Controlling Coherency Phase Boundary for High Performance Batteries

Takahiro Yoshinari

Controlling Coherency Phase Boundary for High Performance Batteries

Takahiro Yoshinari

Graduate School of Human and Environmental Studies

Kyoto University

Supervised by

Prof. Dr. Yoshiharu Uchimoto

Contents

Chapter 1.
General introduction

1.1. Batteries and their fundamental principals

1.1.1. Basics

A battery is composed of two electrodes and an electrolyte and is an electric storage device that stores electric energy as chemical energy. The two electrodes have different chemical potential, and a chemical reaction takes place based on this difference. A combination of electrodes provides many kinds of batteries. An electrode with a higher potential is called a cathode which is a positive electrode, and a lower one is called an anode which is a negative electrode. The electrolyte is an ionic conductor but an electric insulator, otherwise it would cause an internal short-circuit. An electrolyte is used as a separator between the cathode and anode and offers a diffusion path for the charge transfer ions among them.

When the electrodes are connected to each other across the electrolyte, electrons move from the anode to the cathode throughout the external circuit. As electric current flows, electric energy can be taken out. Meanwhile, ions move through electrolyte from/in electrodes with maintaining electrical neutrality. This is the discharge process, where reduction reactions that receive electrons from the external circuit occur in the cathode while oxidation reactions that release electrons to the external circuit occur in the anode. The charge process is the opposite. As this electrochemical reaction is not subject to the restriction of Carnot cycle, the theoretical conversion efficiency calculated from Gibbs free energy is 100%, which is efficient energy conversion and storage system with the lowest entropy production.[1]

This framework can be applied to such as Li-ion batteries or other batteries with an ion-carrier. In the following, taking a closer look at each component in Li-ion battery system as an example. The schematic diagram[2] is shown in **Figure 1.1**. The cathode is layered transition metal oxides and the anode is graphite, which is one of the most typical combination. Each of electrode active materials is mixed with conductive carbon and binder to form a paste. The products are casted onto each current collector, which is

aluminum for the cathode side and copper for the anode side. Both of them are inexpensive, lightweight and high durability even if they are made of thin films. These electrodes are placed across a separator sheet soaked in an electrolyte.

The working principle will be described. During discharge, Li ions are released from the anode into the electrolyte through the electrode/electrolyte interface, and are inserted into the cathode through the electrode/electrolyte interface again. Meanwhile, electrons move from the anode to the cathode through the external circuit. The oxidation reaction of graphite occurs at the anode, and the reduction reaction of the transition metal element M mainly proceeds at the cathode. This electrochemical reaction on discharge is expressed by the following equation:

(cathode) $\mathrm{LiMO_2} \rightarrow \mathrm{Li_{1-x}MO_2} + x\mathrm{Li^+} + x\mathrm{e^{-1}}$

(anode) $\mathrm{C_6} + x\mathrm{Li^+} + x\mathrm{e^-} \rightarrow \mathrm{Li}_x\mathrm{C_6}$

(overall) $\mathrm{LiMO_2} + \mathrm{C_6} \rightarrow \mathrm{Li_{1-x}MO_2} + \mathrm{Li}_x\mathrm{C_6}$

The charge reaction is opposite to the discharge:

(cathode) $\mathrm{Li_{1-x}MO_2} + x\mathrm{Li^+} + x\mathrm{e^{-1}} \rightarrow \mathrm{LiMO_2}$

(anode) $\mathrm{Li}_x\mathrm{C_6} \rightarrow \mathrm{C_6} + x\mathrm{Li^+} + x\mathrm{e^-}$

(overall) $\mathrm{Li_{1-x}MO_2} + \mathrm{Li}_x\mathrm{C_6} \rightarrow \mathrm{LiMO_2} + \mathrm{C_6}$.

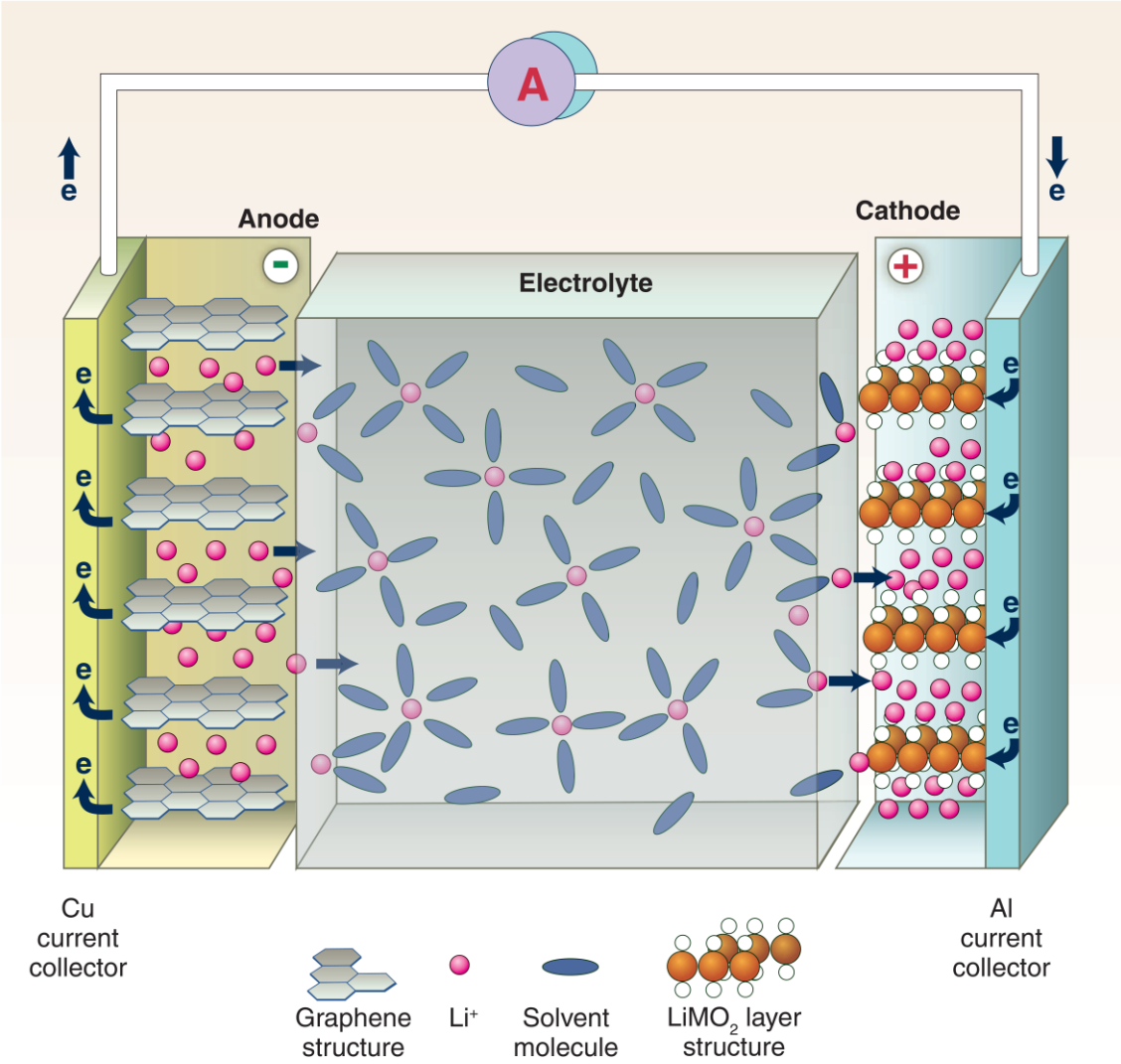

Figure 1.1. *Schematic of a Li-ion battery. The negative electrode is a graphitic carbon that holds Li in its layers, whereas the positive electrode is a Li-intercalation compound—usually an oxide because of its higher potential—that often is characterized by a layered structure. Both electrodes are able to reversibly insert and remove Li ions from their respective structures. On charging, Li ions are removed or deintercalated from the layered oxide compound and intercalated into the graphite layers. The process is reversed on discharge. The electrodes are separated by a nonaqueous electrolyte that transports Li ions between the electrodes.*[2]

The theoretical capacity of the electrode material is calculated as follows:

$$Q = \frac{1}{W} \times n \times F \times \frac{1000}{3600} \tag{1-1}$$

where Q [mAh/g] is the theoretical capacity, W [g/mol] is the molecular weight, n is

the number of electrons in the reaction, and F [C / mol] is the Faraday constant. The last term on the right side multiplies to convert unit C (coulomb) to mAh. In the battery system, unit mAh, not C, is used because time unit of hour is convenient rather than unit sec. For instance, considering the case of a battery capacity of 1822 mAh (which is equivalent to the battery capacity of iPhone 8 made by Apple Inc. Theoretical capacity and actual one must be considered separately, however). A current of 150 mA can flow for about 12 h (= 1882 mAh / 150 mA) to fully charge this battery from empty, while for the quick charge within 30 min, 3764 mA (= 1882 mAh / 0.5 h) is needed. In this manner, unit mAh after conversion is more convenient than C (coulomb).

Unit C for rate is a technical word for the battery community. 1 C is a current value that the theoretical capacity is charged and discharged for 1 h. That is, 10 C is a current value to charge and discharge the theoretical capacity for 6 min and 0.2 C is for 5 h. In the example above, 0.5 C corresponds to 941 mA.

1.1.2. Thermodynamics

The battery systems follow directly from the thermodynamic and kinetic formulations for chemical reactions as adapted to electrochemical reactions.[1] The basic thermodynamic equations for a reversible electrochemical response at constant temperature are given as

$$\Delta G = \Delta H - T\Delta S \tag{1-2}$$

and

$$\Delta G^\circ = \Delta H^\circ - T\Delta S^\circ \tag{1-3}$$

where ΔG is the Gibbs free energy, or the energy of a reaction available for useful work, ΔH is the enthalpy, or the energy released by the reaction, ΔS is the entropy, and T is the absolute temperature, with $T\Delta S$ being the heat associated with the organization/disorganization of materials. The terms ΔG, ΔH, and ΔS are state functions and depend only on the identity of the materials and the initial and final states of the reaction. The degree symbol is used to indicate that the value of the function is for the material in the standard state at 25°C and unit activity.

Because ΔG represents the net useful energy available from a given reaction, in electrical terms, the net available electrical energy from a reaction in a cell is given by

$$\Delta G = -nFE \tag{1-4}$$

and

$$\Delta G^\circ = -nFE^\circ \tag{1-5}$$

where n is the number of electrons transferred per mole of reactants, F is the Faraday constant, being equal to the charge of one electron, and E is the voltage of the cell with the specific chemical reaction; in other words, E is the electromotive force (emf) of the cell reaction. The voltage of the cell is unique for each reaction couple. The amount of electricity produced, nF, is determined by the total amount of materials available for reaction and can be thought of as a capacity factor; the cell voltage can be considered to be an intensity factor. The usual thermodynamic calculations on the effect of temperature, pressure, etc., apply directly to electrochemical reactions. Spontaneous processes have a negative free energy and a positive emf with the reaction written in a reversible fashion, which goes in the forward direction. The van't Hoff isotherm identifies the free energy relationship for bulk chemical reactions as

$$\Delta G = \Delta G^\circ + RT \ln\left(a_p/a_r\right) \tag{1-6}$$

where R is the gas constant, a_p the activity product of the products and a_r the activity product of the reactants. Combining eqs (1-4) to (1-6), the Nernst equation for electrochemical reactions is

$$E = E^\circ + RT \ln\left(a_p/a_r\right). \tag{1-7}$$

Faraday's laws, as summarized in eq (1-7), give the direct relationship between the amount of reaction and the current flow. There are no known exceptions to Faraday's laws.

$$g = \frac{ItW}{nF}. \tag{1-8}$$

g is the grams of material transformed, I is the current flow (amps), t is the time of current flow (seconds, hours), W is the molecular or atomic weight of the material being transformed, and n is the number of electrons in the reaction.

1.1.3. Kinetics

Thermodynamics describe reactions at equilibrium and the maximum energy release for a given reaction. Compared to the equilibrium voltage (= open circuit voltage, E_{OCV}), the

voltage drops off (= "electrode polarization" or "overvoltage") when current is drawn from the battery because of kinetic limitations of reactions and of other processes must occur to produce current flow during operation. Electrochemical reaction kinetics follow the same general considerations as those for bulk chemical reactions. However, electrode kinetics differs from chemical kinetics in two important aspects: (1) the influence of the potential drop in the electrical double layer at an electrode interface as it directly affects the activated complex and (2) the fact that reactions at electrode interfaces proceed in a two-dimensional, not three-dimensional, manner. The detailed mechanism of battery electrode reactions often involves a series of physical, chemical, and electrochemical steps, including charge-transfer and charge transport reactions. The rates of these individual steps determine the kinetics of the electrode and, thus, of the cell/battery. Basically, three different kinetics effects for polarization have to be considered: (1) activation polarization is related to the kinetics of the electrochemical redox (or charge-transfer) reactions taking place at the electrode/electrolyte interfaces of anode and cathode; (2) ohmic polarization is interconnected to the resistance of individual cell components and to the resistance due to contact problems between the cell components; (3) concentration polarization is due to mass transport limitations during cell operation. The polarization, η, is given by

$$\eta = E_{OCV} - E_T. \tag{1-9}$$

where E_{OCV} is the voltage of the cell at open circuit and E_T is the terminal cell voltage with current, I, flowing.

Activation polarization arises from kinetics hindrances of the charge-transfer reaction taking place at the electrode/electrolyte interface. This type of kinetics is best understood using the absolute reaction rate theory or the transition state theory. In these treatments, the path followed by the reaction proceeds by a route involving an activated complex, where the rate-limiting step is the dissociation of the activated complex. The rate, current flow, i ($i = I/A$ and $i_0 = I_0/A$, where A is the electrode surface area), of a charge-transfer-controlled battery reaction can be given by the Butler–Volmer equation as

$$i = i_0\left[\exp(\alpha F\eta/RT) - \exp\big((1-\alpha)F\eta/RT\big)\right]. \tag{1-10}$$

where the exchange current density, $i_0 = k_0 FA$ is the exchange current density (k_0 is the reaction rate constant for the electrode reaction, and A is the activity product of the reactants), η is the polarization or departure (overpotential) from equilibrium ($\eta = E_{OCV} - E_T$), and α is the transfer coefficient, which is best considered as the fraction of

the change of overpotential that leads to a change in the rate constant for charge-transfer reaction. The exchange current density is directly related to the reaction rate constant, to the activities of reactants and products, and to the potential drop across the double layer. Reactions with larger i_0 are more reversible and have lower polarization for a given current flow. Electrode reactions having high exchange currents (i_0 in the range of 10^{-2} A/cm^2) at room temperature are favored for use in battery applications. The buildup and decay of the activation polarization are fast and can be identified by the voltage change on current interruption in a time frame of 10^{-2}–10^{-4} s.

The activation polarization follows the Tafel equation derived from eq (1-8)

$$\eta = a - b\log(I/I_0) \tag{1-11}$$

where a and b are constants.

Ohmic polarization arises from the resistance of the electrolyte, the conductive diluent, and materials of construction of the electrodes, current collectors, terminals, and contact between particles of the active mass and conductive diluent or from a resistive film on the surface of the electrode. Ohmic polarization appears and disappears instantaneously ($\leq 10^{-6}$ s) when current flows and ceases. Under the effect of ohmic resistance, R, there is a linear Ohm's Law relationship between I and η.

$$\eta = IR \tag{1-12}$$

As the redox reactions proceed, the availability of the active species at the electrode/electrolyte interface changes. Concentration polarization arises from limited mass transport capabilities, for example, limited diffusion of active species to and from the electrode surface to replace the reacted material to sustain the reaction. Diffusion limitations are relatively slow, and the buildup and decay take $\geq 10^{-2}$ s to appear. For limited diffusion the electrolyte solution, the concentration polarization, can be expressed as

$$\eta = (RT/n)\ln(C/C_0) \tag{1-13}$$

where C is the concentration at the electrode surface and C_0 is the concentration in the bulk of the solution. The movement or transport of reactants from the bulk solution to the reaction site at the electrode interface and vice versa is a common feature of all electrode reactions. Most battery electrodes are porous structures in which an interconnected matrix of small solid particles, consisting of both nonconductive and

electronically conductive materials, is filled with electrolyte. Porous electrode structures are used to extend the available surface area and lower the current density for more efficient operation.

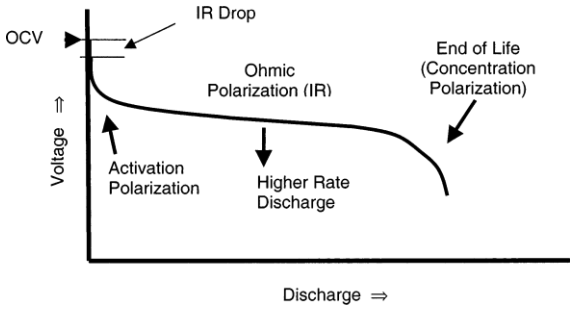

Figure 1.2. *Typical discharge curve of a battery, showing the influence of the various types of polarization.*[1]

1.2. Thermodynamics of binary systems

1.2.1. Regular solution approximation

When temperature and pressure are fixed in a system, Gibbs free energy has a certain value in pure substances, whereas it attributes composition dependent curves in binary mixtures. The latter state is called solution in liquid or gas systems as well as solid solution in a solid system. In the following, Gibbs free energy of $A-B$ binary system will be described with an assumption of arithmetic average of segregation limit for the first step, ideal solution approximation with mixed entropy, and regular solution approximation with mixed enthalpy in addition.

In a binary solution of $A-B$, Gibbs free energy of simple substances A and B are ${G_A}^0$ and ${G_B}^0$, respectively. Atomic fraction of A and B are x_A and x_B when mixed both samples. For the state where the two phases are completely separated, that is, at the segregation limit, the Gibbs free energy of mixing is

$$G^0 = x_A {G_A}^0 + \mathrm{x_B} {G_B}^0. \tag{1-14}$$

It is assumed that A and B atoms are completely disordered. The total number for arranging A atoms of N_A particles and B atoms of N_B particles at lattice points in the solution is

$$W = \frac{(N_A + N_B)!}{N_A! \cdot N_B!}. \tag{1-15}$$

In general, the entropy of an aggregate of atoms is expressed by the Boltzmann's equation with the number of cases of atomic arrangement W.

$$S = k_B \ln W \tag{1-16}$$

where k_B is the Boltzmann constant. The number N is set to the number of lattices for 1 mol, that is, Avogadro's constant, satisfying the equation of $N = N_A + N_B$. With Stirling's approximation of $\ln N! \sim N \ln N - N$, the enthalpya of mixing is

$$\begin{aligned} \Delta S_{mix} &= k_B \ln W = k_B \ln \frac{(N_A + N_B)!}{N_A! \cdot N_B!} \\ &= -(N_A + N_B) k_B \left(\frac{N_A}{N_A + N_B} \ln \frac{N_A}{N_A + N_B} \right. \\ &\qquad \left. + \frac{N_B}{N_A + N_B} \ln \frac{N_B}{N_A + N_B} \right) \\ &= -R(x_A \ln x_A + x_B \ln x_B). \end{aligned} \tag{1-17}$$

A solution in which there is no interaction between each atom and the atomic arrangement is disordered is called an ideal solution. The Gibbs free energy of this ideal solution is expressed by adding the entropy of mixing to the segregation limit model as mentioned above:

$$\begin{aligned} G^{ideal} &= x_A {G_A}^0 + \mathrm{x_B} {G_B}^0 + RT(x_A \ln x_A + x_B \ln x_B) \\ &= G^0 - T\Delta S_{mix}. \end{aligned} \tag{1-18}$$

Since the entropy of mixing ΔS_{mix} is always positive, $G^{ideal} < G^0$ holds, so that it is more stable for the system to become a solution state by mixing atoms with each other rather than at the segregation limit.

Interaction between heterogeneous atoms cannot be ignored in an actual solution, and then enthalpy of mixing must be considered. In the aggregated phase of liquid or solid, the pressure term (pV) is smaller than the energy term (E), so that the approximation of $H = pV + E \sim E$ can be used. The interaction energy is calculated under the following assumption:

① The cohesive energy of the solution is represented by the sum of the bonding energy only between the nearest neighbor atoms. The bonding energy between atoms separated by the second adjacent position or more is ignored.

② The bonding energy between the nearest neighbor atoms depends only on the kind of the atom pair and not on the surrounding atoms.

With the number of $i-j$ bonds (N_{ij}) and their binding energy (E_{ij}), the energy after mixing is

$$H = N_{AA}E_{AA} + N_{BB}E_{BB} + N_{AB}E_{AB} \tag{1-19}$$

as described in **Figure 1.3**.

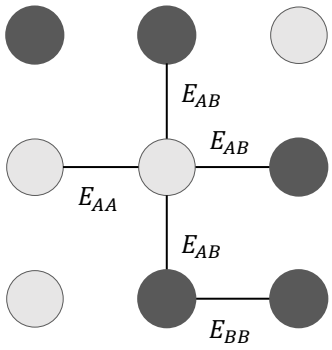

Figure 1.3. *Bonding energy between* ***A*** *and* ***B*** *atoms under regular solution approximation in a binary system.* ***A*** *atoms represent the light gray and* ***B*** *atoms the dark gray.*

The total number of A atoms is N_A, the total number of B atoms is N_B, and z is the coordination number. To avoid the duplication of A and B atoms, N_{ij} are expressed as following:

$$\begin{aligned} N_{AA} &= \frac{1}{2}N_A z x_A = \frac{1}{2}N z {x_A}^2 \\ N_{BB} &= \frac{1}{2}N_B z x_B = \frac{1}{2}N z {x_B}^2 \\ N_{AB} &= N_A z x_B = N_B z x_A = N z x_A x_B \end{aligned} \tag{1-20}$$

Then,

$$
\begin{aligned}
H &= \frac{1}{2}Nz{x_A}^2E_{AA} + \frac{1}{2}Nz{x_B}^2E_{BB} + Nzx_Ax_BE_{AB} \\
&= \frac{1}{2}Nzx_A(1-x_B)E_{AA} + \frac{1}{2}Nzx_B(1-x_A)E_{BB} + Nzx_Ax_BE_{AB} \\
&= \frac{1}{2}Nzx_AE_{AA} + \frac{1}{2}Nzx_BE_{BB} + Nzx_Ax_B\left(E_{AB} - \frac{E_{AA}+E_{BB}}{2}\right).
\end{aligned}
\tag{1-21}
$$

The first two terms equal to the energy at segregation limit.

The Gibbs free energy of before mixing is

$$
\begin{aligned}
G^0 &= H^0 \\
&= \frac{1}{2}Nzx_AE_{AA} + \frac{1}{2}Nzx_BE_{BB} \\
&= x_A{H_A}^0 + x_B{H_B}^0
\end{aligned}
\tag{1-22}
$$

${H_A}^0 = NzE_{AA}/2$ and ${H_B}^0 = NzE_{BB}/2$ are the enthalpy of pure substances. Therefore, the enthalpy of mixing under regular solution approximation is finally

$$
\begin{aligned}
\Delta H_{mix} &= H - H^0 \\
&= Nzx_Ax_B\left(E_{AB} - \frac{E_{AA}+E_{BB}}{2}\right) \\
&= \Omega x_Ax_B
\end{aligned}
\tag{1-23}
$$

where Ω represents the deviation from the ideal solution and is called the interaction parameter. This is an inherent parameter of the system, characterizing thermodynamic properties peculiar to the solution. The solution model considering only the binding energy of a nearest atom pair is referred to as regular solution approximation. The Gibbs free energy of mixing is

$$
\begin{aligned}
G_{mix} &= G^0 + \Delta H_{mix} - T\Delta S_{mix} \\
&= G^{ideal} + \Delta H_{mix} \\
&= x_A{G_A}^0 + x_B{G_B}^0 + \Omega x_Ax_B + RT(x_A\ln x_A + x_B\ln x_B).
\end{aligned}
\tag{1-24}
$$

1.2.2. Thermodynamic interaction parameters

Since interaction between heterogeneous atoms cannot be ignored in a regular solution, its Gibbs free energy is expressed by the formula **(1-24)** as shown above. In this equation, the thermodynamic properties of the solution change according to the value of Ω:

$$
\Omega = Nz\left(E_{AB} - \frac{E_{AA}+E_{BB}}{2}\right).
\tag{1-25}
$$

Since $E_{AB} < (E_{AA}+E_{BB})/2$ when $\Omega < 0$, the energy of the $A-B$ pair is lower than the

average energy of the $A-A$ pair and the $B-B$ pair, which means A atoms and B atoms try to attract each other. Consequently, the solution show ordering trend (**Figure 1.4b**). On the other hand, since $E_{AB} > (E_{AA}+E_{BB})/2$ when $\Omega > 0$, the energy of the $A-B$ pair is higher than the average energy of the $A-A$ pair and the $B-B$ pair, which means A atoms and B atoms try to repel each other. Therefore, A atoms bond to A atoms themselves and B atoms as well, so that the solution tends to separate into two phases (**Figure 1.4c**). When $\Omega = 0$, there is no interaction between A atoms and B atoms, so that the atomic arrangement becomes disordered. That is an ideal solution.

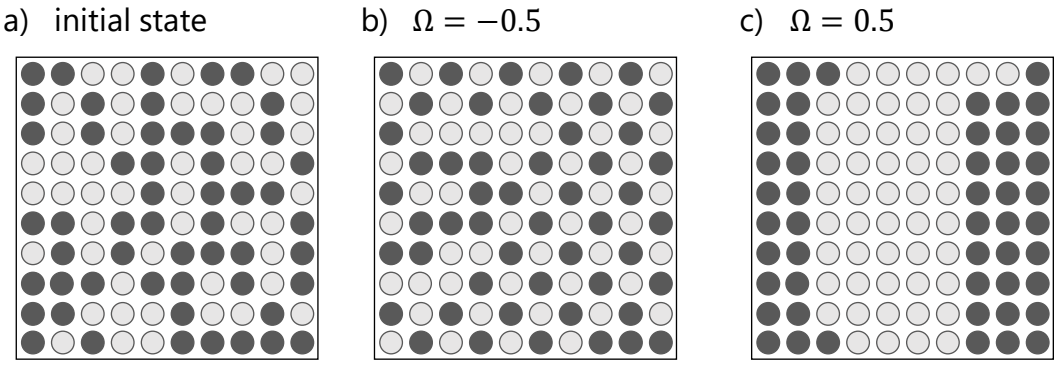

Figure 1.4. *Simulation of two interaction parameters in a binary system under regular solution approximation.* ***A*** *atoms represent the light gray and* ***B*** *atoms the dark gray.*

1.2.3. Composition – Gibbs free energy diagram

Gibbs free energy of mixing of a regular solution subtracted from that of ideal solution is called excessive Gibbs free energy. From the equation **(1-24)**,

$$\Delta G_{mix}^{EX} = G_{mix} - G^{ideal} = \Omega x_A x_B. \tag{1-26}$$

As can be seen from this equation, excess Gibbs free energy is always symmetric with respect to concentration. In an actual case, when the interaction parameter Ω is dependent on concentration, it is expressed such as $\Omega = \Omega_0 + \Omega_1 x_B$. This is called semi-regular solution approximation.

Gibbs free energy of mixing per 1 mol in a regular solution can be expressed as follows using chemical potential μ_A for A atom.

$$G_{mix} = x_A\mu_A + x_B\mu_B \tag{1-27}$$

In the case of an ideal solution, the chemical potential is

$$\mu_A^{ideal} = G_A{}^0 + RT\ln x_A. \tag{1-28}$$

Considering the deviation from the ideal solution, the chemical potential of the regular solution is

$$\begin{aligned}\mu_A &= G_A{}^0 + RT\ln a_A \\ &= G_A{}^0 + RT\ln \gamma_A x_A\end{aligned} \tag{1-29}$$

where a_A represents activity of A atom and γ_A is activity coefficient, which is 1 for an ideal solution. Therefore, excessive Gibbs free energy with the activity coefficients is

$$\Delta G_{mix}^{EX} = RT(x_A\ln\gamma_A + x_B\ln\gamma_B) \tag{1-30}$$

In this way, the interaction parameter is embed in the activity coefficients, enabling to calculate the interaction parameter from the activity coefficients.

The composition-Gibbs free energy diagram is illustrated by the equation **(1-24)** as shown in **Figure 1.5**. Since the energy of the segregation limit is expressed as $G^0 = x_A G_A{}^0 + \mathrm{x_B} G_B{}^0$, it becomes a straight line connecting $G_A{}^0$ and $G_B{}^0$ as indicated by the dotted line in **Figure 1.5**. As $\Delta S_{mix} > 0$ is always satisfied, the entropy of mixing $-T\Delta S_{mix}$ is symmetric with respect to concentration and shows a negative value. As the enthalpy of mixing is $\Delta H_{mix} = \Omega x_A x_B$ as well as $x_A x_B = (1 - x_B)x_B > 0$, this is also symmetric with respect to concentration.

When $\Omega < 0$, the Gibbs free energy of mixing describes a convex downward curve at any temperature as shown in **Figure 1.5a**. On the other hand, when $\Omega > 0$, ΔH_{mix} is convex upward whereas $-T\Delta S_{mix}$ is convex downward energy curve, so that the inflection point is generated in the Gibbs free energy curve in a certain temperature range due to the relative relation between the enthalpy and the entropy such as **Figure 1.5b.** In this case, it is advantageous in terms of energy to separate into two phases having different concentrations. A coexisting region of two phases with the same structure is generated.

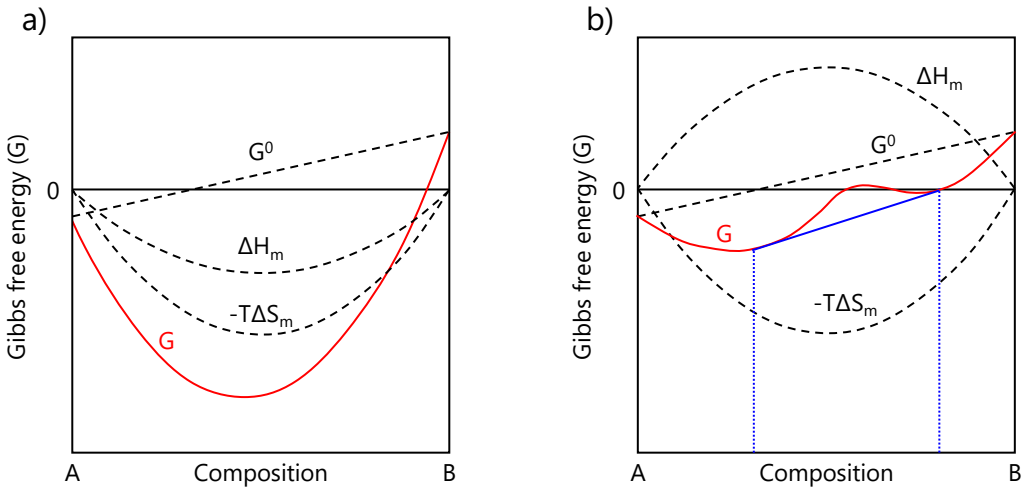

Figure 1.5. Composition – Gibbs free energy diagram.

Taking a closer look at the case of $\Omega > 0$, which tends to separate into two phases. When the $A-B$ binary solution consists of two phases, α and β phase, at a certain temperature, the composition-Gibbs free energy diagram shows a partially convex upward curve with an inflection point as shown in **Figure 1.6**.

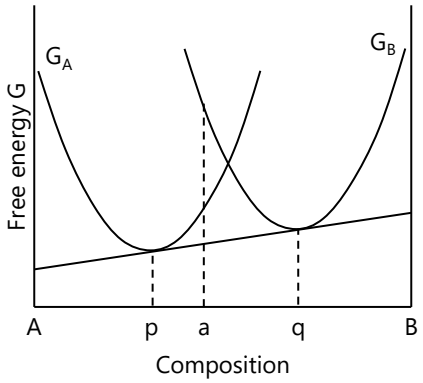

Figure 1.6. Composition – Gibbs free energy diagram.

Upon a common tangent to the Gibbs free energy curve of each phase, the concentration at the contact point with the Gibbs free energy curve G^{α} (of the α phase) and G^{β} (of the β phase) is p and q, respectively. Considering the case where the concentration of

the system is a satisfying $p < a < q$, Gibbs free energy of mixing at concentration a using a chemical potential such as equation **(1-27)** is

$$G^{\alpha+\beta}(a) = (1-a)\mu_A + a\mu_B. \tag{1-31}$$

The Gibbs free energy G^{α} at concentration p and the Gibbs free energy G^{β} at concentration q are

$$\begin{aligned} G^{\alpha}(p) &= (1-p)\mu_A^{\alpha} + p\mu_B^{\alpha} \\ G^{\beta}(q) &= (1-q)\mu_A^{\beta} + q\mu_B^{\beta}. \end{aligned} \tag{1-32}$$

When two phases are in equilibrium, the chemical potential of each component is equal.

$$\mu_A = \mu_A^{\alpha} = \mu_A^{\beta}, \qquad \mu_B = \mu_B^{\alpha} = \mu_B^{\beta} \tag{1-33}$$

At this time, the equation (1-32) can be rearranged as follows.

$$\begin{aligned} \mu_A &= \frac{q}{q-p}G^{\alpha}(p) + \frac{-p}{q-p}G^{\beta}(q) \\ \mu_B &= \frac{q-1}{q-p}G^{\alpha}(p) + \frac{1-p}{q-p}G^{\beta}(q) \end{aligned} \tag{1-34}$$

This chemical potential is substituted into the equation (1-31) and arranged:

$$G^{\alpha+\beta}(a) = \frac{q-a}{q-p}G^{\alpha}(p) + \frac{a-p}{q-p}G^{\beta}(q). \tag{1-35}$$

This is the point on the common tangent line in **Figure 1.6**. Since $G^{\alpha+\beta}(a) < G^{\alpha}(a)$ and $\backsim G^{\alpha+\beta}(a) < G^{\beta}(a)$ always hold, it is more stable that the two phases are separated and coexistent in the equilibrium state rather than the solid solution of only α phase or β phase is formed. Conversely, when a common tangent line can be drawn to the Gibbs free energy curve of the two phases, there is a region where two phases are separated.

According to the equation **(1-27)**, the chemical potentials μ_A and μ_B correspond to intercepts of the common tangent at $x_A = 1$ and $x_B = 1$, respectively (**Figure 1.7**). This can easily be confirmed geometrically.

$$\mu_A = G_{mix} + x_A \left(\frac{\partial G_{mix}}{\partial x_A}\right)$$
$$\mu_B = G_{mix} + x_B \left(\frac{\partial G_{mix}}{\partial x_B}\right) \quad (1\text{-}36)$$

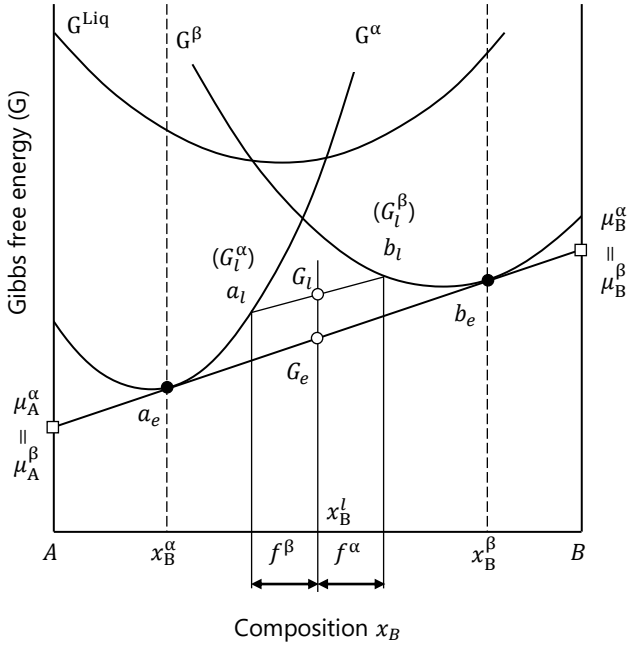

Figure 1.7. Composition – Gibbs free energy diagram.

In the following, based on the eutectic binary phase diagram as shown in **Figure 1.8**, the Gibbs free energy curve at each temperature is considered.

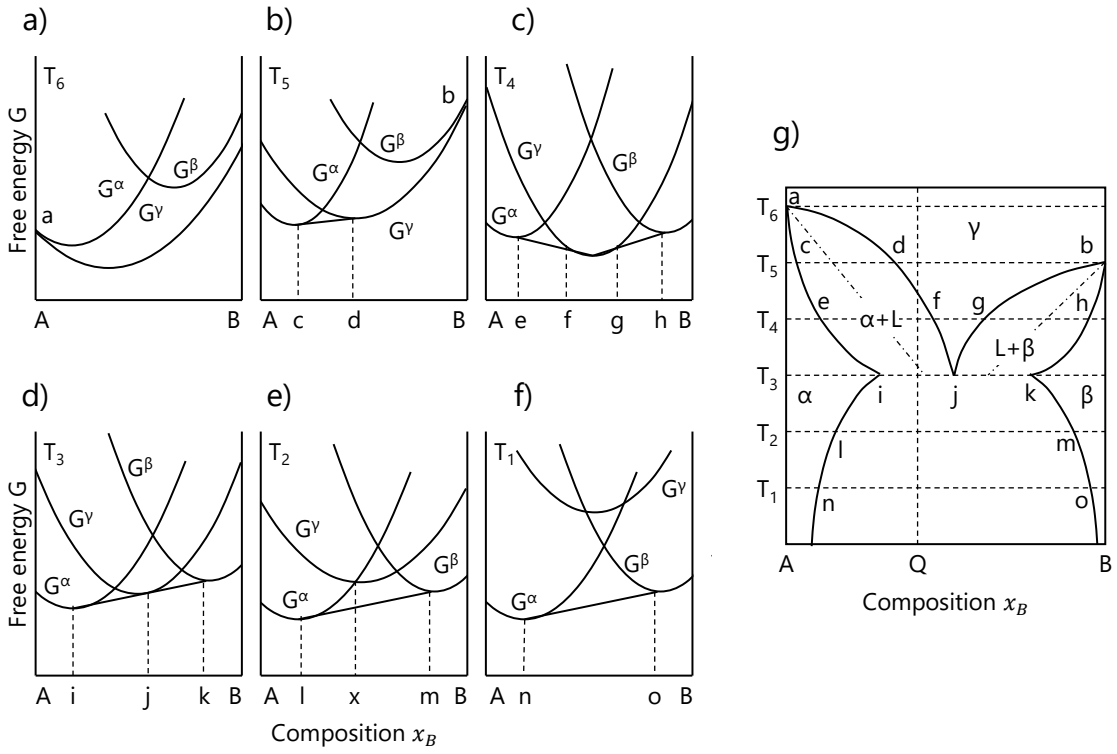

Figure 1.8. Phase diagram of eutectic binary system.

At temperature T_5, the Gibbs free energy curves of α phase and γ phase intersect at an certain concentration, so that the common tangent line can be drawn to these phases. There are regions in which two phases of α phase and γ phase coexist. In the concentration between Ac, the system becomes α phase solid solution, and between cd the system becomes coexistence of two phases of α phase and γ phase. The Gibbs free energy of γ phase is the lowest between dB so γ phase is stable. At temperature T_4, the Gibbs free energy curves of α and β phases intersect with that of γ phase. One α phase solid solution phase between Ae, which is the concentration range, two phase coexistence of α phase and γ phase between ef, one γ phase between fg, two phase coexistence of β phase and γ phase between gh, and one β phase between hB are stable in equilibrium state. At temperature T_3, a common tangent line to the three Gibbs free energy curves is drawn. Since γ phase is in equilibrium state with both α phase and β phase, this temperature is called the eutectic temperature in the binary system. When the temperature further drops to T_2, one α phase or one β phase exist between Al or mB, respectively. There are two phases coexistence with α and β phase without γ phase between lm, the total Gibbs free energy becomes very small.

1.2.4. Spinodal decomposition

Considering a case where a supersaturated solid solution is separated into two phases having different composition but same crystal structure, the Gibbs free energy of both phases offers a continuous curve. The shape of the Gibbs free energy curve depends on the interaction parameter Ω, which represents the solid solution stability against concentration fluctuation.

Considering $A-B$ binary system, when the minute concentration fluctuation occurs and the mixture is separated into two phases (**Figure 1.9**). When the Gibbs free energy curve is convex downward, the Gibbs free energy of the system increases, so that the concentration fluctuation disappears and the solid solution is kept stable. On the other hand, if the Gibbs free energy curve is convex upwards, the Gibbs free energy of the system decreases and the solid solution becomes unstable. Then, the condition that the solid solution is stable against fluctuation is

$$\frac{\partial^2 G}{\partial {x_B}^2} > 0. \tag{1-37}$$

At a certain temperature satisfying $\Omega > 0$, the Gibbs free energy curve has two local minima and the stability of the solid solution against fluctuation depends on three concentration regions.

① Less than x_1 and more than x_2: Stable with uniform solid solution.

In the inside of the binodal line $\partial G/\partial x_B = 0$, the solid solution is separated into two phases.

② More than x_1 and less than s_1, or more than s_2 and less than x_2: Phase separation occurs only when the fluctuation range of concentration is large.

③ More than s_1 and less than s_2: Inside the spinodal line $\partial^2 G/\partial {x_B}^2 = 0$, even if slight concentration fluctuation occurs, its width increases and phase separation occurs.

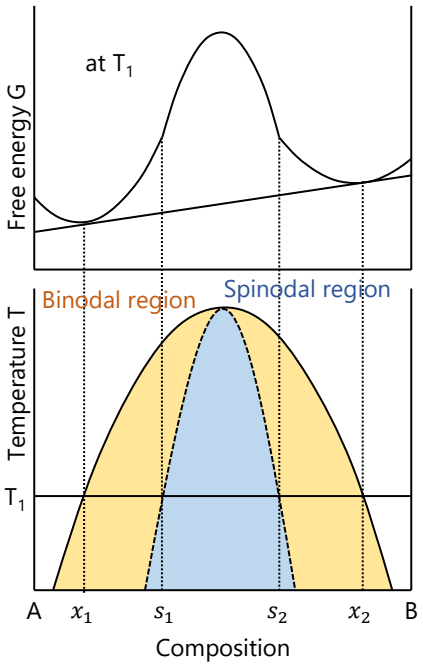

Figure 1.9. Spinodal and bimodal decomposition curve.

1.2.5. Driving force for phase change

In $A-B$ binary system, the driving force for precipitating the β phase from supersaturated solid solution of α phase is shown in **Figure 1.10**. The crystal structure of α and β phase are different, and both phases have individual Gibbs free energy curves. The Gibbs free energy at equilibrium is given by the common tangent of both Gibbs free energy curves.

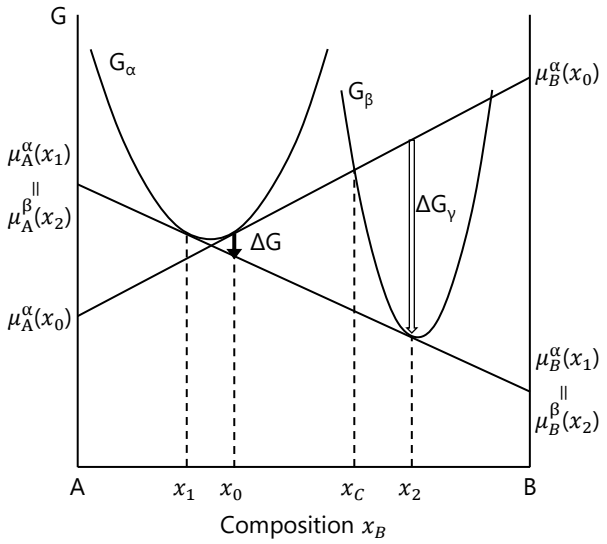

Figure 1.10. Composition – Gibbs free energy diagram.

When the concentration of the solid solution in the parent phase is x_0, the driving force of the precipitation reaction is represented by ΔG in **Figure 1.10**.

$$\Delta G = (1 - x_0)\mu_A{}^\alpha(x_1) + x_0\mu_B{}^\alpha(x_1) - G^\alpha(x_0) \tag{1-38}$$

At the nucleation in the early stage of the reaction, when a very small amount of β phase produces out of a large volume of α phase, the concentration change of the parent phase due to the precipitation of β phase is almost negligible. The Gibbs free energy of this reaction, which is the driving force for the nucleation of β phase is expressed as follows:

$$\begin{aligned}\Delta G_V = &\left[(1 - x_2)\mu_A{}^\beta(x_2) + x_2\mu_B{}^\beta(x_2)\right] \\ &- [(1 - x_2)\mu_A{}^\alpha(x_0) + x_2\mu_B{}^\alpha(x_0)].\end{aligned} \tag{1-39}$$

The first term on the right side is the Gibbs free energy of β phase at the concentration x_2, and the second term is the Gibbs free energy where the concentration of A and B atoms in the parent phase having the initial concentration x_0 is x_2.

The driving force ΔG_V is generated if the nucleus concentration is greater than x_C in **Figure 1.10**. The maximum driving force $\Delta G_V{}^{max}$ can be produced when the tangent of the Gibbs free energy curve of β phase is drawn to be parallel to the tangent of the Gibbs free energy curve of α phase at the initial concentration and the nuclei is formed with

the concentration of the contact point.

1.2.6. Activation energy of nucleation

Nucleation by diffusion of atoms is a phenomenon in which a new phase of the minimum size that is stable against the fluctuation of the concentration and/or the structure in the parent phase is generated. In the elementary processes, the size of clusters changes due to attachment / detachment of atoms.

The Gibbs free energy change ΔG_r due to cluster formation of a new phase with atoms of radius r is shown in **Figure 1.11**.

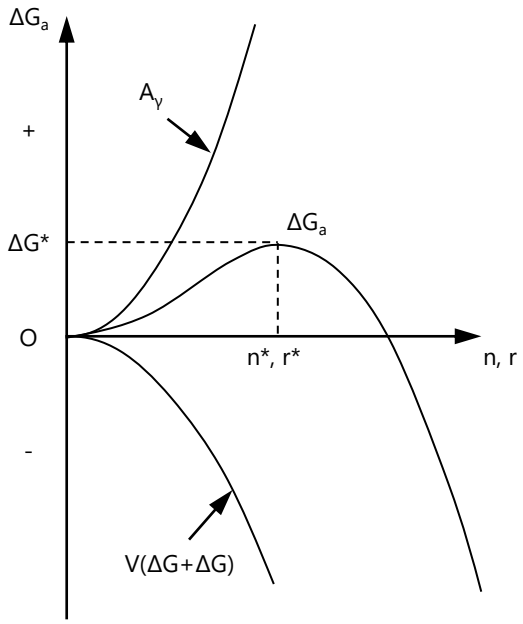

Figure 1.11. Activation energy of nucleus reaction.

When the interfacial energy γ is constant, ΔG_r can be expressed as follows using the volume V of the new phase, the interface area A, and the elastic strain energy ΔG_s:

$$\Delta G_r = V(\Delta G_V + \Delta G_s) + A\gamma \tag{1-40}$$

The driving force for nucleation ΔG_V is a Gibbs free energy change from the parent phase to the new phase per unit volume and takes a negative value. On the other hand, the interfacial energy γ and elastic strain energy ΔG_s are positive. In order to occur the phase change, the Gibbs free energy of the system must decrease. It is necessary that the

driving force generated by a certain volume of the new phase exceeds the interfacial energy and elastic strain energy, which means there is an energy barrier for nucleation.

Ignoring the elastic strain energy, the shape of the new phase at nucleation is given as the condition of minimum interface energy per unit area. When the interface energy is isotropic, the shape of the new phase becomes spherical without anisotropy. At this time, the Gibbs free energy change is

$$\Delta G_r = \frac{4\pi r^3}{3}(\Delta G_V + \Delta G_s) + 4\pi r^2 \gamma \tag{1-41}$$

The local maximum value ΔG_{r^*} is taken for a certain nucleus size r^*. As clusters exceeding the critical radius become larger, ΔG_r turns to decrease and they grows furthermore. On the other hand, as clusters below the critical radius try to be larger, ΔG_r will increase and they tend to disappear. The radius r^* of the spherical critical nucleus and the activation energy ΔG_{r^*} for the critical nucleation are

$$\begin{aligned} r^* &= \frac{-2\gamma}{(\Delta G_V + \Delta G_s)} \\ \Delta G_{r^*} &= \frac{16\pi\gamma^3}{3(\Delta G_V + \Delta G_s)^2}. \end{aligned} \tag{1-42}$$

1.3. Two-phase materials in Li-ion batteries

$LiFePO_4$ is a phase separated and anisotropic material[3-6] with a large miscibility gap for particles larger than ~50 nm[7] and exhibits one-dimensional lithium migration[8, 9]. At low current rates, $LiFePO_4$ intercalates via a particle-by-particle pathway, first explained by the domino cascade model[10] and more recently by its non-monotonic Li chemical potential profile[11, 12]. At elevated current rates, density functional theory[13] and reaction-limited phase-field modelling[14] suggest that phase separation is suppressed and replaced with a solid solution pathway. This metastable solid solution was observed using operando diffraction and microscopy[15-19], and the solid solution phase separates into Li-rich and Li-poor phases under equilibrium at room temperature[13].

1.4. Metal/metal fluoride battery system

Recently, Reddy and Fichtner for the first time demonstrated rechargeable fluoride ion batteries working at a temperature of 150 °C using solid electrolyte.[20] Subsequently, several attempts were made to improve the performance of FIBs: by using nanocrystalline fluorite-type electrolytes,[21] Mg+MgF_2-based composite as an anode,[22] intercalation-based materials as cathodes,[23-25] and by employing thin electrolyte and electrode layers.[26-28] However, in all cases, the cells were operated at 150 °C or above and the reaction mechanism of metal/metal fluoride system has not been understood.

1.5. Objectives

Batteries are widely spread from power supplies for small electronic devices to large energy storage, and are indispensable for realizing a sustainable society. In addition to improving the performance of existing lithium ion batteries, research and development of fluoride-ion batteries, which are high energy density next generation batteries, are undertaken. In both cases, lattice reorganization occurs in the electrode active material due to continuous ion/ lectron transfer in the electrochemical reaction field, and the phase transition progresses. The phase transition reaction proceeds from the interface between the parent phase and the new phase as a starting point, and it is expected that the cycle characteristics and output characteristics of the batteries can be largely improved by understanding the phenomenon and proper control. Many attempts have been taken to improve performance by individual methods for each material so far, but lacking concepts and approaches to integrate them are present conditions. In this study, we firstly clarified the phase boundary movement phenomenon by reducing lattice volume difference in $LiFePO_4$, which is a typical lithium ion battery positive electrode material, and examined its influence. We applied this knowledge to Cu, which is a positive electrode material for fluoride-ion batteries, and attempted to improve the performance of the storage battery.

References

1. Winter, M.; Brodd, R. J., What are Batteries, Fuel Cells, and Supercapacitors? *Chem. Rev.* **2004,** *104* (10), 4245-4269.

2. Dunn, B.; Kamath, H.; Tarascon, J. M., Electrical Energy Storage for the Grid: A Battery of Choices. *Science* **2011,** *334* (6058), 928-935.

3. Padhi, A. K.; Nanjundaswamy, K. S.; Goodenough, J. B., Phospho-Olivines as Positive-Electrode Materials for Rechargeable Lithium Batteries. *J. Electrochem. Soc.* **1997,** *144* (4), 1188-1194.

4. Delacourt, C.; Poizot, P.; Tarascon, J. M.; Masquelier, C., The Existence of a Temperature-Driven Solid Solution in Li_xFePO_4 for 0 <= *x* <= 1. *Nat. Mater.* **2005,** *4* (3), 254-260.

5. Yamada, A.; Koizumi, H.; Nishimura, S. I.; Sonoyama, N.; Kanno, R.; Yonemura, M.; Nakamura, T.; Kobayashi, Y., Room-Temperature Miscibility Gap in Li_xFePO_4. *Nat. Mater.* **2006,** *5* (5), 357-360.

6. Tang, M.; Carter, W. C.; Chiang, Y. M., Electrochemically Driven Phase Transitions in Insertion Electrodes or Lithium-Ion Batteries: Examples in Lithium Metal Phosphate Olivines. *Annual Review of Materials Research, Vol 40* **2010,** *40*, 501-529.

7. Gibot, P.; Casas-Cabanas, M.; Laffont, L.; Levasseur, S.; Carlach, P.; Hamelet, S.; Tarascon, J. M.; Masquelier, C., Room-temperature single-phase Li insertion/extraction in nanoscale Li(x)FePO(4). *Nat. Mater.* **2008,** *7* (9), 741-747.

8. Morgan, D.; Van der Ven, A.; Ceder, G., Li Conductivity in Li_xMPO_4 (M = Mn, Fe, Co, Ni) Olivine Materials. *Electrochem. Solid-State Lett.* **2004,** *7* (2), A30-A32.

9. Islam, M. S.; Driscoll, D. J.; Fisher, C. A. J.; Slater, P. R., Atomic-scale investigation of defects, dopants, and lithium transport in the LiFePO4 olivine-type battery material. *Chem. Mater.* **2005,** *17* (20), 5085-5092.

10. Delmas, C.; Maccario, M.; Croguennec, L.; Le Cras, F.; Weill, F., Lithium Deintercalation in $LiFePO_4$ Nanoparticles via a Domino-Cascade Model. *Nat. Mater.* **2008,** *7* (8), 665-671.

11. Dreyer, W.; Jamnik, J.; Guhlke, C.; Huth, R.; Moskon, J.; Gaberscek, M., The Thermodynamic Origin of Hysteresis in Insertion Batteries. *Nat. Mater.* **2010,** *9* (5), 448-453.

12. Cogswell, D. A.; Bazant, M. Z., Coherency Strain and the Kinetics of Phase Separation in $LiFePO_4$ Nanoparticles. *ACS Nano* **2012,** *6* (3), 2215-2225.

13. Malik, R.; Zhou, F.; Ceder, G., Kinetics of Non-Equilibrium Lithium Incorporation in $LiFePO_4$. *Nat. Mater.* **2011,** *10* (8), 587-590.

14. Bai, P.; Cogswell, D. A.; Bazant, M. Z., Suppression of Phase Separation in $LiFePO_4$ Nanoparticles during Battery Discharge. *Nano Lett.* **2011,** *11* (11), 4890-4896.

15. Orikasa, Y.; Maeda, T.; Koyama, Y.; Murayama, H.; Fukuda, K.; Tanida, H.; Arai, H.; Matsubara, E.; Uchimoto, Y.; Ogumi, Z., Direct Observation of a Metastable Crystal Phase of Li_xFePO_4 under Electrochemical Phase Transition. *J. Am. Chem. Soc.* **2013,** *135* (15), 5497-5500.

16. Zhang, X. Y.; van Hulzen, M.; Singh, D. P.; Brownrigg, A.; Wright, J. P.; van Dijk, N. H.; Wagemaker, M., Rate-Induced Solubility and Suppression of the First-Order Phase Transition in Olivine $LiFePO_4$. *Nano Lett.* **2014,** *14* (5), 2279-2285.

17. Liu, H.; Strobridge, F. C.; Borkiewicz, O. J.; Wiaderek, K. M.; Chapman, K. W.; Chupas, P. J.; Grey, C. P., Capturing Metastable Structures during High-Rate Cycling of $LiFePO_4$ Nanoparticle

Electrodes. *Science* **2014,** *344* (6191).

18. Zhang, X. Y.; van Hulzen, M.; Singh, D. P.; Brownrigg, A.; Wright, J. P.; van Dijk, N. H.; Wagemaker, M., Direct View on the Phase Evolution in Individual $LiFePO_4$ Nanoparticles during Li-Ion Battery Cycling. *Nat. Commun.* **2015,** *6*.

19. Lim, J.; Li, Y. Y.; Alsem, D. H.; So, H.; Lee, S. C.; Bai, P.; Cogswell, D. A.; Liu, X. Z.; Jin, N.; Yu, Y. S.; Salmon, N. J.; Shapiro, D. A.; Bazant, M. Z.; Tyliszczak, T.; Chueh, W. C., Origin and Hysteresis of Lithium Compositional Spatiodynamics within Battery Primary Particles. *Science* **2016,** *353* (6299), 566-571.

20. Reddy, M. A.; Fichtner, M., Batteries based on fluoride shuttle. *J. Mater. Chem.* **2011,** *21* (43), 17059-17062.

21. Rongeat, C.; Reddy, M. A.; Witter, R.; Fichtner, M., Nanostructured Fluorite-Type Fluorides As Electrolytes for Fluoride Ion Batteries. *J. Phys. Chem. C* **2013,** *117* (10), 4943-4950.

22. Rongeat, C.; Reddy, M. A.; Diemant, T.; Behm, R. J.; Fichtner, M., Development of new anode composite materials for fluoride ion batteries. *J. Mater. Chem. A* **2014,** *2* (48), 20861-20872.

23. Nowroozi, M. A.; Wissel, K.; Rohrer, J.; Munnangi, A. R.; Clemens, O., $LaSrMnO_4$: Reversible electrochemical intercalation of fluoride ions in the context of fluoride ion batteries. *Chem. Mater.* **2017,** *29* (8), 3441-3453.

24. Nowroozi, M. A.; Ivlev, S.; Rohrer, J.; Clemens, O., La_2CoO_4: A new intercalation based cathode material for fluoride ion batteries with improved cycling stability. *J. Mater. Chem. A* **2018,** *6* (11), 4658-4669.

25. Nowroozi, M. A.; de Laune, B.; Clemens, O., Reversible Electrochemical Intercalation and Deintercalation of Fluoride Ions into Host Lattices with Schafarzikite-Type Structure. *Chemistryopen* **2018,** *7* (8), 617-623.

26. Zhang, L.; Reddy, M. A.; Gao, P.; Fichtner, M., Development of dense solid state thin-film electrolyte for fluoride ion batteries. *J. Alloys Compd.* **2016,** *684*, 733-738.

27. Zhang, L.; Reddy, M. A.; Gao, P.; Diemant, T.; Behm, R. J.; Fichtner, M., Study of all solid-state rechargeable fluoride ion batteries based on thin-film electrolyte. *J. Solid State Electrochem.* **2017,** *21* (5), 1243-1251.

28. Zhang, L.; Reddy, M. A.; Fichtner, M., Electrochemical performance of all solid-state fluoride-ion batteries based on thin-film electrolyte using alternative conductive additives and anodes. *J. Solid State Electrochem.* **2018,** *22* (4), 997-1006.

Chapter 2.

High rate performance of dual-substituted $LiFePO_4$ based on controlling metastable intermediate phase

High rate capability is one of the most important properties in Li-ion batteries for electric vehicle and/or energy grid use. Herein, a high-power electrode material consisting of dual-substituted $LiFePO_4$ by zirconium and silicon, $Li(Fe_{0.95}Zr_{0.05})(P_{0.9}Si_{0.1})O_4$, was developed as it exhibits small lattice volume change between Li-rich and Li-poor phases. The dual-substituted cathode exhibited 1.1−4.4 times larger charge/discharge capacities for upper 10 C rates than that of the undoped material. Time-resolved XRD measurements at the high rate of 10 C revealed the formation of a metastable intermediate phase during the Li intercalation/deintercalation processes which triggers the continuous phase transition in $Li(Fe_{0.95}Zr_{0.05})(P_{0.9}Si_{0.1})O_4$ with moderation of the lattice mismatch. Controlling the lattice volume change between the initial and end phase of the intercalation materials is key to achieving high rate capabilities.

2.1. Introduction

The cathode material, $LiFePO_4$, whose specific theoretical capacity is 170 mAh/g with an average voltage of 3.4 V vs Li^+/Li, exhibits excellent performance in batteries.[1-3] Its strong polyanionic framework enables the extraction of one Li ion without irreversible structure transformation. The Fe^{2+}/Fe^{3+} redox potential in the olivine structure is higher than that in the layered structure because the Fe–O covalency in octahedral FeO_6 is weakened by strong covalency of the P–O bond in the neighboring tetrahedral PO_4.[4] The intrinsic high thermal/chemical stability and long cycle life of the material make it suitable for use in energy storage systems. Li-ion intercalation/deintercalation in $LiFePO_4$ proceeds via a two-phase reaction between the Li-rich $Li_{1-\beta}FePO_4$ (LFP) and Li-poor $Li_\alpha FePO_4$ (FP) phases.[1, 5, 6] Li-ion diffusion occurs along the *b* axis,[7, 8] as the phase boundary forms a thermodynamically favorable *bc* plane or kinetically favorable *ac* plane.[8-11] Although nucleation and subsequent growth reactions are considered to be a kinetic disadvantage because of the associated large lattice volume change, $LiFePO_4$ nevertheless exhibits high charging/discharging rates. A metastable intermediate phase, which forms during the charging/discharging processes, decreases the extent of lattice mismatch between LFP and FP, resulting in high rate performance.[12] Therefore, reduction of the lattice mismatch between the LFP and FP phases is anticipated to be advantageous for a faster phase transition. Recently $Li(Fe_{1-x}Zr_x)(P_{1-2x}Si_{2x})O_4$, which is dual-substituted $LiFePO_4$ with zirconium and silicon, has been reported for the small lattice volume change.[13] Although the higher dopant content of x in $Li(Fe_{1-x}Zr_x)(P_{1-2x}Si_{2x})O_4$ offers the smaller volume change, it is a trade-off for the lower theoretical capacity as the iron is the only redox active element. Herein, we examined the rate performance and phase transition behavior of the optimized dopant content of $Li(Fe_{1-x}Zr_x)(P_{1-2x}Si_{2x})O_4$ or $Li(Fe_{0.95}Zr_{0.05})(P_{0.9}Si_{0.1})O_4$, with the reduced lattice mismatch as well as the acceptable capacity. $Li(Fe_{0.95}Zr_{0.05})(P_{0.9}Si_{0.1})O_4$ exhibited a higher rate performance than that of $LiFePO_4$. The metastable intermediate phase of $Li(Fe_{0.95}Zr_{0.05})(P_{0.9}Si_{0.1})O_4$ appeared for a wider range of Li contents than that of $LiFePO_4$ during the charging/discharging processes, resulting in the rate performance improvement.

2.2. Experimental

$LiFePO_4$ and $Li(Fe_{0.95}Zr_{0.05})(P_{0.9}Si_{0.1})O_4$ were synthesized by a solid state reaction. The crystal structure of the electrochemically delithiated samples were analyzed by X-ray

diffraction (XRD) with the wavelength of 0.699292(4) Å, which was calibrated using CeO_2, at a beam line BL02B2 of SPring-8 (Hyogo, Japan). The particle size of the prepared samples were confirmed by scanning electron microscopy (SEM) (S-3400 N, Hitachi HighTech Co.).

The electrode was prepared by mixing 80% active material, 10% carbon black (Denka Company Limited), and 10% polyvinylidene fluoride (Kureha Corporation) with 1-methyl-2-pyrrolidinone as a solvent (Wako Pure Chemical Industries, Ltd.). The composite electrode was placed in laminate-type cells in an Ar-filled glove box with lithium metal as counter and reference electrodes. $LiPF_6$ (1 M) in a 3:7 volume ratio of ethylene carbonate and ethyl methyl carbonate (Kishida Chemical Co., Ltd.) was used as the electrolyte. The laminate-type cell was assembled in the same manner as previously reported.[12] Galvanostatic charge/discharge measurements were conducted from 0.2C (C = 170 mA/g) to 50C rates at 25 °C after a pretreatment of one cycle at a 0.2C rate and two cycles at a 0.5C rate. The cut-off voltage was set at 4.3 V on the charge and 2.0 V on the discharge.

Time-resolved X-ray diffraction (TR-XRD) measurements were performed at a beam line BL28XU of SPring-8 using a 1D detector (Mythen 1K, Dectris). The wavelength was set at 0.619862(2) Å, which was calibrated using CeO_2. The TR-XRD data were collected in the 2θ range of 10 to 13° with an exposure time of 1 s every 15 s.

First-principles calculations were performed using the projector augmented wave (PAW) method,[14, 15] as implemented in the VASP code.[16-18] The configurations of the valence electrons in the PAW potentials are $2s^1$ for Li, $3p^6\ 3d^6\ 4s^2$ for Fe, $3s^2\ 3p^3$ for P, $4s^2\ 4p^6\ 4d^2\ 5s^2$ for Zr and $3s^2\ 3p^2$ for Si, $2s^2\ 2p^4$ for O, respectively. All calculations were carried out under spin-polarized ferromagnetic conditions. GGA+U approach[19] was used to take into account strong correlation effect of 3d orbital. The value of U potential for Fe 3d orbital was set to be 4.3 eV.[20] This value is equal to an averaged one of the U parameters for Fe^{2+} and Fe^{3+}.[21] Crystal structures were fully optimized until that all residual forces acting on atoms become smaller than 0.02 eV/Å. Supercell models, those size is $1 \times 1 \times 2$ of a $LiFePO_4$ unit cell composed of 56 atoms, were constructed for computation of the $Li(Fe_{0.95}Zr_{0.05})(P_{0.9}Si_{0.1})O_4$ system. One Zr and two Si atoms were simultaneously substituted for the sites of Fe and P in the supercell, respectively. In total 28 kinds of co-doped models ($Li_8Fe_7ZrP_6Si_2O_{32}$) with symmetrically nonequivalent configurations of Zr and Si atoms were calculated. From the series of structure optimization calculations of the co-doped supercells, the most stable configuration was determined as shown in

Figure 2.1. This model was used for detail investigation.

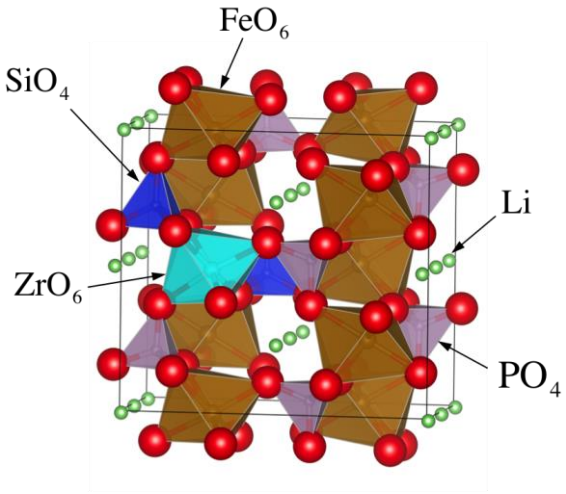

Figure 2.1. *The most stable configuration of Zr and Si among the co-doped models of* $Li_8Fe_7ZrP_6Si_2O_{32}$ *found by the present DFT calculations.*

2.3. Results and Discussion

The lattice parameters of each sample were similar to those reported previously, and the lattice volume change between the two phases decreases from 6.6% to 6.3% after the dual-substitution, as summarized in **Table 2.1**[13].

Table 2.1. *Lattice constants and volume change between lithiated and delithiated phases of* $LiFePO_4$ *and* $Li(Fe_{0.95}Zr_{0.05})(P_{0.9}Si_{0.1})O_4$ *calculated from the electrochemically delithiated samples of* $Li_{0.5}FePO_4$ *and* $Li_{0.5}(Fe_{0.95}Zr_{0.05})(P_{0.9}Si_{0.1})O_4$*, respectively.*

	a [Å]	*b* [Å]	*c* [Å]	*V* [Å]	ΔV/V [%]
$LiFePO_4$	10.3262(8)	6.0048(5)	4.6908(0)	290.86(6)	-
$FePO_4$	9.8177(0)	5.7894(9)	4.7816(3)	271.78(5)	6.6
$Li(Fe_{0.95}Zr_{0.05})(P_{0.9}Si_{0.1})O_4$	10.3140(3)	6.0007(5)	4.6919(8)	290.39(6)	-
$(Fe_{0.95}Zr_{0.05})(P_{0.9}Si_{0.1})O_4$	9.8280(7)	5.7944(1)	4.7800(4)	272.21(3)	6.3

The dual-substitution of $LiFePO_4$ provides considerable enhancement of the rate performance of the material, as shown in **Figure 2.2**. At a low rate of 1C, both $LiFePO_4$ and $Li(Fe_{0.95}Zr_{0.05})(P_{0.9}Si_{0.1})O_4$ show almost the same capacity of 120 mAh/g. The voltage curves of the two materials are exactly overlapping except for at the beginning of the

charge and the end of the discharge. However, this fractional feature does not significantly influence the obtained capacity. At the high rate of 10C, the capacity of $Li(Fe_{0.95}Zr_{0.05})(P_{0.9}Si_{0.1})O_4$ is maintained at 90 mAh/g, although that of $LiFePO_4$ falls to 75 mAh/g. The difference between the capacities of the materials grows larger with increasing current rates, and $Li(Fe_{0.95}Zr_{0.05})(P_{0.9}Si_{0.1})O_4$ can charge and discharge 1.1–4.4 times longer than that of $LiFePO_4$ at rate greater than 10 C.

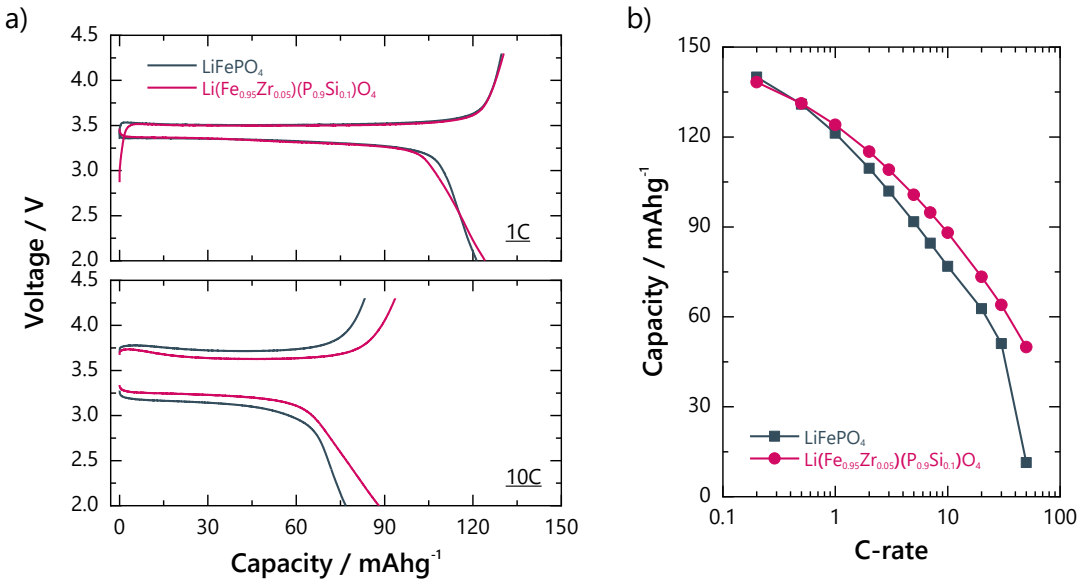

Figure 2.2. *Rate performance under galvanostatic charge/discharge cycling. (a) Voltage curves at rates of 1C (top) and 10C (bottom) for $LiFePO_4$ and $Li(Fe_{0.95}Zr_{0.05})(P_{0.9}Si_{0.1})O_4$. (b) Discharge capacities at various C-rates for $LiFePO_4$ and $Li(Fe_{0.95}Zr_{0.05})(P_{0.9}Si_{0.1})O_4$. The gray line and rectangle, and red line and circle denote $LiFePO_4$ and $Li(Fe_{0.95}Zr_{0.05})(P_{0.9}Si_{0.1})O_4$, respectively.*

In addition, quasi-open-circuit-voltage (quasi-OCV) measurements showed that the overpotential of $Li(Fe_{0.95}Zr_{0.05})(P_{0.9}Si_{0.1})O_4$ is smaller than that of $LiFePO_4$, indicating that the intercalation reaction of $Li(Fe_{0.95}Zr_{0.05})(P_{0.9}Si_{0.1})O_4$ is faster than that of $LiFePO_4$ (**Figure 2.3**). Note that the dual-substituted electrode exhibited improved rate capability without sacrificing accumulated capacity at low rates.

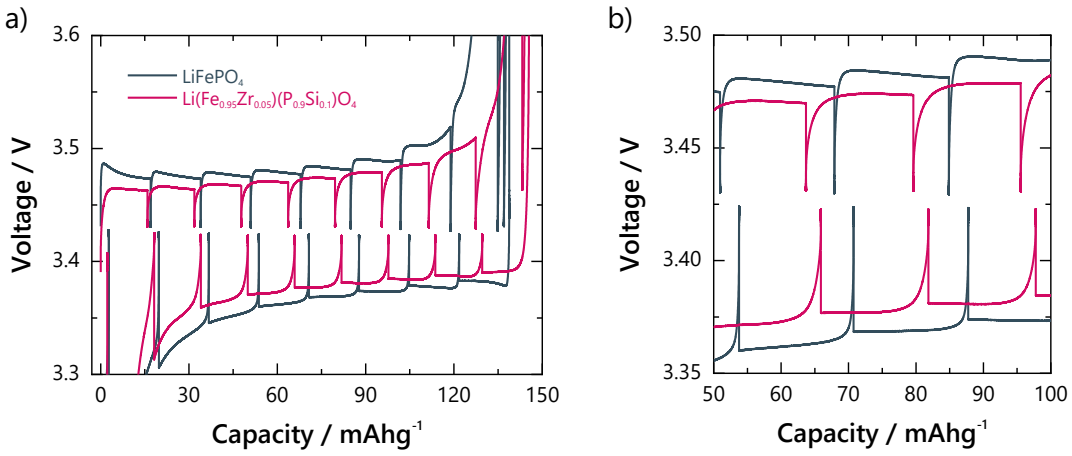

Figure 2.3. *(a) Quasi-OCV curves and (b) their magnification of $LiFePO_4$ and $Li(Fe_{0.95}Zr_{0.05})(P_{0.9}Si_{0.1})O_4$. The gray and red lines denote data from $LiFePO_4$ and $Li(Fe_{0.95}Zr_{0.05})(P_{0.9}Si_{0.1})O_4$, respectively.*

For the static condition, two-phase behavior was observed in both samples. The diffraction patterns originating from the isolated two phases and the flat voltage of the quasi-OCV after relaxation represent a typical two-phase nature (**Figure 2.3**and **Figure 2.4**). It was found that the particle size as well as the crystalline size are around 100 nm for both $LiFePO_4$ and $Li(Fe_{0.95}Zr_{0.05})(P_{0.9}Si_{0.1})O_4$ due to XRD patterns and SEM images of the pristine samples (**Figure 2.4** and **Figure 2.5**).

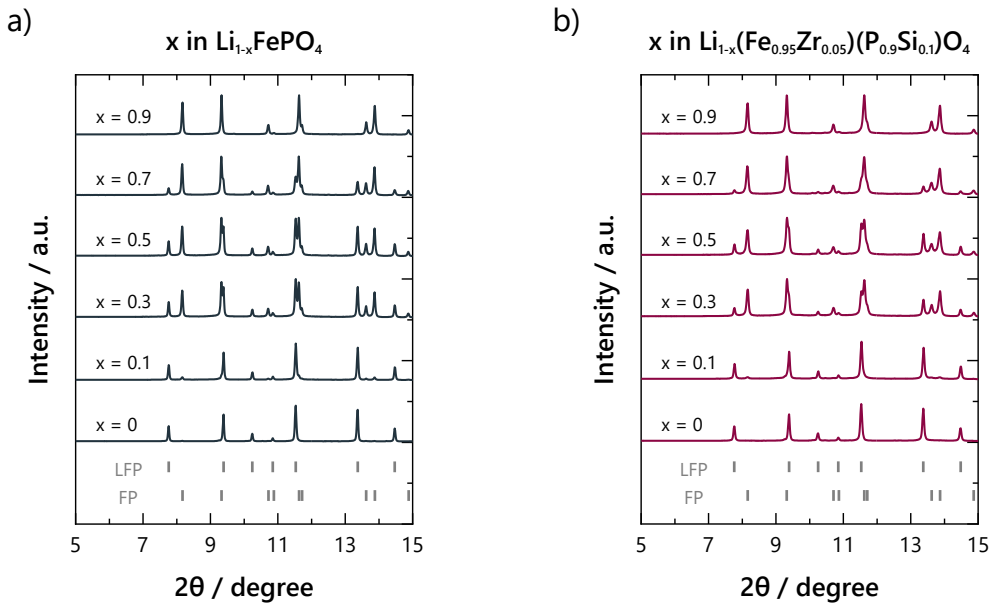

Figure 2.4. *ex-situ XRD patterns of (a) $LiFePO_4$ and (b) $Li(Fe_{0.95}Zr_{0.05})(P_{0.9}Si_{0.1})O_4$. All samples were prepared for the first charge process and relaxed under an open circuit for 48 h with electrochemically delithiated electrodes.*

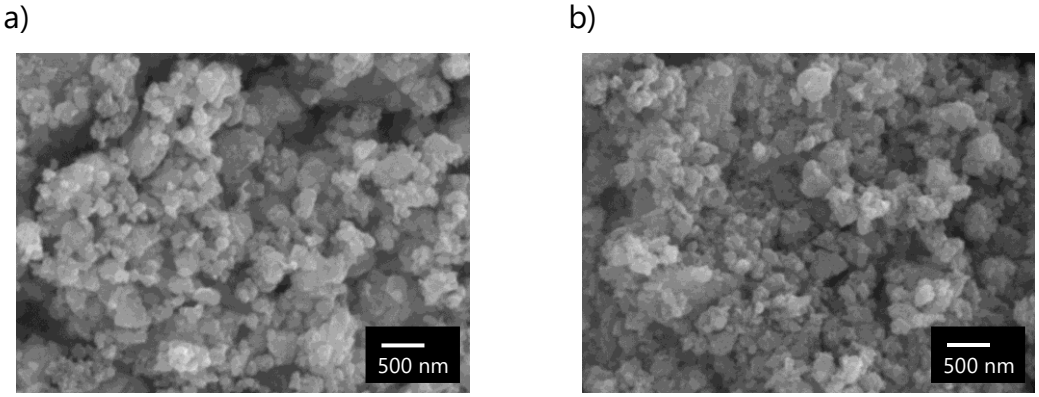

Figure 2.5. *SEM images of (a) $LiFePO_4$ and (b) $Li(Fe_{0.95}Zr_{0.05})(P_{0.9}Si_{0.1})O_4$.*

The dynamic phase transition was examined under battery operation at the high rate of 10C by time-resolved XRD measurement. In both samples the metastable intermediate solid solution phase (LxFP) was observed in addition to the LFP and the FP during galvanostatic charge/discharge cycling, as shown in **Figure 2.6**. However, the metastable intermediate solid solution phase in $LiFePO_4$ emerges only under a narrow range of conditions (the end of the discharge and beginning of the charge), whereas the metastable intermediate solid solution phase in $Li(Fe_{0.95}Zr_{0.05})(P_{0.9}Si_{0.1})O_4$ exists over a wide range of conditions. The peak position of the metastable intermediate solid solution phase continuously shifts, indicating a quasi single-phase reaction.

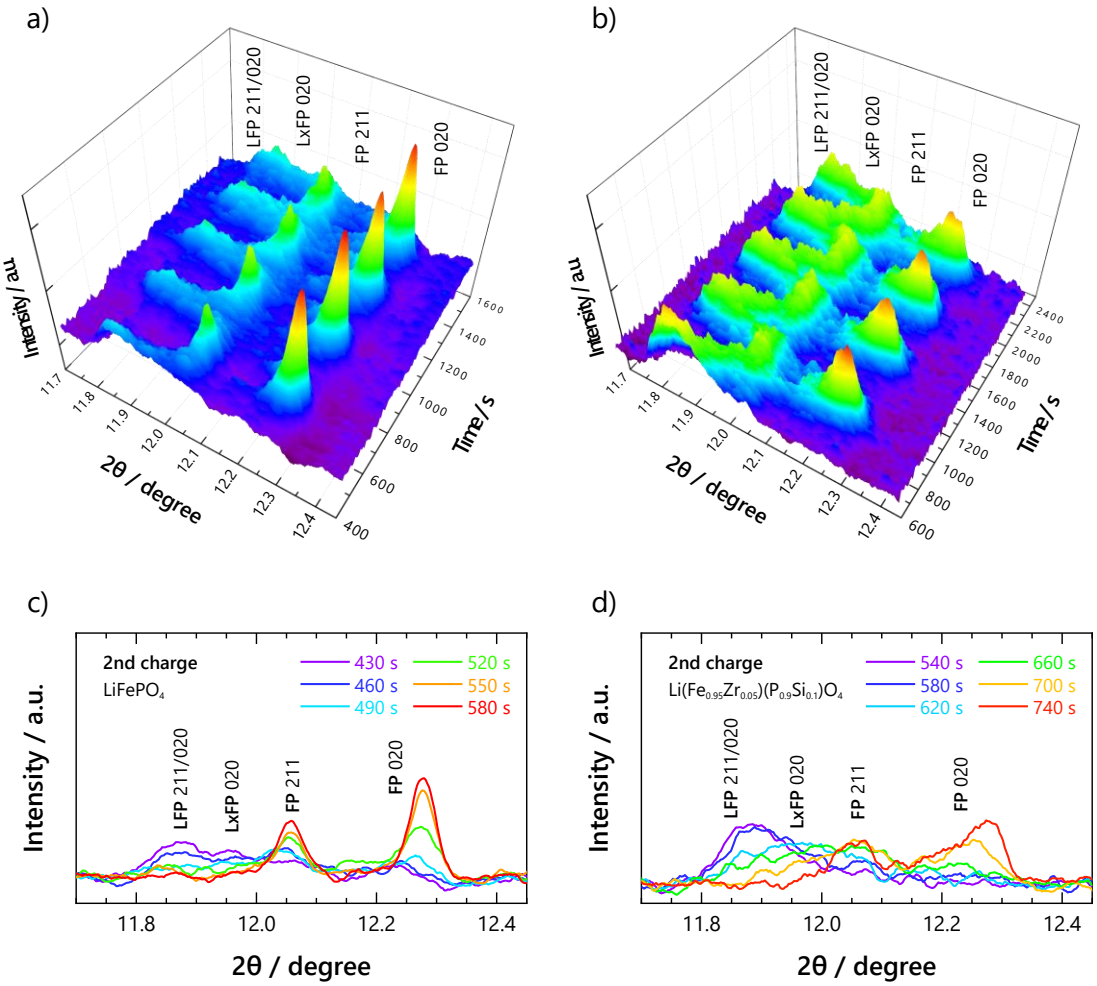

Figure 2.6. *TR-XRD patterns during galvanostatic charge/discharge cycling at a high rate of 10C. Charging process from the 2nd to the 5th cycle of (a) $LiFePO_4$ and (b) $Li(Fe_{0.95}Zr_{0.05})(P_{0.9}Si_{0.1})O_4$. The XRD patterns during the 2nd charge process for (c) $LiFePO_4$ and (d) $Li(Fe_{0.95}Zr_{0.05})(P_{0.9}Si_{0.1})O_4$.*

A schematic illustration of the improved rate performance of $LiFePO_4$ by dual-substitution with zirconium and silicon is shown in **Figure 2.7**. Dual-substitution reduces the lattice volume change of $LiFePO_4$ between LFP and FP phases from 6.6% to 6.3%. Reduction of the lattice strain at the phase boundary leads to enhanced rate capability because the quasi single-phase reaction proceeds over a wide Li compositional range. Once the phase transition barrier is removed, Li ion transport occurs homogeneously in the host structure.[22-24] Because Li-ion insertion/extraction is not restricted within phase boundaries, the specific surface area for the single-phase reaction is larger than that for the two-phase reaction. The competing disproportionation reaction

model can be applied to $Li(Fe_{0.95}Zr_{0.05})(P_{0.9}Si_{0.1})O_4$ as well as $LiFePO_4$ to explain the influence of the metastable intermediate solid solution phase.[25] When the metastable intermediate solid solution phase evolves during the reaction under high current rates, it is more stable in $Li(Fe_{0.95}Zr_{0.05})(P_{0.9}Si_{0.1})O_4$ than in $LiFePO_4$ due to smaller strain energies within the phase boundary. The slow phase decomposition to two isolated phases enables the extensive participation of the metastable intermediate solid solution phase in $Li(Fe_{0.95}Zr_{0.05})(P_{0.9}Si_{0.1})O_4$.

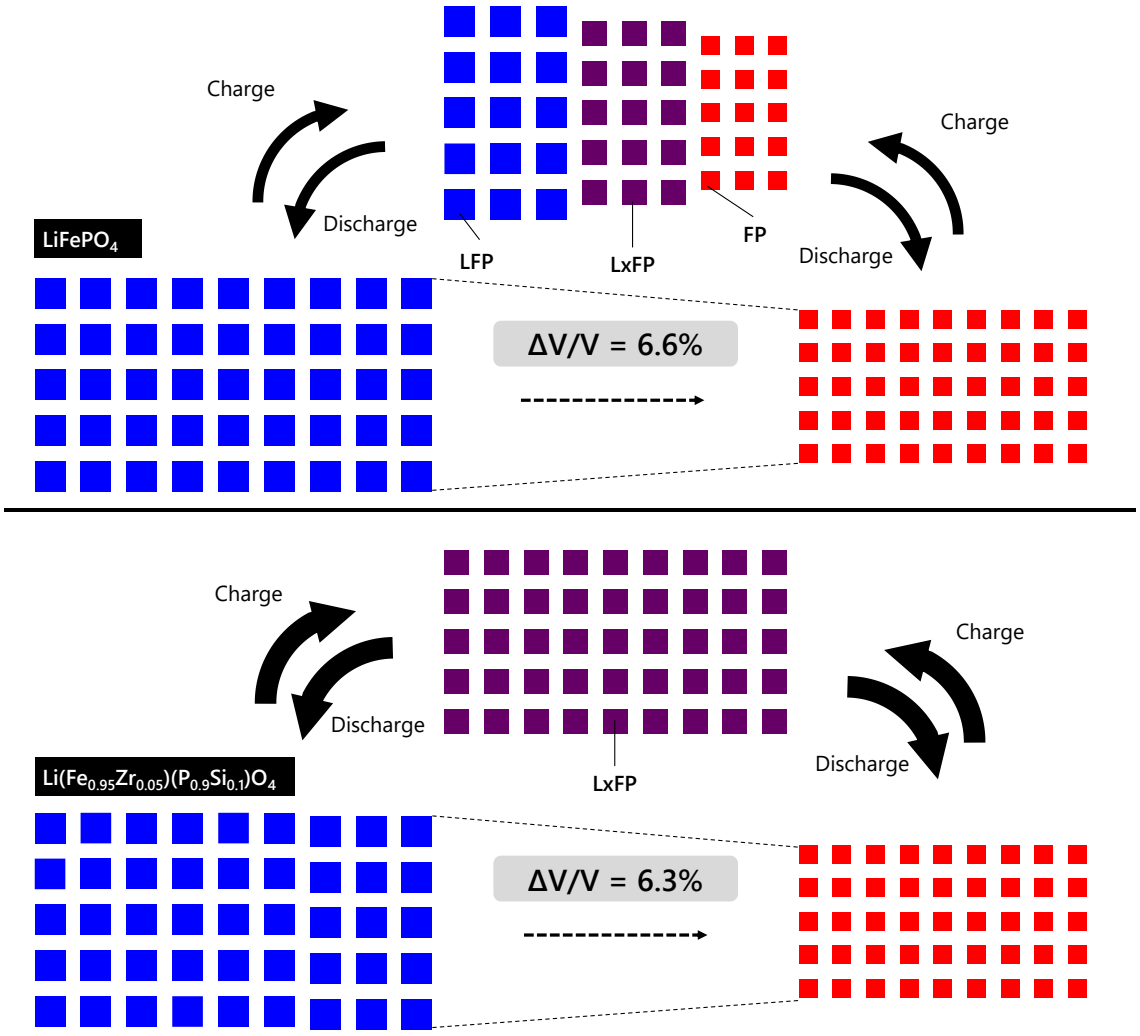

Figure 2.7. *Phase transition model for $LiFePO_4$ and $Li(Fe_{0.95}Zr_{0.05})(P_{0.9}Si_{0.1})O_4$ under high rate charge/discharge cycling.*

With decreasing temperature, the enhancement of the rate performance is smaller in $Li(Fe_{0.95}Zr_{0.05})(P_{0.9}Si_{0.1})O_4$ as shown in **Figure 2.8**. As the metastable intermediate phase of

$LiFePO_4$ is no longer the transient solid solution and predominant throughout the phase transition at –5°C,[25] the difference of the lattice volume change for both samples is irrelevant to the rate performance at lower temperature. This supports the role of the metastable intermediate phase being responsible for the phase transition kinetics. Note that both samples have almost the same particle size, around 100 nm, indicating that particle size effects[26, 27] are negligible.

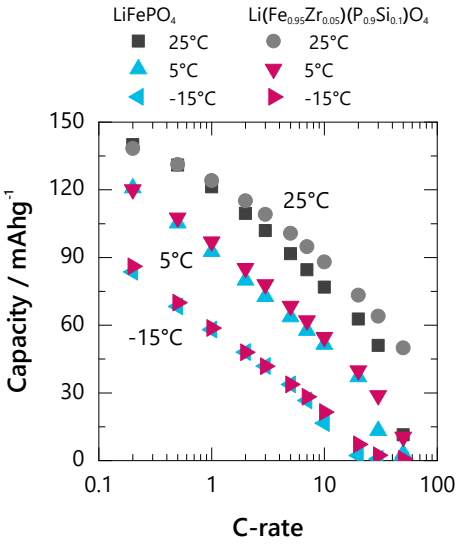

Figure 2.8. *Temperature dependent discharge capacity at various C-rates for $LiFePO_4$ and $Li(Fe_{0.95}Zr_{0.05})(P_{0.9}Si_{0.1})O_4$. The blue and red lines denote data from LiFePO4 and $Li(Fe_{0.95}Zr_{0.05})(P_{0.9}Si_{0.1})O_4$, respectively. The data at 25°C shown in* ***Figure 2.2*** *displays as reference.*

The dual-substitution effect by specific elements of Zr and Si was investigated by first principle calculation. The DOS calculation for both samples was conducted as shown in **Figure 2.9**. The supercell model was applied to $Li(Fe_{0.95}Zr_{0.05})(P_{0.9}Si_{0.1})O_4$ and the formula unit is $Li_8Fe_7ZrP_6Si_2O_{32}$. The calculated band gap of LiFePO4 is 3.7 eV, corresponding to the previous report.[28] For $Li_8Fe_7ZrP_6Si_2O_{32}$, isolated impurity states of Zr appears near the Fermi level and reduces the band gap to 2.8 eV. The narrow band gap might provide the high electronic conductivity, which contributes to triggering the fast charge transfer and the subsequent crystal structure change. The Fe^{2+}/Fe^{3+} redox potential is slightly lower in $Li_8Fe_7ZrP_6Si_2O_{32}$ (3.30 V) than in $LiFePO_4$ (3.38 V, **Table 2.2**), as a result of the inductive effect from oxygen forming weaker bonds within $(P_{0.9}Si_{0.1})O_4^{3.1-}$ than PO_4^{3-}. This is consistent with the quasi-OCV measurements (**Figure 2.3**).

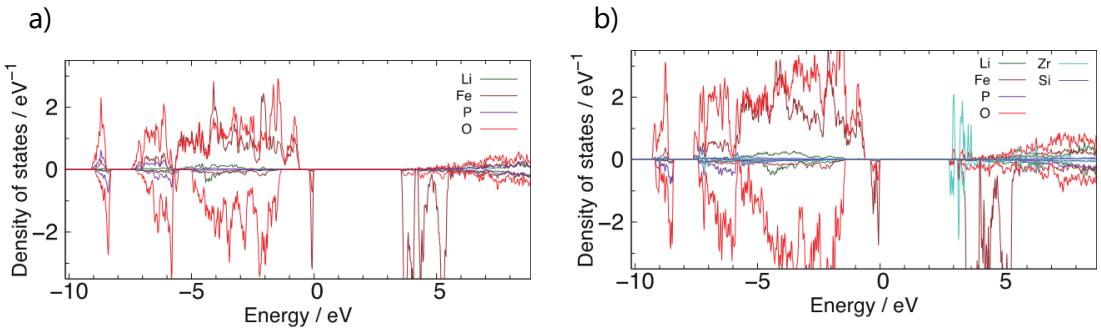

***Figure* 2.9.** *Density of states of all elements in the initial state. (a) $LiFePO_4$ and (b) $Li_8Fe_7ZrP_6Si_2O_{32}$. Green, brown, purple, red, light blue, and blue denote Li, Fe, P, O, Zr, and Si, respectively.*

***Table* 2.2.** *Parameters of $LiFePO_4$ and $Li_8Fe_7ZrP_6Si_2O_{32}$ obtained from DFT calculations.*

	$LiFePO_4$	$Li_8Fe_7ZrP_6Si_2O_{32}$
Band gap	3.7 eV	2.8 eV
Voltage vs. Li^+/Li	3.38 V	3.30 V
Volume change between lithiated and delithiated phase	3.8%	2.5%

The migration energy was also calculated depending on Li-ion diffusion pathways for both samples as shown in **Figure 2.10**. For $LiFePO_4$, one type of the diffusion pathway was found and the maximum migration energy is 0.35 eV, while for $Li_8Fe_7ZrP_6Si_2O_{32}$, four types of the diffusion pathways were found and the maximum migration energy is 0.38–0.56 eV. In the olivine structure, Li ions transport along one direction[7] so that the maximum value of the migration energy governs the diffusivity. As there is no advantage for the doped sample, it is suggested the Li intercalation kinetics strongly depends on the phase transition rate, not the diffusion effect within the material. The metastable intermediate phase, which determines the rate capability, vanishes after 30 minutes during the relaxation condition.[12] It is doubtful that the parameters obtained from the relaxation condition are crucial to understand the intercalation reaction with the participation of the metastable intermediate phase.

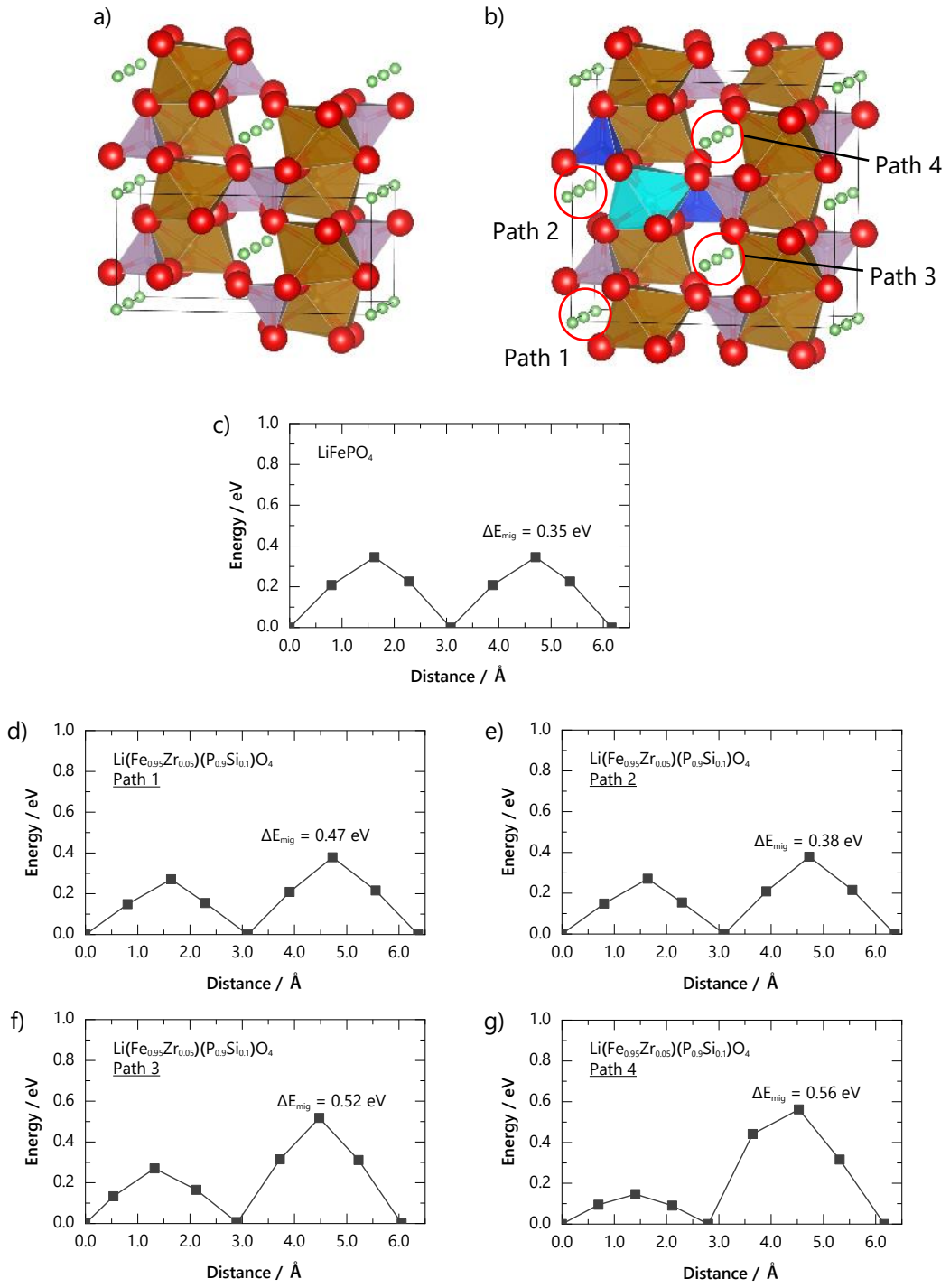

Figure 2.10. *Crystal structure of (a) $LiFePO_4$ and (b) $Li_8Fe_7ZrP_6Si_2O_{32}$. Green, brown, purple, red, light blue, and blue denote Li, Fe, P, O, Zr, and Si, respectively. Migration energy of (c) $LiFePO_4$ and $Li_8Fe_7ZrP_6Si_2O_{32}$ on (d) path 1, (e) path 2, (f) path 3, and (g) path 4. The migration energy around tetravalent Zr is higher than that of divalent or trivalent Fe due to the repulsion with Li ion.*

2.4. Conclusion

Dual-substitution with reduced lattice mismatch in $LiFePO_4$ enhances the cycle life[13] and maintains the rate performance by preserving the intrinsic nature of the material. This finding is important for the design of materials with fast charge/discharge characteristics.

References

1. Padhi, A. K.; Nanjundaswamy, K. S.; Goodenough, J. B., Phospho-Olivines as Positive-Electrode Materials for Rechargeable Lithium Batteries. *J. Electrochem. Soc.* **1997,** *144* (4), 1188-1194.

2. Chung, S. Y.; Bloking, J. T.; Chiang, Y. M., Electronically Conductive Phospho-Olivines as Lithium Storage Electrodes. *Nat. Mater.* **2002,** *1* (2), 123-128.

3. Kang, B.; Ceder, G., Battery Materials for Ultrafast Charging and Discharging. *Nature* **2009,** *458* (7235), 190-193.

4. Padhi, A. K.; Nanjundaswamy, K. S.; Masquelier, C.; Okada, S.; Goodenough, J. B., Effect of Structure on the Fe^{3+}/Fe^{2+} Redox Couple in Iron Phosphates. *J. Electrochem. Soc.* **1997,** *144* (5), 1609-1613.

5. Delacourt, C.; Poizot, P.; Tarascon, J. M.; Masquelier, C., The Existence of a Temperature-Driven Solid Solution in Li_xFePO_4 for $0 <= x <= 1$. *Nat. Mater.* **2005,** *4* (3), 254-260.

6. Yamada, A.; Koizumi, H.; Nishimura, S. I.; Sonoyama, N.; Kanno, R.; Yonemura, M.; Nakamura, T.; Kobayashi, Y., Room-Temperature Miscibility Gap in Li_xFePO_4. *Nat. Mater.* **2006,** *5* (5), 357-360.

7. Morgan, D.; Van der Ven, A.; Ceder, G., Li Conductivity in Li_xMPO_4 (M = Mn, Fe, Co, Ni) Olivine Materials. *Electrochem. Solid-State Lett.* **2004,** *7* (2), A30-A32.

8. Chen, G. Y.; Song, X. Y.; Richardson, T. J., Electron Microscopy Study of the $LiFePO_4$ to $FePO_4$ Phase Transition. *Electrochem. Solid-State Lett.* **2006,** *9* (6), A295-A298.

9. Cogswell, D. A.; Bazant, M. Z., Coherency Strain and the Kinetics of Phase Separation in $LiFePO_4$ Nanoparticles. *ACS Nano* **2012,** *6* (3), 2215-2225.

10. Abdellahi, A.; Akyildiz, O.; Malik, R.; Thornton, K.; Ceder, G., Particle-size and Morphology Dependence of the Preferred Interface Orientation in $LiFePO_4$ Nano-particles. *J Mater. Chem. A* **2014,** *2* (37), 15437-15447.

11. Abdellahi, A.; Akyildiz, O.; Malik, R.; Thornton, K.; Ceder, G., The Thermodynamic Stability of Intermediate Solid Solutions in $LiFePO_4$ Nanoparticles. *J Mater. Chem. A* **2016,** *4* (15), 5436-5447.

12. Orikasa, Y.; Maeda, T.; Koyama, Y.; Murayama, H.; Fukuda, K.; Tanida, H.; Arai, H.; Matsubara, E.; Uchimoto, Y.; Ogumi, Z., Direct Observation of a Metastable Crystal Phase of Li_xFePO_4 under Electrochemical Phase Transition. *J. Am. Chem. Soc.* **2013,** *135* (15), 5497-5500.

13. Nishijima, M.; Ootani, T.; Kamimura, Y.; Sueki, T.; Esaki, S.; Murai, S.; Fujita, K.; Tanaka, K.; Ohira, K.; Koyama, Y.; Tanaka, I., Accelerated Discovery of Cathode Materials with Prolonged Cycle Life for Lithium-Ion Battery. *Nat. Commun.* **2014,** *5*.

14. Blochl, P. E., Projector Augmented-wave Method. *Phys. Rev. B* **1994,** *50* (24), 17953-17979.

15. Kresse, G.; Joubert, D., From Ultrasoft Pseudopotentials to the Projector Augmented-wave Method. *Phys. Rev. B* **1999,** *59* (3), 1758-1775.

16. Kresse, G.; Hafner, J., Abinitio Molecular-Dynamics for Liquid-Metals. *Phys. Rev. B* **1993,** *47* (1), 558-561.

17. Kresse, G.; Furthmuller, J., Efficient Iterative Schemes for Ab Initio Total-Energy Calculations Using a Plane-wave Basis Set. *Phys. Rev. B* **1996,** *54* (16), 11169-11186.

18. Kresse, G.; Furthmuller, J., Efficiency of Ab-initio Total Energy Calculations for Metals and Semiconductors Using a Plane-wave Basis Set. *Comput. Mater. Sci.* **1996,** *6* (1), 15-50.

19. Dudarev, S. L.; Botton, G. A.; Savrasov, S. Y.; Humphreys, C. J.; Sutton, A. P., Electron-energy-loss Spectra and the Structural Stability of Nickel Oxide: An LSDA+U Study. *Phys. Rev. B* **1998,** *57* (3), 1505-1509.

20. Dathar, G. K. P.; Sheppard, D.; Stevenson, K. J.; Henkelman, G., Calculations of Li-ion Diffusion in Olivine Phosphates. *Chem. Mater.* **2011,** *23* (17), 4032-4037.

21. Zhou, F.; Cococcioni, M.; Marianetti, C. A.; Morgan, D.; Ceder, G., First-Principles Prediction of Redox Potentials in Transition-metal Compounds with LDA + U. *Phys. Rev. B* **2004,** *70* (23).

22. Bai, P.; Cogswell, D. A.; Bazant, M. Z., Suppression of Phase Separation in $LiFePO_4$ Nanoparticles during Battery Discharge. *Nano Lett.* **2011,** *11* (11), 4890-4896.

23. Malik, R.; Zhou, F.; Ceder, G., Kinetics of Non-Equilibrium Lithium Incorporation in $LiFePO_4$. *Nat. Mater.* **2011,** *10* (8), 587-590.

24. Niu, J. J.; Kushima, A.; Qian, X. F.; Qi, L.; Xiang, K.; Chiang, Y. M.; Li, J., In Situ Observation of Random Solid Solution Zone in $LiFePO_4$ Electrode. *Nano Lett.* **2014,** *14* (7), 4005-4010.

25. Koyama, Y.; Uyama, T.; Orikasa, Y.; Naka, T.; Komatsu, H.; Shimoda, K.; Murayama, H.; Fukuda, K.; Arai, H.; Matsubara, E.; Uchimoto, Y.; Ogumi, Z., Hidden Two-Step Phase Transition and Competing Reaction Pathways in $LiFePO_4$. *Chem. Mater.* **2017,** *29* (7), 2855-2863.

26. Meethong, N.; Huang, H. Y. S.; Carter, W. C.; Chiang, Y. M., Size-Dependent Lithium Miscibility Gap in Nanoscale $Li_{1-x}FePO_4$. *Electrochem. Solid-State Lett.* **2007,** *10* (5), A134-A138.

27. Wagemaker, M.; Singh, D. P.; Borghols, W. J. H.; Lafont, U.; Haverkate, L.; Peterson, V. K.; Mulder, F. M., Dynamic Solubility Limits in Nanosized Olivine $LiFePO_4$. *J. Am. Chem. Soc.* **2011,** *133* (26), 10222-10228.

28. Zhou, F.; Kang, K. S.; Maxisch, T.; Ceder, G.; Morgan, D., The electronic structure and band gap of LiFePO4 and LiMnPO4. *Solid State Commun.* **2004,** *132* (3-4), 181-186.

Chapter 3.
Current-induced hysteretic phase transition behavior via intermediate solid solution phase in $LiFePO_4$

Lithium-ion batteries play a fundamental role in social infrastructure and electric vehicles. The promising electrode material of $LiFePO_4$ exhibits high-rate performance due to the crucial but controversial act of the metastable intermediate phase in addition to the end-member of the two phases at room temperature. Here we demonstrate the electrochemical and crystal structural behavior of the intermediate phase in Li_xFePO_4 to be thermodynamically stable at elevated temperature. The current-induced intermediate phase is detected by *operando* X-ray diffraction using molten salt electrolyte at 230°C and shows the hysteretic charge/discharge characteristics. The nucleation of the intermediate phase occurs at its composition of x = 0.64–0.65 on the independent reaction direction. Both the composition of the intermediate phase and the total composition of Li_xFePO_4 does equal on the charge and does not on the discharge. This discrepancy produces the unexpected results that the sequential phase transition via the intermediate phase as a single phase proceeds on the charge, but the three phases coexist in a whole reaction on the discharge. The charge process is a kinetically favorable direction for a current-induced phase transition being responsible for the intermediate phase. This phase transition mechanism could be deduced to the actual environment. The formation of the intermediate phase is important as its further stabilization leads to an extension of a single phase reaction, realizing high-rate electrode materials.

3.1. Introduction

Phase transition mechanism within topochemical intercalation materials has been widely studied in energy devices.[1-3] For Li-ion batteries, along with Li compositional change, the phase separation occurs in the two-phase system while the lattice constant varies with the Vegard's low in the solid solution system. The phase boundary between two phases restricts the specific surface area for Li diffusion and hinders the high-rate cycling due to the activation process induced by the strain energy.[4, 5] Although the two-phase materials have the disadvantage for the high-rate characteristics, extraordinary phase transition via a new phase in addition to the original two phases has been observed[6-8] and becomes a bypass to the low energy route under the high current density. This phenomenon is far from those expected on a basis of equilibrium thermodynamics. The rate-dependent phase transition mechanism is a key to understand the fast intercalation kinetics.

$LiFePO_4$ is a model phase transition material with the two phase character that each of Li-rich (LFP) and Li-poor (FP) phase, being isostructural with olivine, is responsible for the charge transfer within the intercalation reaction processes[9]. These end-members deviate slightly from stoichiometric $LiFePO_4$ and $FePO_4$, having the solid solution range across a large miscibility gap under an equilibrium state at room temperature[10]. During high rate cycling, density functional theory[11] and electrochemical phase-field model[12] predict suppression of phase separation and possibility of a solid-solution pathway. Above a critical current density, a single phase reaction extended by the solid solution range of the end-members proceeds without phase separation that hinders the homogeneous Li diffusion. This is also confirmed by experimental results[13-16]. Meanwhile, the explanation based on the Gibbs energy[13] allows emergence of a new phase in a non-equilibrium state, and the metastable intermediate phase of Li_xFePO_4 which participates in the electrochemical reaction as the third phase has been observed[6, 17-21]. The composition of the metastable intermediate phase is x = 0.6–0.7, corresponding to that of the eutectoid point[22, 23]. More specifically, $Li_{2/3}FePO_4$ has a long-range ordering superstructure[24] and shows the extremely high electronic conductivity[25]. The metastable intermediate phase accelerates the reaction kinetics to act as a buffer layer that moderates the lattice mismatch between the two phases. Nevertheless, the quantitative analysis for the kinetics of the intermediate phase is inherent in difficulties of direct observation during electrochemical reactions at room temperature.

Here we investigated the phase transition mechanism via the intermediate phase as a thermodynamically stable phase at elevated temperature using *operando* X-ray diffraction to be deduced the deep insight at room temperature. The origin of the metastable intermediate phase is regarded as the eutectoid point at high temperature, above which the intermediate phase (L*x*FP) involves the phase transition in addition to LFP and FP as the thermodynamically stable phase. As the eutectoid temperature is 200°C based on the phase diagram[23], the measurement environment above 200°C must be prepared.

At around 100°C, LiBOB/EC electrolyte was used and provided good cyclabilitiy[26] and rate performance[27]. Above 150°C, however, EC-based electrolyte is unstable thermodynamically so that a molten salt electrolyte is necessary. A modified Swagelok cell with the two electrode system being absent from any binder allowed $LiFePO_4$ to be successfully cycled using LiTFSA as electrolyte, although the expected two-phase (LFP + FP) to one-phase (L*x*FP) transition could not be detected at 230–250°C[28].

We assembled a beaker type three electrode cell to estimate the precise electrode potential as well as to minimize the solution resistance. A binary molten salt consisted of LiTFSA and CsTFSA works as an excellent electrolyte at moderate temperature that exhibits low melting point (below 100°C)[29] and high ionic conductivity[30]. Li–Al alloy has the ability to replace lithium metal as the counter electrode and even the reference electrode, which can store and release lithium-ion without showing any significant polarization[31]. An X-ray diffractometer built-in atmosphere control glove box device enables this open operating system to apply a confocal X-ray diffraction (XRD) method to avoid the absorption from caesium, tracking the phase transition reaction.

3.2. Experimental

3.2.1. Cell preparation

$LiFePO_4$ was purchased and characterized by SEM, and XRD (**Figure 3.1**, **Figure 3.2**, and **Table 3.1**). The working electrode was a composite of 90 wt% $LiFePO_4$, 5 wt% acetylene black (Denka Company Limited), and 5 wt% polyamic acid (IST), which is a precursor of polyimide binder. The composite was cast onto Al foil current collector and heated up to 260°C in vacuum for 3 h to form polyimide from polyamic acid. The electrolyte was a binary molten salt mixture which is consisted of 20 mol% lithium

bis(trifluoromethanesulfonyl) amide (LiTFSA) and 80 mol% caesium bis(trifluoromethanesulfonyl) amide (CsTFSA). Li metal was used as the counter and reference electrodes for measurements at 170°C. Li–Al alloy was prepared by an electrochemical method that the Al wire was lithiated to 60 mol% in the molten mixture LiTFSA–CsTFSA at 160°C and used as the counter and reference electrodes for measurements at 200°C and 230°C (**Figure 3.3**).

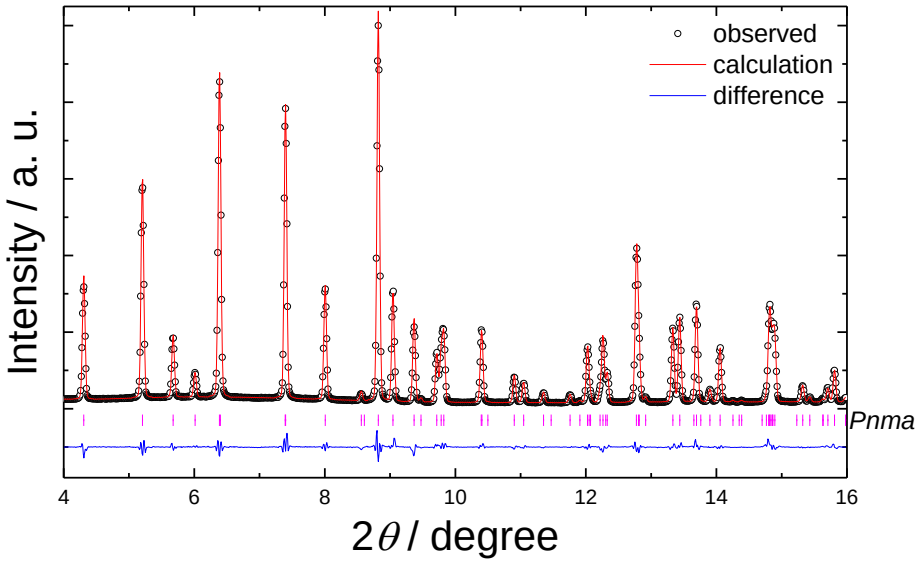

Figure 3.1. Synchrotron XRD patterns of the pristine $LiFePO_4$ powder. *The wavelength was set at 0.3875(4) Å. Space group is Pnma. The refined lattice parameters are a = 10.3480(1) Å, b = 6.0181(7) Å, c = 4.69968(6) Å, and V = 292.67(4) Å^3.*

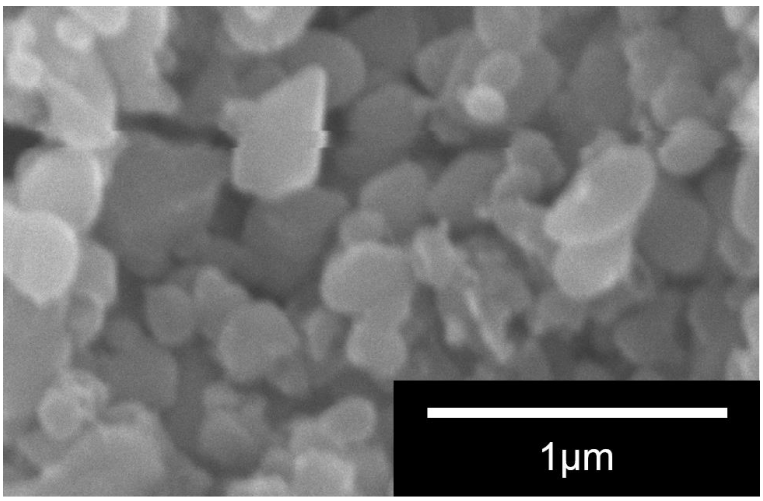

Figure 3.2. SEM image of the pristine $LiFePO_4$ powder. *The particle size is a few hundreds micro meter.*

Table 3.1. Refined crystal parameters and reliability factors in Rietveld analysis of the pristine $LiFePO_4$ powders.

Atom	Wyckoff	g	*x*	*y*	*z*	$100*U_{iso}$ / Å^2
Li	4a	1	0	0	0	3.926
Fe	4c	1	0.2820(1)	0.25	0.9738(3)	0.738
P	4c	1	0.0946(2)	0.25	0.4182(5)	1.372
O(1)	4c	1	0.0973(4)	0.25	0.7394(9)	0.305
O(2)	4c	1	0.4548(5)	0.25	0.2086(7)	0.874
O(3)	8d	1	0.1643(3)	0.0481(5)	0.2843(5)	0.358
R_{wp} = 4.54%			R_p = 3.45%			

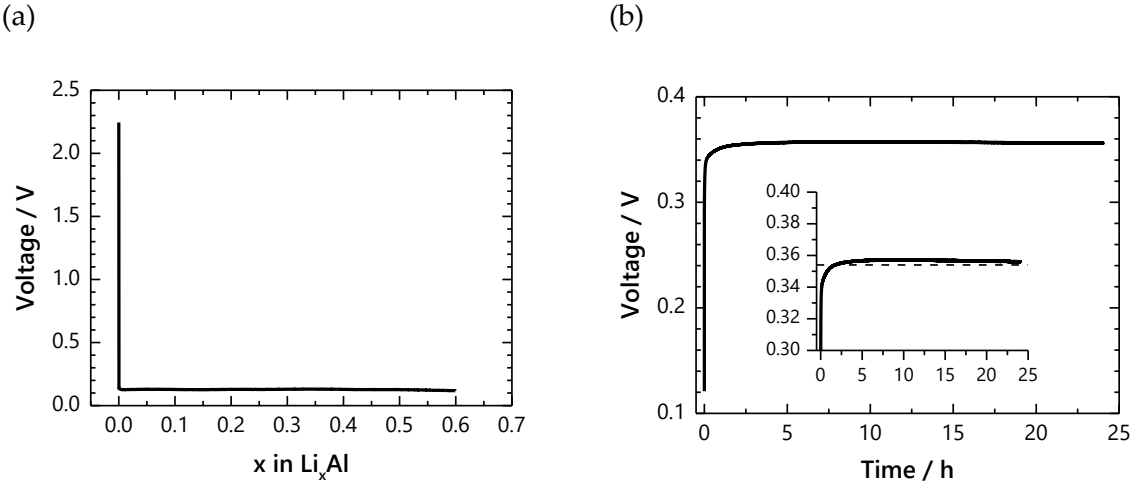

Figure 3.3. Electrochemical preparation of LiAl alloy for counter and reference electrodes. *(a) The voltage curve of lithiation into Al metal to prepare a LiAl alloy electrode within LiTFSA : CsTFSA = 20 : 80 (mol%) electrolyte at 160°C. Current density was 99.4 mA g^{-1}. (b) The voltage relaxation after the completion of LiAl alloy.*

3.2.2. Electrochemical measurements

Galvanostatic charge/discharge measurements were conducted from 1 C (= 170 mA/g) to

30 C rates at certain temperature. The cut-off potential was set on 2.8–3.8 V vs. Li^+/Li using the conversion formula.[32]

3.2.3. High-temperature *operando* XRD

Operando XRD measurements were performed a standard reflection mode geometry at a beamline BL28XU of SPring-8 (Japan). An in-vacuum tapered undulator offers quasi-monochromatic X-rays. Four Si-coated mirrors with Rh and Pt stripes allow the X-rays to be focused and very low divergence. The X-rays with the target energy were selected by a Si (111) channel-cut crystal with a narrow gap due to the high brilliance of the beam. The incident X-ray energy was set at 32.0 keV with a beam size of 0.2 mm (V) × 0.5 mm (H). The data were collected by using Ce^+-doped yttrium aluminum perovskite scintillation detector system (OKEN Co., Ltd., Japan) with an exposure time of 1.3 s for each step. A θ–2θ scan was conducted in 2θ values of between 7.2º and 7.76º by a step of 0.004°. The electrochemical cell with a temperature-controlled unit was placed in an Ar-filled glove box integrated diffractometer during measurements. The detailed setup is shown in **Figure 3.4**. The battery cell was worked under the current rate 1 C at 230°C.

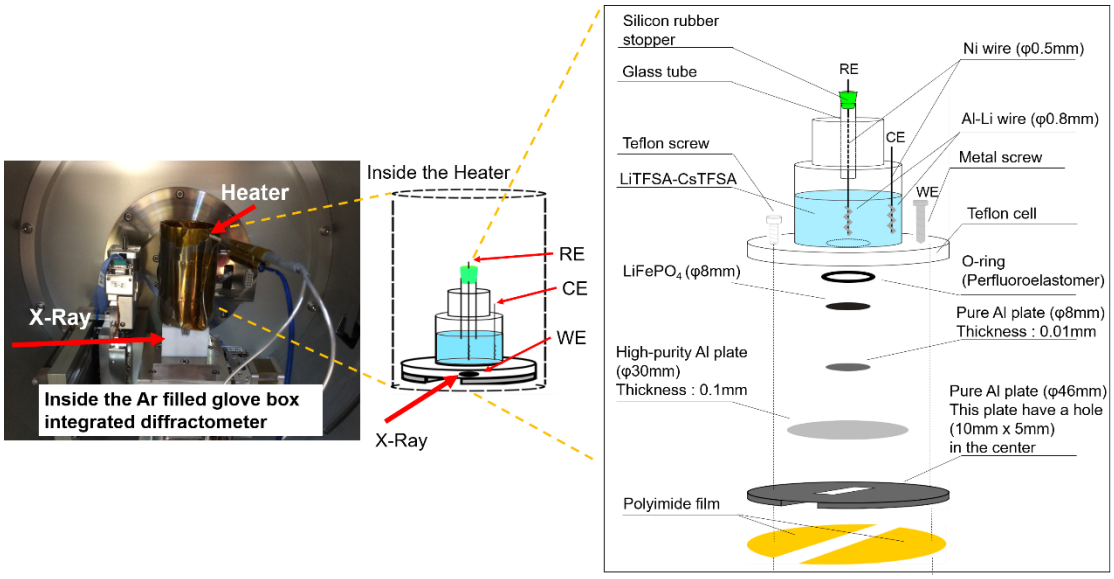

Figure 3.4. The environment of operando XRD measurement. *The electrochemical cell was put in the Ar filled glove box integrated diffractometer. X-ray goes through underneath the cell.*

3.3. Results and Discussion

Involvement of the intermediate phase with increasing temperature is shown in **Figure**

3.5. The three measurement temperatures were selected based on the phase diagram[23]: 170, 200, and 230°C correspond to below, at, and above the eutectoid temperature, respectively. For the differential capacity plots converted from the charge/discharge curves, there is a pair of a single peak for both of the cathodic/anodic reactions at 170°C. At 200 and 230°C, on the other hand, peak separation was found in either of the reaction direction. As a single peak of redox pair splits into two peaks passing through the eutectoid temperature, formation of the intermediate phase is expected of the phase diagram.[22, 23] The two distinct peaks imply two-step phase transition between LFP + L*x*FP and L*x*FP + FP. To our knowledge, this is the first time to be detected electrochemically the current-induced intermediate phase as a thermodynamically stable phase, whereas no peak splitting was observed in electrochemical intercalation of $LiFePO_4$ at 230°C.[28] Note that the molten salt electrolyte we used is electrochemically unstable in a certain extent so that the decomposition reaction is included during the cycle, resulting in an excess of the theoretical capacity.

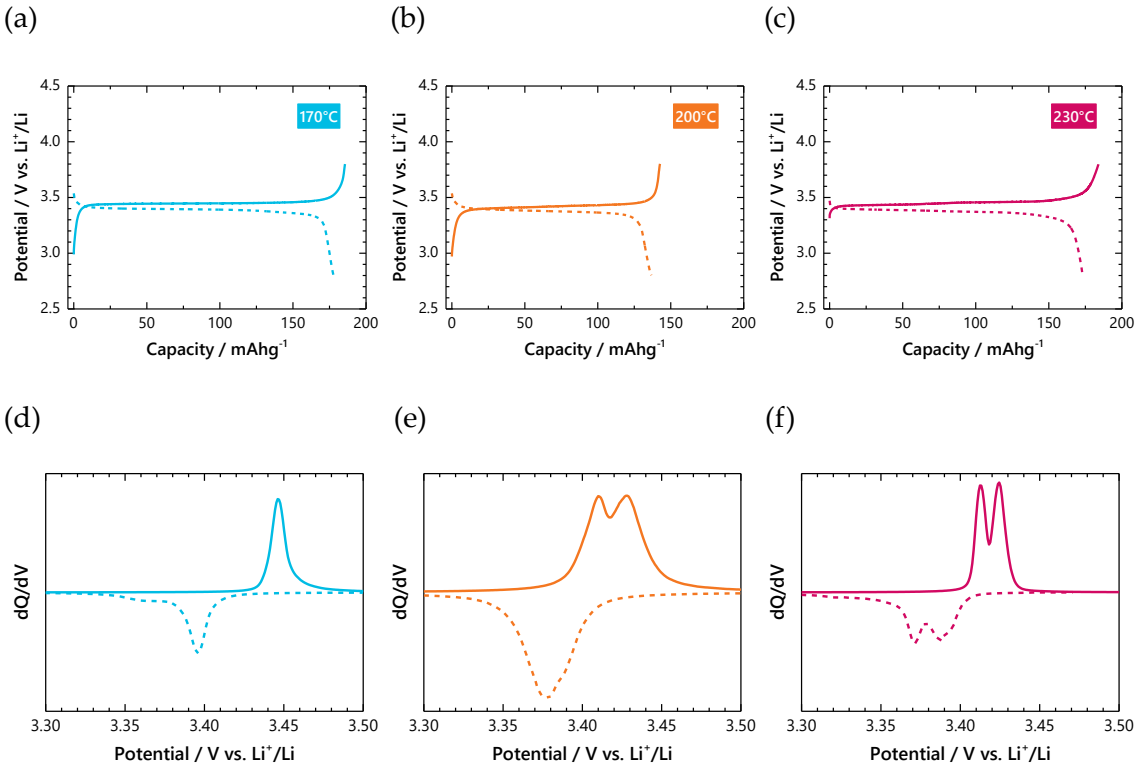

Figure 3.5. Electrochemical properties at elevated temperatures. *Galvanostatic charge/discharge curves with their differential capacity plots at (a) 170°C, (b) 200°C, and (c) 230°C. Solid lines and dashed line denote the charge/discharge process, respectively. Current density was 17.0 mAg^{-1} (1C) for all samples.*

The characteristics of the dQ/dV plots is further investigated after the normalization to each obtained capacity. The total composition of a local minimum/maximum is 55% on the charge at 200°C, and 55% on the charge and 45% on the discharge at 230°C (**Figure 3.6**). With an assumption that the fully charged/discharged state is regarded as the one lithium extraction/insertion, these compositional range is x = 0.45–0.55. The amount of the intermediate phase would maximize at the local minimum/maximum in the dQ/dV plots if the many-particle model is assumed.[33] This maximum point is different from the eutectoid point of x = 0.6 predicted by the phase diagram[23] or the value of x = 0.6–0.7 observed by high-rate cycling at room temperature.[6, 17-19]

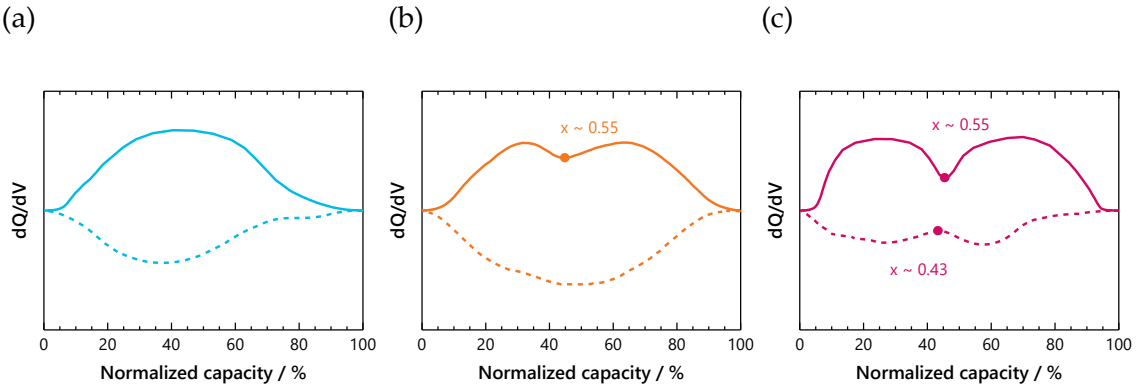

Figure 3.6. The differential capacity plots. *(a) 170°C, (b) 200°C, and (c) 230°C. Normalized capacity is calculated based on the assumption that the obtained charge/discharge capacity corresponds to the theoretical one. Current density was 17.0 mAg^{-1} (1C) for all samples.*

The hysteretic behavior is observed during the electrochemical intercalation reaction (**Figure 3.5**). At 200°C, the two separated peaks are found on the charge but not on the discharge. The two-step phase transition via the current-induced intermediate phase, as mentioned above, would be more pronounced on the charge than on the discharge. Intercalation battery materials show the inherent hysteretic behavior even at an equilibrium state.[33] Although a certain temperature should produce the same thermodynamic stability in the system, the potential profiles strongly depend on the compositional direction. The asymmetric charge/discharge behavior has been observed at the particle level that there are reaction heterogeneities during the charge but they are suppressed during the discharge,[16, 34] which is consistent with theoretical predictions.[12, 35] Moreover, the peaks on the charge are sharper than those on the discharge at 230°C. The broad potential distribution on the discharge may reflect a concurrent intercalation

pathway.[34] This result suggests the possibility of the hysteretic phase transition pathway due to the participation of the intermediate phase.

The rate-dependent dQ/dV plots converted from the galvanostatic charge/discharge curves at 230°C (**Figure 3.7**) offers the kinetic behavior of the intermediate phase. The four individual peak in **Figure 3.7b** moves toward the direction along with the applied current and each potential is plotted in **Figure 3.8**. The polarization derived from the slope on the charge is slightly smaller than that of the discharge, which is consistent with the result at room temperature.[17] The zero-current potential is almost the same in both of the charge (3.1415 V) and discharge (3.1413 V) calculated from the intersection but very slightly higher on the charge, indicating the hysteresis at an equilibrium state.[33] **Figure 3.8b** shows the produced capacity until the local minimum/maximum in dQ/dV curves on the charge/discharge. As the charge capacity located in the first peak is higher than that on the discharge, the phase transition front might be shifted more forward on the charge, leading to the continuous phase transition.

(a) (b)

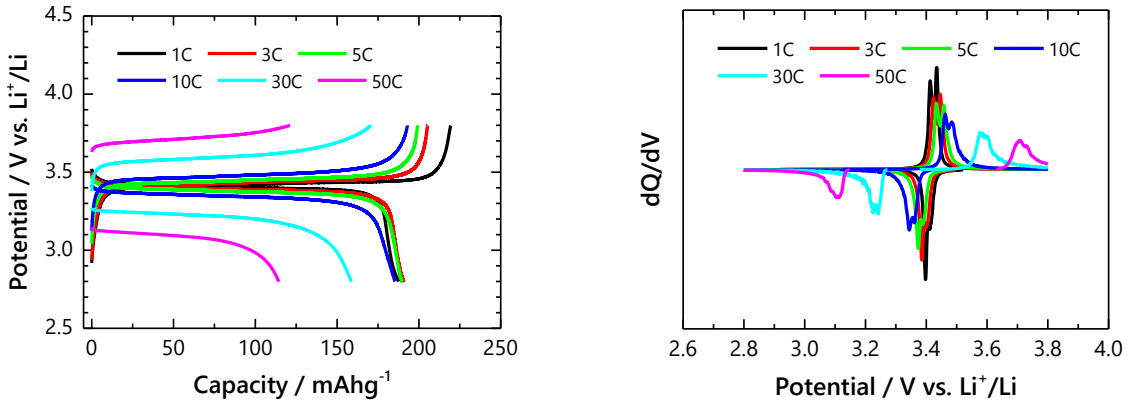

Figure 3.7. Rate dependent (a) galvanostatic charge/discharge curves with (b) their differential capacity plots at 230°C.

(a) (b)

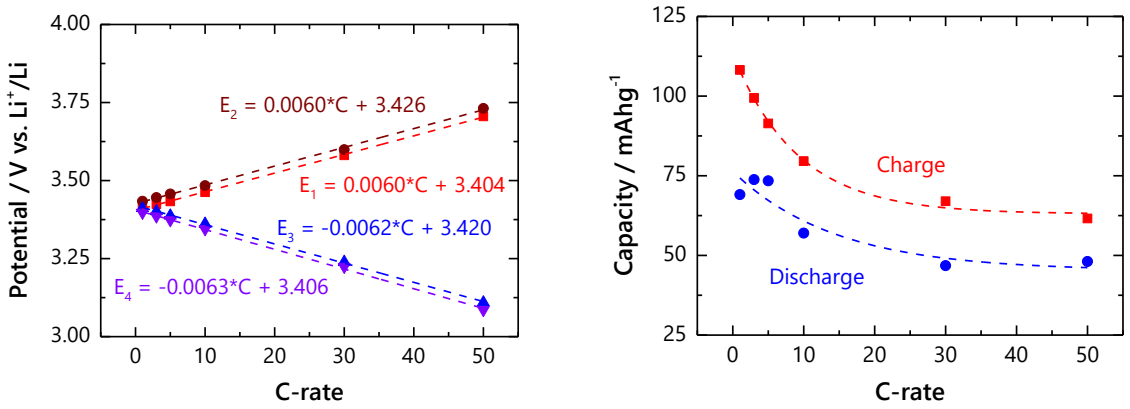

Figure 3.8. *(a) Potential plots of the local minimum/maximum in dQ/dV curves at various C-rates at 230°C. E_1 and E_2 denote the lower and the higher potential on the charge, respectively. E_3 and E_4 denote the higher and the lower potential on the discharge, respectively. Dashed lines are linear fits of each potential as a function of C-rate. The slope and the intersection represent the polarization and the potential at the equilibrium, respectively. (b) Capacity plots of the local minimum/maximum in dQ/dV curves on the charge/discharge, respectively, at various C-rates at 230°C. Dashed lines are a guide to the eye.*

To understand the crystal structure change via the intermediate phase, *operando* XRD measurement was performed at 230°C as shown in **Figure 3.9**. At this temperature, the intermediate phase is thermodynamically stable[22, 23]. The intermediate phase is observed on both of the charge/discharge as a crystalline phase and its behavior is completely different between the charge/discharge. With an assumption that Vegard's law can be applied in the three phases including the intermediate phase, their Li composition is determined as shown in **Figure 3.10**. On the charge, the stepwise phase transition proceeds along with the large compositional change of the intermediate phase from x = 0.64 to x = 0.47, whereas on the discharge, the three phase coexistence reaction occurs in a wide range, as the compositional change of the intermediate phase is restricted in x = 0.65 – 0.74. It is a noteworthy fact that the nucleation initially occurs in the reaction and the composition of the nucleus is almost the same as x = 0.66. $Li_{2/3}FePO_4$ is found in its superstructure[24] and is similar to the composition of the eutectoid point[23] and of the phase boundary[19, 36]. The amount of the intermediate phase, however, might maximize at the total composition of x = 0.45 – 0.55 and is more on the charge, as shown in **Figure 3.11**. Considering the coherency strain model[37], the composition in which the Gibbs free energy in coherent two-phase coexistence maximizes is x ~ 0.4, lower than that in which the Gibbs free energy in a homogeneous phase locally minimizes. This is not inconsistent with the nucleation and growth model[38]. This compositional discrepancy originates the

hysteretic behavior between the sequential phase transition on the charge and the coexistence of three phases on the discharge.

(a) (b)

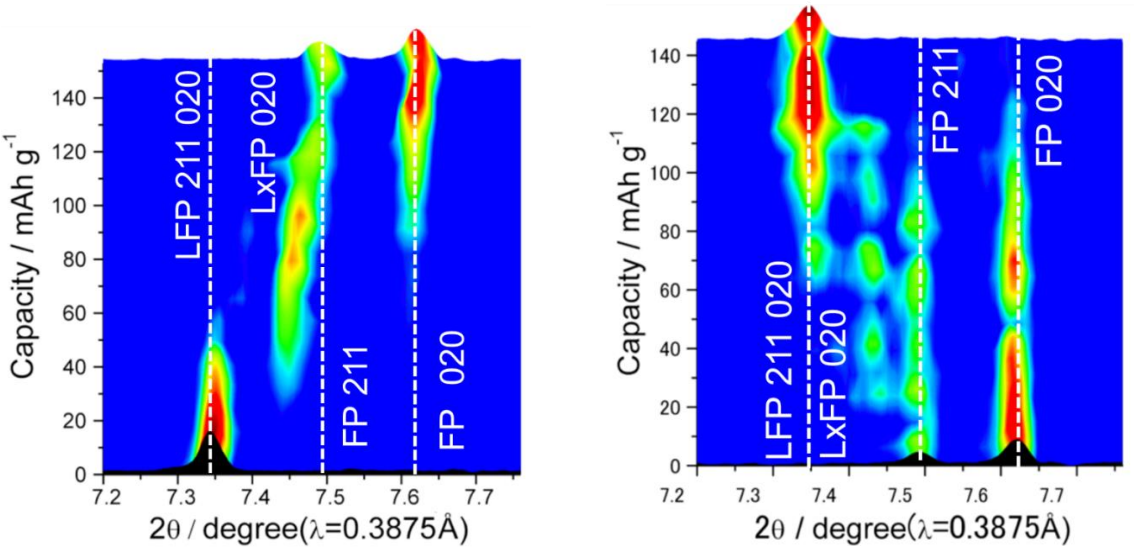

Figure 3.9. *operando XRD patterns during (a) the charge and (b) discharge at 230°C. The intensity indicates in color scale that the red is high and blue is low. Dashed lines are a guide for each phase position.*

(a) (b)

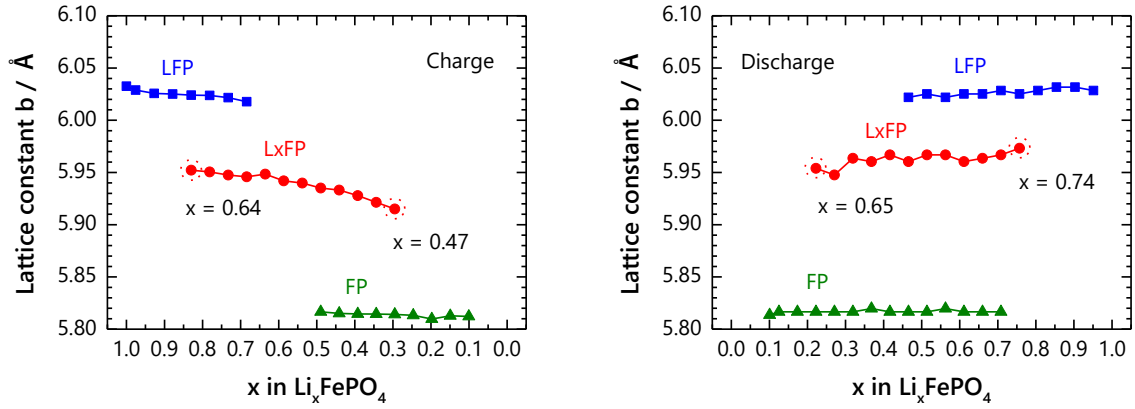

Figure 3.10. *The lattice parameters of LFP, LxFP, and FP obtained from peak centers of partial diffraction profiles during (a) charge and (b) discharge at 230°C.*

(a) (b)

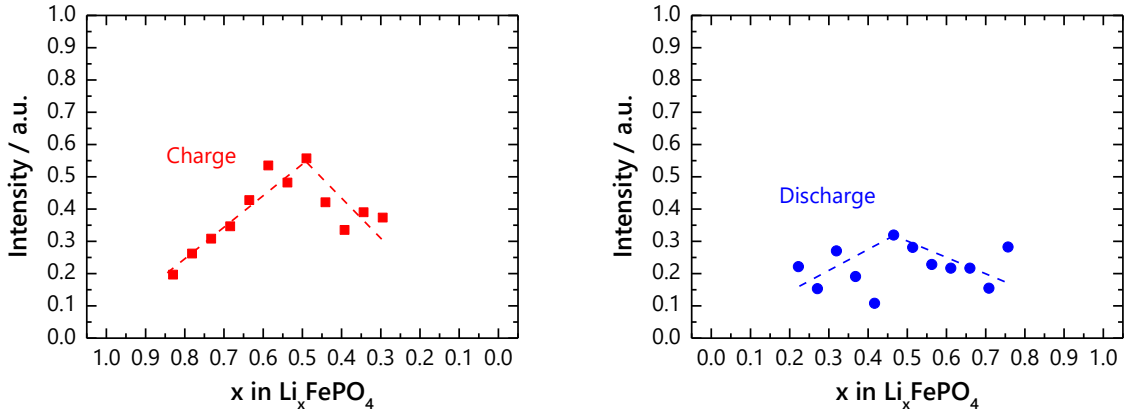

Figure 3.11. *The intensity of the intermediate solid solution phase during (a) charge and (b) discharge at 230°C.*

Figure 3.12 illustrates the hysteretic phase transition in Li_xFePO_4. On the charge, as the intermediate phase whose composition is x = 0.64 emerges, its amount increases toward the total composition of x = 0.5. The intermediate phase takes great responsible for the phase transition reaction with the contact of these composition. Once the single phase forms in the system, the high speed phase transition route can be accessible. The lattice mismatch is shrinking through the reaction. The nucleation composition on the discharge is equal to that on the charge and the growth reaction evolves. However, the composition of the intermediate phase is far away from the total composition, which hinders the sequential phase transition as seen on the charge. Consequentlu, FP remains to the end of the reaction, which generates the larger lattice strain than that on the charge at the phase boundary.

(a)

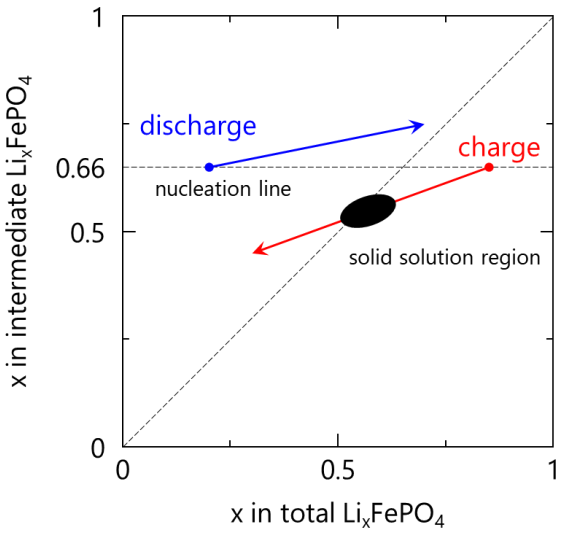

(b)

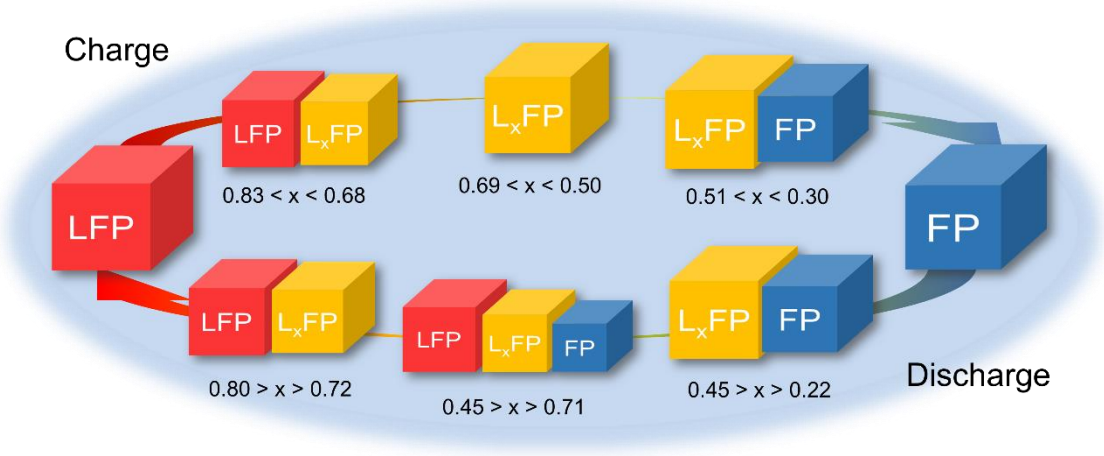

Figure 3.12. Phase transition model within the stable solid solution phase. *(a) X-axis is the total composition of Li_xFePO_4 and y-axis is the composition of the intermediate phase of Li_xFePO_4. On the charge, these two have the same value, resulting in the solid solution reaction. On the discharge, however, they are different, resulting in the phase separation.*

Our findings about the intermediate phase help with creating the high-power electrode materials. The metastable intermediate phase at room temperature freezes on the discharge[17], which is explained as mentioned above. The electrode material whose intermediate phase is stabilized in the wide Li compositional range should exhibit the

high rate performance. Indeed, the rate characteristics on the charge is superior to that on the discharge (**Figure 3.13**), restricting the practical capacity by the discharge one. The improvement of the rate-determining discharge process has the potential to be the faster phase transition kinetics.

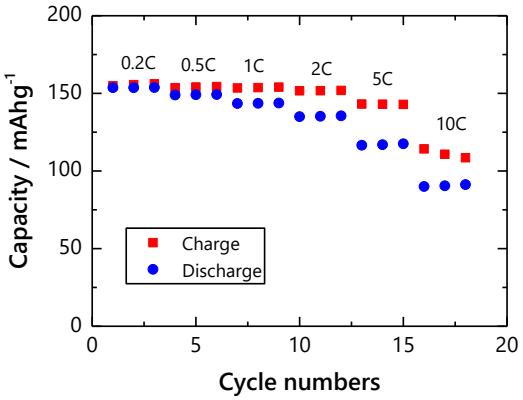

Figure 3.13. Rate capability of charge or discharge separately at room temperature. *The charge profiles are obtained under the fixed discharge rate of 0.2C and the discharge ones are obtained under the fixed charge rate of 0.2C.*

3.4. Conclusion

We investigated the intermediate phase of $LiFePO_4$ as a function of temperature where the intermediate phase exists as a thermodynamically stable phase to understand the phase transition mechanism, which has not been clarified at room temperature. The intermediate phase as a thermodynamically stable phase is detected electrochemically at 230°C for the first time. The *operando* XRD was conducted to track the crystal structure change using an X-ray diffractometer built-in atmosphere control glove box device. On the charge, the intermediate phase emerges at the compositional range of x = 0.64-0.47, the reaction proceeding sequentially like LFP -> LFP + LxFP -> LxFP -> LxFP + FP -> FP. On the discharge, the intermediate phase emerges at the compositional range of x = 0.64–0.47, the reaction proceeding to keep with the three phase coexistence. The nucleation occurs at x = 0.64–65 on both of the direction, and the amount of the intermediate phase maximizes at the total composition of x = 0.49 on the charge and x = 0.46 on the discharge. The composition of x = 0.6–0.7 is consistent with that of the eutectoid point in which the intermediate phase exists most stable thermodynamically. The two phase coexistence is most unstable at the composition of x = 0.4–0.5. Combining the prediction from the rate-

dependent galvanostatic tests, the charge process is the kinetically favorable direction. Indeed, the rate performance test evaluating the charge/discharge individually shows that the charge is faster than the discharge at room temperature. The involvement of the intermediate phase originates the current-induced hysteretic behavior, elucidating that the capacity of $LiFePO_4$ is limited to the discharge process. $LiFePO_4$ has the potential to enhance the rate capability furthermore by the approach that the intermediate phase is stabilized the wider compositional range.

References

1. Arico, A. S.; Bruce, P.; Scrosati, B.; Tarascon, J. M.; Van Schalkwijk, W., Nanostructured Materials for Advanced Energy Conversion and Storage Devices. *Nat. Mater.* **2005,** *4* (5), 366-377.

2. Dunn, B.; Kamath, H.; Tarascon, J. M., Electrical Energy Storage for the Grid: A Battery of Choices. *Science* **2011,** *334* (6058), 928-935.

3. Mohtadi, R.; Orimo, S. I., The renaissance of hydrides as energy materials. *Nat Rev Mater* **2017,** *2* (3).

4. Maxisch, T.; Ceder, G., Elastic properties of olivine LixFePO4 from first principles. *Phys. Rev. B* **2006,** *73* (17).

5. Lv, W. Q.; Niu, Y. H.; Jian, X.; Zhang, K. H. L.; Wang, W.; Zhao, J. Y.; Wang, Z. M.; Yang, W. Q.; He, W. D., Space matters: Li+ conduction versus strain effect at FePO4/LiFePO4 interface. *Appl. Phys. Lett.* **2016,** *108* (8).

6. Orikasa, Y.; Maeda, T.; Koyama, Y.; Murayama, H.; Fukuda, K.; Tanida, H.; Arai, H.; Matsubara, E.; Uchimoto, Y.; Ogumi, Z., Direct Observation of a Metastable Crystal Phase of Li_xFePO_4 under Electrochemical Phase Transition. *J. Am. Chem. Soc.* **2013,** *135* (15), 5497-5500.

7. Komatsu, H.; Arai, H.; Koyama, Y.; Sato, K.; Kato, T.; Yoshida, R.; Murayama, H.; Takahashi, I.; Orikasa, Y.; Fukuda, K.; Hirayama, T.; Ikuhara, Y.; Ukyo, Y.; Uchimoto, Y.; Ogumi, Z., Solid Solution Domains at Phase Transition Front of $Li_xNi_{0.5}Mn_{1.5}O_4$. *Adv Energy Mater* **2015,** *5* (17).

8. Zhou, Y. N.; Yue, J. L.; Hu, E. Y.; Li, H.; Gu, L.; Nam, K. W.; Bak, S. M.; Yu, X. Q.; Liu, J.; Bai, J. M.; Dooryhee, E.; Fu, Z. W.; Yang, X. Q., High-Rate Charging Induced Intermediate Phases and Structural Changes of Layer-Structured Cathode for Lithium-Ion Batteries. *Adv Energy Mater* **2016,** *6* (21).

9. Padhi, A. K.; Nanjundaswamy, K. S.; Goodenough, J. B., Phospho-Olivines as Positive-Electrode Materials for Rechargeable Lithium Batteries. *J. Electrochem. Soc.* **1997,** *144* (4), 1188-1194.

10. Yamada, A.; Koizumi, H.; Nishimura, S. I.; Sonoyama, N.; Kanno, R.; Yonemura, M.; Nakamura, T.; Kobayashi, Y., Room-Temperature Miscibility Gap in Li_xFePO_4. *Nat. Mater.* **2006,** *5* (5), 357-360.

11. Malik, R.; Zhou, F.; Ceder, G., Kinetics of Non-Equilibrium Lithium Incorporation in

$LiFePO_4$. *Nat. Mater.* **2011,** *10* (8), 587-590.

12. Bai, P.; Cogswell, D. A.; Bazant, M. Z., Suppression of Phase Separation in $LiFePO_4$ Nanoparticles during Battery Discharge. *Nano Lett.* **2011,** *11* (11), 4890-4896.

13. Zhang, X. Y.; van Hulzen, M.; Singh, D. P.; Brownrigg, A.; Wright, J. P.; van Dijk, N. H.; Wagemaker, M., Rate-Induced Solubility and Suppression of the First-Order Phase Transition in Olivine $LiFePO_4$. *Nano Lett.* **2014,** *14* (5), 2279-2285.

14. Liu, H.; Strobridge, F. C.; Borkiewicz, O. J.; Wiaderek, K. M.; Chapman, K. W.; Chupas, P. J.; Grey, C. P., Capturing Metastable Structures during High-Rate Cycling of $LiFePO_4$ Nanoparticle Electrodes. *Science* **2014,** *344* (6191).

15. Zhang, X. Y.; van Hulzen, M.; Singh, D. P.; Brownrigg, A.; Wright, J. P.; van Dijk, N. H.; Wagemaker, M., Direct View on the Phase Evolution in Individual $LiFePO_4$ Nanoparticles during Li-Ion Battery Cycling. *Nat. Commun.* **2015,** *6*.

16. Lim, J.; Li, Y. Y.; Alsem, D. H.; So, H.; Lee, S. C.; Bai, P.; Cogswell, D. A.; Liu, X. Z.; Jin, N.; Yu, Y. S.; Salmon, N. J.; Shapiro, D. A.; Bazant, M. Z.; Tyliszczak, T.; Chueh, W. C., Origin and Hysteresis of Lithium Compositional Spatiodynamics within Battery Primary Particles. *Science* **2016,** *353* (6299), 566-571.

17. Hess, M.; Sasaki, T.; Villevieille, C.; Novak, P., Combined *Operando* X-ray Diffraction-Electrochemical Impedance Spectroscopy Detecting Solid Solution Reactions of $LifFePO_4$ in Batteries. *Nat. Commun.* **2015,** *6*.

18. Koyama, Y.; Uyama, T.; Orikasa, Y.; Naka, T.; Komatsu, H.; Shimoda, K.; Murayama, H.; Fukuda, K.; Arai, H.; Matsubara, E.; Uchimoto, Y.; Ogumi, Z., Hidden Two-Step Phase Transition and Competing Reaction Pathways in $LiFePO_4$. *Chem. Mater.* **2017,** *29* (7), 2855-2863.

19. Kobayashi, S.; Kuwabara, A.; Fisher, C. A. J.; Ukyo, Y.; Ikuhara, Y., Microscopic Mechanism of Biphasic Interface Relaxation in Lithium Iron Phosphate after Delithiation. *Nat. Commun.* **2018,** *9*.

20. Li, Y. Y.; Chen, H. R.; Lim, K.; Deng, H. D.; Lim, J.; Fraggedakis, D.; Attia, P. M.; Lee, S. C.; Jin, N.; Moskon, J.; Guan, Z. X.; Gent, W. E.; Hong, J.; Yu, Y. S.; Gaberscek, M.; Islam, M. S.; Bazant, M. Z.; Chueh, W. C., Fluid-Enhanced Surface Diffusion Controls Intraparticle Phase Transformations. *Nat. Mater.* **2018,** *17* (10), 915-923.

21. Yoshinari, T.; Yamamoto, K.; Nishijima, M.; Fukuda, K.; Kuwabara, A.; Tanaka, I.; Maeda, K.; Kageyama, H.; Orikasa, Y.; Uchimoto, Y., High Rate Performance of Dual-Substituted $LiFePO_4$ Based on Controlling Metastable Intermediate Phase. *ACS Appl. Energy Mater.* **2018,** *1* (12), 6736-6740.

22. Delacourt, C.; Poizot, P.; Tarascon, J. M.; Masquelier, C., The Existence of a Temperature-Driven Solid Solution in Li_xFePO_4 for $0 <= x <= 1$. *Nat. Mater.* **2005,** *4* (3), 254-260.

23. Dodd, J. L.; Yazami, R.; Fultz, B., Phase Diagram of Li_xFePO_4. *Electrochem. Solid-State Lett.* **2006,** *9* (3), A151-A155.

24. Nishimura, S.; Natsui, R.; Yamada, A., Superstructure in the Metastable Intermediate-Phase $Li_{2/3}FePO_4$ Accelerating the Lithium Battery Cathode Reaction. *Angew. Chem. Int. Ed.* **2015,** *54* (31), 8939-8942.

25. Lu, J. C.; Oyama, G.; Nishimura, S.; Yamada, A., Increased Conductivity in the Metastable Intermediate in Li_xFePO_4 Electrode. *Chem. Mater.* **2016,** *28* (4), 1101-1106.

26. Mestre-Aizpurua, F.; Hamelet, S.; Masquelier, C.; Palacin, M. R., High Temperature Electrochemical Performance of Nanosized $LiFePO_4$. *J. Power Sources* **2010,** *195* (19), 6897-6901.

27. Kurita, T.; Lu, J. C.; Yaegashi, M.; Yamada, Y.; Nishimura, S.; Tanaka, T.; Uzumaki, T.; Yamada, A., Challenges toward Higher Temperature Operation of $LiFePO_4$. *J. Power Sources* **2012,** *214*, 166-170.

28. Munoz-Rojas, D.; Leriche, J. B.; Delacourt, C.; Poizot, P.; Palacin, M. R.; Tarascon, J. M., Development and Implementation of a High Temperature Electrochemical Cell for Lithium Batteries. *Electrochem. Commun.* **2007,** *9* (4), 708-712.

29. Hagiwara, R.; Tamaki, K.; Kubota, K.; Goto, T.; Nohira, T., Thermal Properties of Mixed Alkali Bis(trifluoromethylsulfonyl)amides. *J. Chem. Eng. Data* **2008,** *53* (2), 355-358.

30. Kubota, K.; Tamaki, K.; Nohira, T.; Goto, T.; Hagiwara, R., Electrochemical Properties of Alkali Bis(trifluoromethylsulfonyl)amides and Their Eutectic Mixtures. *Electrochim. Acta* **2010,** *55* (3), 1113-1119.

31. Yao, N. P.; Heredy, L. A.; Saunders, R. C., Emf Measurements of Electrochemically Prepared Lithium-Aluminum Alloy. *J. Electrochem. Soc.* **1971,** *118* (7), 1039-&.

32. Amezawa, K.; Yamamoto, N.; Tomii, Y.; Ito, Y., Thermodynamic Properties and Single-Electrode Peltier Heats of a Li-Al alloy in a LiCl-KCl Eutectic Melt. *J. Electrochem. Soc.* **1999,** *146* (3), 1069-1074.

33. Dreyer, W.; Jamnik, J.; Guhlke, C.; Huth, R.; Moskon, J.; Gaberscek, M., The Thermodynamic Origin of Hysteresis in Insertion Batteries. *Nat. Mater.* **2010,** *9* (5), 448-453.

34. Li, Y. Y.; El Gabaly, F.; Ferguson, T. R.; Smith, R. B.; Bartelt, N. C.; Sugar, J. D.; Fenton, K. R.; Cogswell, D. A.; Kilcoyne, A. L. D.; Tyliszczak, T.; Bazant, M. Z.; Chueh, W. C., Current-Induced Transition from Particle-by-Particle to Concurrent Intercalation in Phase-Separating Battery Electrodes. *Nat. Mater.* **2014,** *13* (12), 1149-1156.

35. Cogswell, D. A.; Bazant, M. Z., Coherency Strain and the Kinetics of Phase Separation in $LiFePO_4$ Nanoparticles. *ACS Nano* **2012,** *6* (3), 2215-2225.

36. Nakamura, A.; Furutsuki, S.; Nishimura, S.; Tohei, T.; Sato, Y.; Shibata, N.; Yamada, A.; Ikuhara, Y., Phase Boundary Structure of Li_xFePO_4 Cathode Material Revealed by Atomic-Resolution Scanning Transmission Electron Microscopy. *Chem. Mater.* **2014,** *26* (21), 6178-6184.

37. Van der Ven, A.; Garikipati, K.; Kim, S.; Wagemaker, M., The Role of Coherency Strains on Phase Stability in Li_xFePO_4: Needle Crystallites Minimize Coherency Strain and Overpotential. *J. Electrochem. Soc.* **2009,** *156* (11), A949-A957.

38. Delmas, C.; Maccario, M.; Croguennec, L.; Le Cras, F.; Weill, F., Lithium Deintercalation in $LiFePO_4$ Nanoparticles via a Domino-Cascade Model. *Nat. Mater.* **2008,** *7* (8), 665-671.

Chapter 4.
Stabilization of Intermediate Phase in $LiFePO_4$ for High-power Li-ion batteries

Fast battery charge/discharge properties strongly depend on the phase transition kinetics. The two-phase material of $LiFePO_4$ exhibits an excellent rate performance due to the participation of the metastable intermediate phase as a third phase, although the large lattice volume change between two phases exist. $Li(Fe_{0.95}Zr_{0.05})(P_{0.9}Si_{0.1})O_4$, which is dual-substituted $LiFePO_4$ with zirconium and silicon to reduce the lattice mismatch, have shown the high-rate performance as well as the long-cycle life. In this study, we investigated the characteristics of the intermediate phase in $Li(Fe_{0.95}Zr_{0.05})(P_{0.9}Si_{0.1})O_4$ at room and elevated temperature. *Operando* X-ray diffraction at room temperature reveals the metastable intermediate phase is responsible for the long range of Li composition as well as the wide solid solution by the dual-substitution. The thermal properties of the intermediate phase were evaluated at elevated temperature. The intermediate phase, whose composition corresponds to the eutectoid point, is thermodynamically stable by 30°C, which is roughly corresponding to 300 J/mol, in $Li(Fe_{0.95}Zr_{0.05})(P_{0.9}Si_{0.1})O_4$. The stabilized intermediate phase is easily accessed during the fast charge/discharge and the bypass for the accelerated phase transition route. The stabilization of the intermediate phase kinetically as well as thermodynamically is a key to enhance the rate capability and provides the new approach for material exploration.

4.1. Introduction

$LiFePO_4$ has overcome its low electronic/ionic conductivity, being commercialized and the major cathode material. The electrochemical performance of $LiFePO_4$ have been improved especially by the carbon-coating[1] and the nano-sizing[2]. The reduction of the particle size increases the surface area and shortens the diffusion distance as well as changes the thermodynamic property[3-6]. Li_xFePO_4 decomposes into the end members of Li-rich phase (LFP) and Li-poor phase (FP) with some extent of the solid solution range at an equilibrium[7]. The large miscibility gap characterizes $LiFePO_4$ as the two-phase material. Although the intercalation reaction proceeds via the two-phase reaction at low rates, the metastable intermediate phase participates in the electrochemical reaction as a new phase with high current density. The composition of the metastable intermediate phase is x = 0.61-0.66, corresponding to that of the eutectoid point[8].

The substitution at the Li site enhances the rate performance at high rates with diminishing the voltage plateau, although it significantly decreases the reversible capacity at low rates[9, 10]. The substitution at the Fe site is also considered[11-15], but the rate performance is at most comparable to that of un-substituted material. Recent research has reported that $Li(Fe_{0.95}Zr_{0.05})(P_{0.9}Si_{0.1})O_4$, which is dual-substituted $LiFePO_4$ with zirconium and silicon to reduce the lattice mismatch, shows the excellent cycle life[16] as well as the high rate performance[17]. The metastable intermediate phase plays an important role for the continuous phase transition that the slow two-phase kinetics leads to the fast single-phase reaction with moderation of the phase boundary strain. Here we investigated the further phase transition mechanism of the intermediate phase in $Li(Fe_{0.95}Zr_{0.05})(P_{0.9}Si_{0.1})O_4$ at room and elevated temperature.

4.2. Experimental

Both $LiFePO_4$ and $Li(Fe_{0.95}Zr_{0.05})(P_{0.9}Si_{0.1})O_4$ were synthesized in the same manner as reported[17]. The cathode materials for the electrochemical tests at room temperature were prepared by mixing 80% active material, 10% carbon black (Denka), and 10% polyvinylidene fluoride (PVDF) (Kureha) with 1-methyl-2-pyrrolidinone solvent (Wako). The composite electrodes were placed in laminate-typed cells in an Ar-filled glovebox with lithium metal as the counter electrodes. $LiPF_6$ (1 M) in a 3:7 volume ratio of ethylene carbonate (EC) and ethyl methyl carbonate (EMC) (Kishida) was used as the electrolyte.

Time-resolved XRD measurements were performed at SPring-8 with a wavelength of 0.619862(2) Å using a 1D detector, MYTHEN 1K. The data were collected in the 2θ range of 10° to 13° with an exposure time of 1 s every 60 s (1C) and 15 s (10C).

The temperature-controlled XRD under Ar atmosphere was performed at the range from 25°C to 300°C with the Li concentration of x=0.66. The collection of the 2theta range is from 29.0° to 31.5° with CuKa radiation.

The cathode materials for the electrochemical tests at high temperature were prepared by mixing 80% active material, 10% carbon black, and 10% polyimmide binder with n-methyl pyrrolidione. A binary molten salt electrolyte based on $M(SO_2CF_3)_2$ (M = Li, Cs) was used as the electrolyte. The galvanostatic charge-discharge was performed between 150°C and 170°C.

4.3. Results and Discussion

Rate-dependent phase transition reactions are shown in **Figure 4.1** and **Figure 4.2**. At a low rate of 1C, the typical two phase reaction occurs in $LiFePO_4$ (**Figure 4.1a**). The phase transition during the charge/discharge is almost symmetric and the lattice constant is independent of Li concentration. The reaction in $Li(Fe_{0.95}Zr_{0.05})(P_{0.9}Si_{0.1})O_4$ shows a bit difference from the undoped one. The lattice constant of LFP on the discharge when LFP evolves as a new phase quite shifts toward FP and the range of the two phase coexistence is shortened. Nevertheless, this characteristic is not influential for the rate capability at lower rates of 1C.[17] The charge/discharge processes for $Li(Fe_{0.95}Zr_{0.05})(P_{0.9}Si_{0.1})O_4$ classifies two phase reaction in the same as $LiFePO_4$. In contrast, the reaction for the $LiMn_yFe_{1-y}PO_4$ system includes the intermediate phase despite a low rate of 0.1C.[15, 18]

At a high rate of 10C, the phase transition mechanism in both cathodes depends on the involvement of the metastable intermediate phase. The metastable intermediate phase whose composition is x = 0.61-0.66 evolves as a third phase under high rate cycling, as reported by Orikasa *et al*.[19] The third phase appears at high temperature[8, 20, 21] and even at low temperature.[22] Thus, we analyze the obtained XRD patterns with the three phases. To determine the composition, Vegard's law is applied as an assumption. In $LiFePO_4$, LxFP emerges at the end of the discharge after the 1st cycle and the beginning of the charge after the 2nd cycle and its lattice constant changes in the composition of x = 0.68 - 0.77. This is unexpectedly the first result how the third phase of LxFP alters its Li

concentration.

The phase transition for $Li(Fe_{0.95}Zr_{0.05})(P_{0.9}Si_{0.1})O_4$ continuously proceeds via the metastable intermediate phase that takes great responsible for the electrochemical reaction. LxFP emerges from the beginning of the 1st charge and its lattice constant changes in the composition of x = 0.63 – 0.86. The metastable intermediate phase with the wider compositional range produces the consecutive phase transition to relax the large volume change between LFP and FP. This suggests that $Li(Fe_{0.95}Zr_{0.05})(P_{0.9}Si_{0.1})O_4$ shows the higher rate capability than that of $LiFePO_4$ to realize the fast phase transition that LxFP acts extensively as a buffer layer to reduce the lattice strain. The different behavior of the metastable intermediate phase for both cathodes explains the rate performance under high rates. The composition of the metastable intermediate phase leans on LFP rather than on FP, which may result from the formation of the intermediate solid solution phase that appears lower temperature on high Li concentration.[8, 20] This distribution is good agreement with the electrochemical phase-field model.[23]

(a)

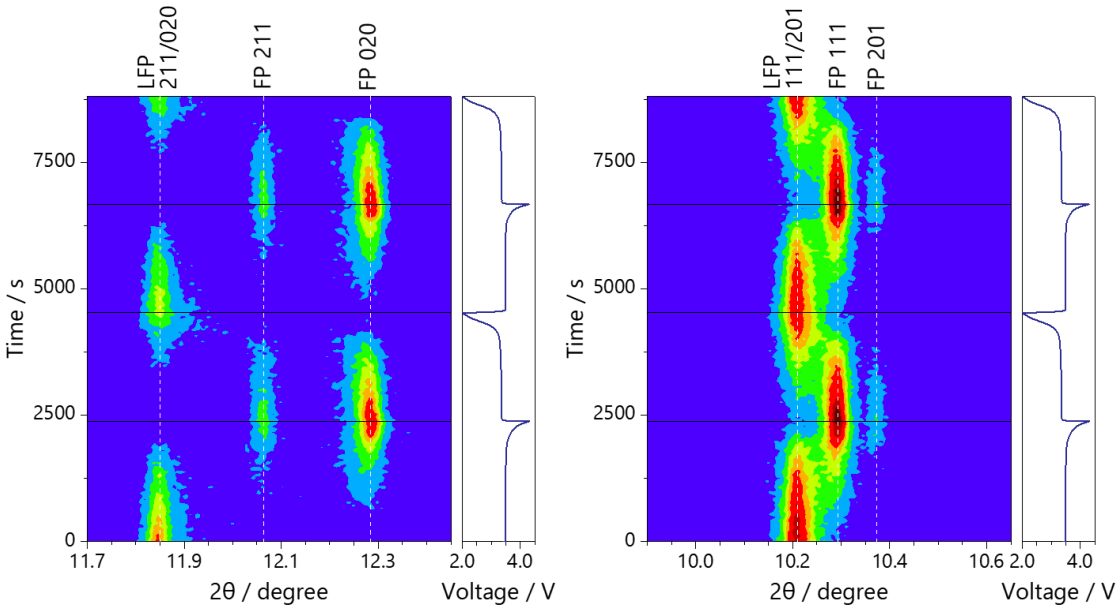

(b)

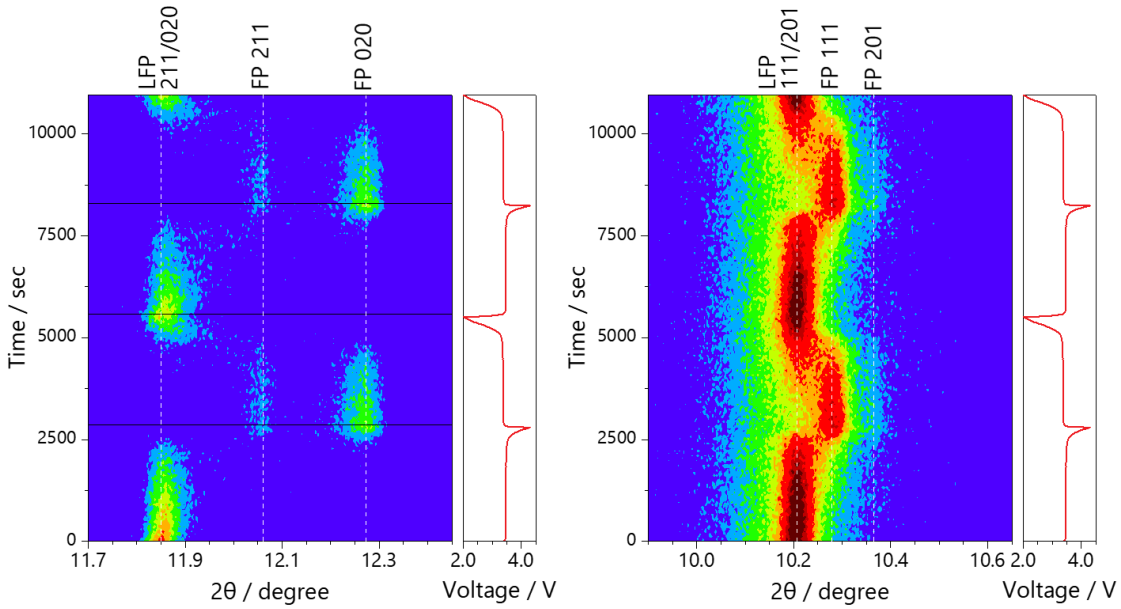
LFP 211/020
FP 211
FP 020
LFP 111/201
FP 111
FP 201
Time / sec
2θ / degree
Voltage / V

(c)

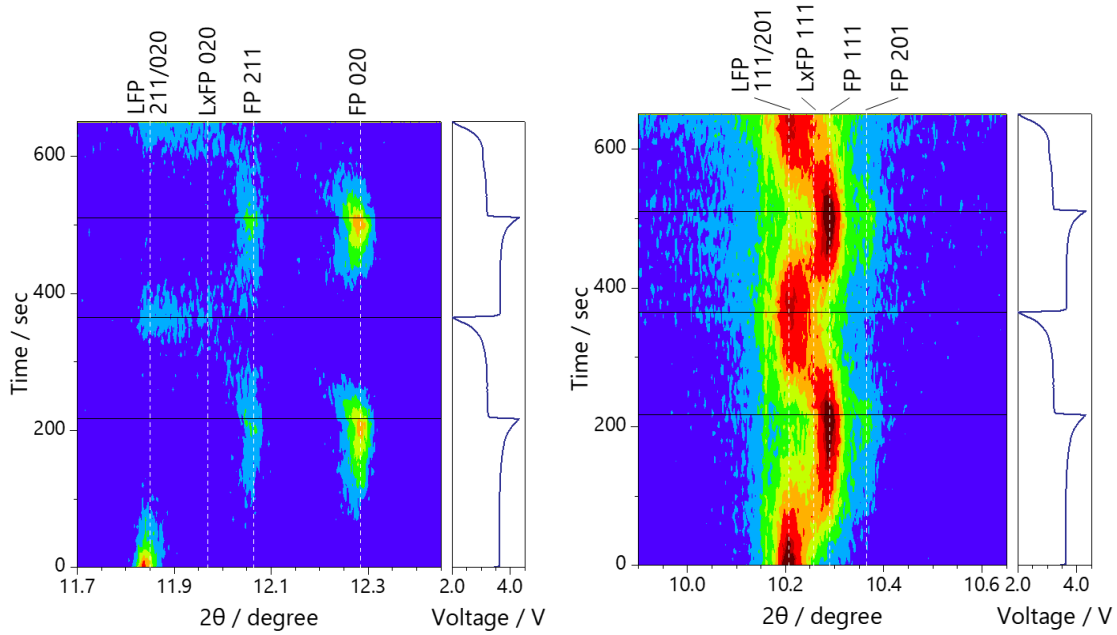
LFP 211/020
LxFP 020
FP 211
FP 020
LFP 111/201
LxFP 111
FP 111
FP 201
Time / sec
2θ / degree
Voltage / V

(d)

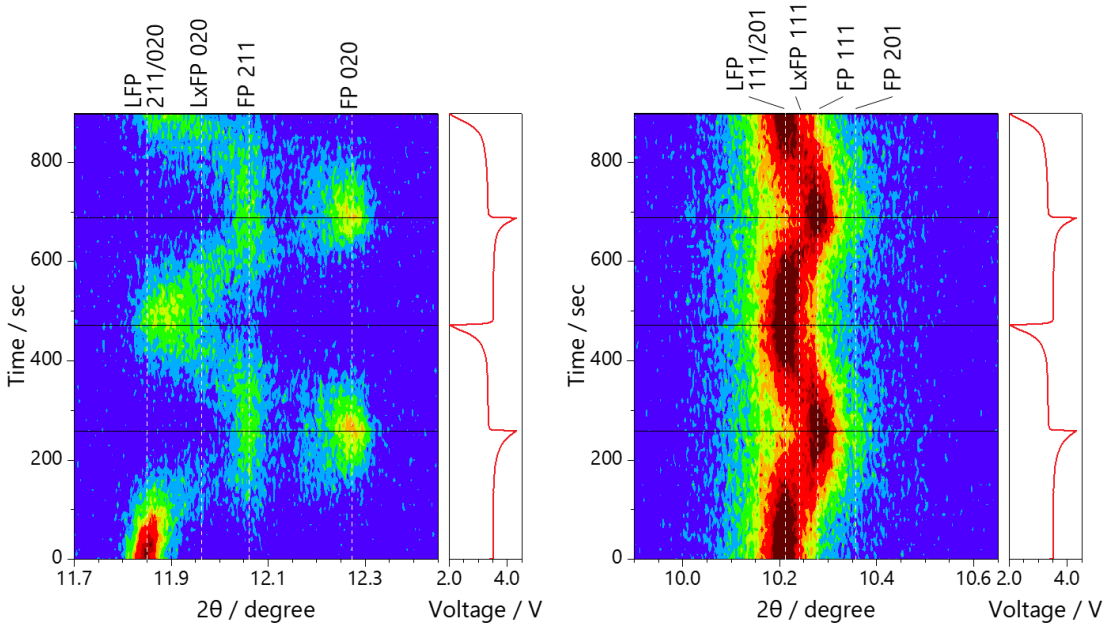

Figure 4.1. Time-resolved XRD patterns during charge/discharge cycling. *(a) $LiFePO_4$ and (b) $Li(Fe_{0.95}Zr_{0.05})(P_{0.9}Si_{0.1})O_4$ at a low rate of 1C and (c) $LiFePO_4$ and (d) $Li(Fe_{0.95}Zr_{0.05})(P_{0.9}Si_{0.1})O_4$ at a high rate of 10C during the first two charge/discharge cycles.*

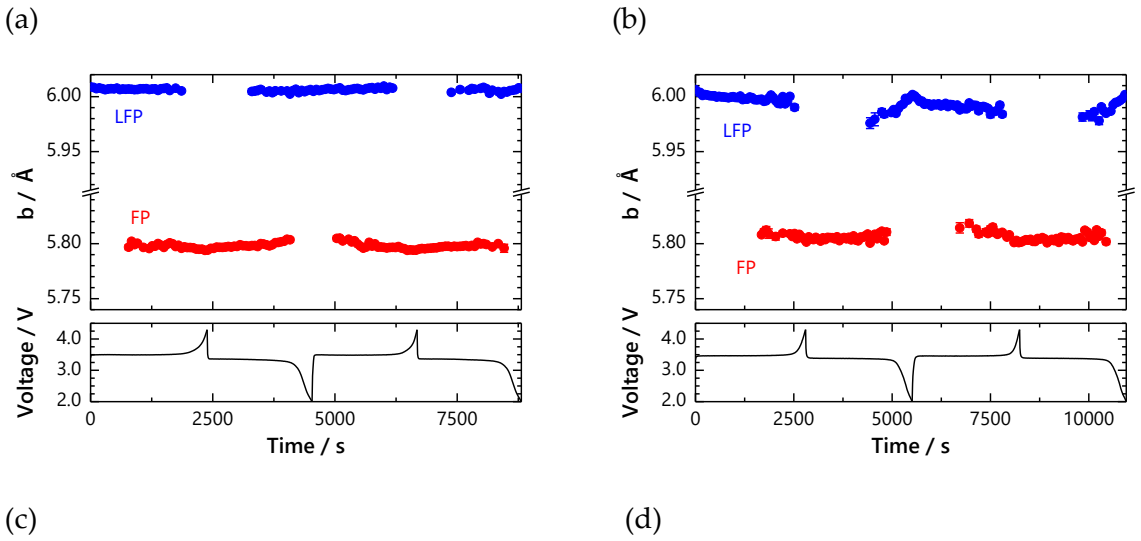

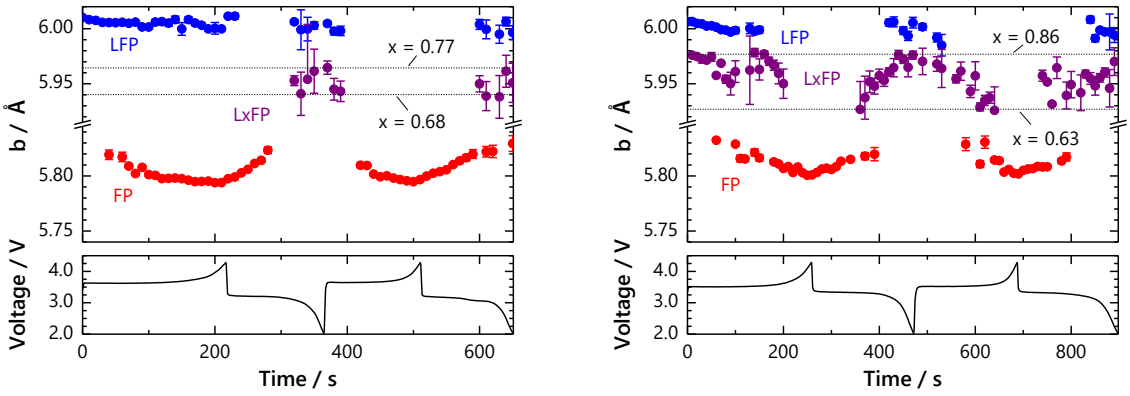

Figure 4.2. Time-resolved XRD patterns during charge/discharge cycling at 25°C. *(a) $LiFePO_4$ and (b) $Li(Fe_{0.95}Zr_{0.05})(P_{0.9}Si_{0.1})O_4$ at a low rate of 1C and (c) $LiFePO_4$ and (d) $Li(Fe_{0.95}Zr_{0.05})(P_{0.9}Si_{0.1})O_4$ at a high rate of 10C during the first two charge/discharge cycles.*

When the metastable intermediate phase observed at room temperature relates to the intermediate solid solution phase based on the phase diagram,[8, 20] the properties at high temperature gives insight into the development of the high rate electrode materials. Temperature-controlled XRD was conducted at the composition of x = 0.66 as shown in **Figure 4.3**. Both $Li_{0.66}FePO_4$ and $Li_{0.66}(Fe_{0.95}Zr_{0.05})(P_{0.9}Si_{0.1})O_4$ consist of only LFP and FP at room temperature. With increasing temperature, the intermediate solid solution phase is observed from 170°C in $Li_{0.66}(Fe_{0.95}Zr_{0.05})(P_{0.9}Si_{0.1})O_4$ and from 230°C in $Li_{0.66}FePO_4$. In the $Li(Fe_{0.95}Zr_{0.05})(P_{0.9}Si_{0.1})O_4$ system, the intermediate solid solution phase is thermodynamically more stable than $LiFePO_4$. The $LiMn_yFe_{1-y}PO_4$ system involves the intermediate phase at room temperature,[24] although the $Li_{1-3y}FeV_yPO_4$ involves the intermediate phase above 100°C.[25]

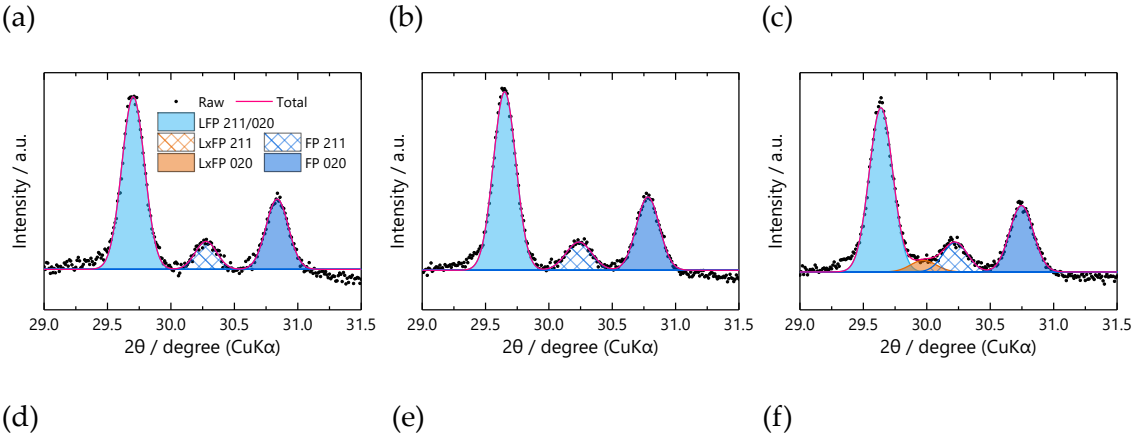

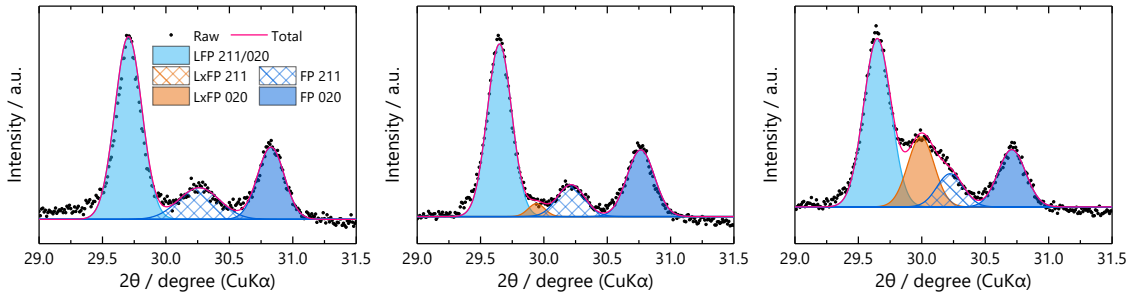

Figure 4.3. Temperature-controlled XRD patterns. *$LiFePO_4$ at (a) 25°C, (b) 170°C, (c) 230°C and $Li(Fe_{0.95}Zr_{0.05})(P_{0.9}Si_{0.1})O_4$ at (d) 25°C, (e) 170°C, (f) 230°C.*

The electrochemical measurements for $Li(Fe_{0.95}Zr_{0.05})(P_{0.9}Si_{0.1})O_4$ at high temperature were conducted as shown in **Figure 4.4**. The obtained capacity decreases with lower temperature due to the lower ionic conductivity of the molten salt electrolyte. This electrolyte is electrochemically unstable and exhibits the self-discharge so that the capacity on the charge is larger than that on the discharge. Nevertheless, we can roughly estimate the electrode property. $LiFePO_4$ shows the current-induced hysteretic behavior via the intermediate solid solution phase that emerges from 200°C as reported by Yoshinari *et al*.[17] In $Li(Fe_{0.95}Zr_{0.05})(P_{0.9}Si_{0.1})O_4$, the differential capacity plots (**Figure 4.4b**) calculated from the charge/discharge curves (**Figure 4.4a**) show two distinct peaks on the charge/discharge above 160°C, indicating that the intermediate solid solution phase involves at lower temperature than in $LiFePO_4$. This is consistent with the obtained temperature-controlled XRD patterns.

(a)

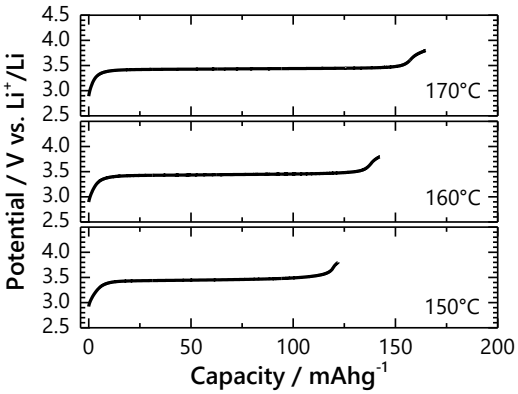

(b)

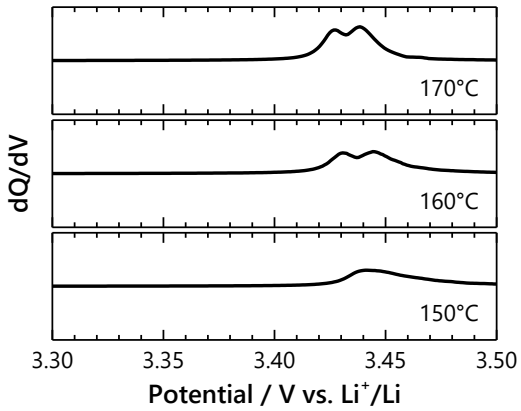

Figure 4.4. Electrochemical properties at elevated temperatures. *(a) Galvanostatic charge/discharge curves with (b) their differential capacity plots at 150°C, 160°C, and 170°C in* $Li(Fe_{0.95}Zr_{0.05})(P_{0.9}Si_{0.1})O_4$*. Current density was 17.0* mAg^{-1} *(1C) for all samples.*

Schematic illustration for the Gibbs free energy at room temperature is shown in **Figure 4.5**. At low current rates, the two phase transition reaction occurs in $LiFePO_4$ and $Li(Fe_{0.95}Zr_{0.05})(P_{0.9}Si_{0.1})O_4$ as observed **Figure 4.1a,b**. At high current rate, as the non-equibilium phase transition pathway is selected, the metastable intermediate phase takes greater responsibility for $Li(Fe_{0.95}Zr_{0.05})(P_{0.9}Si_{0.1})O_4$ than for $LiFePO_4$. The difference originates the enhancement of the rate capability with the consecutive phase transition in $Li(Fe_{0.95}Zr_{0.05})(P_{0.9}Si_{0.1})O_4$.

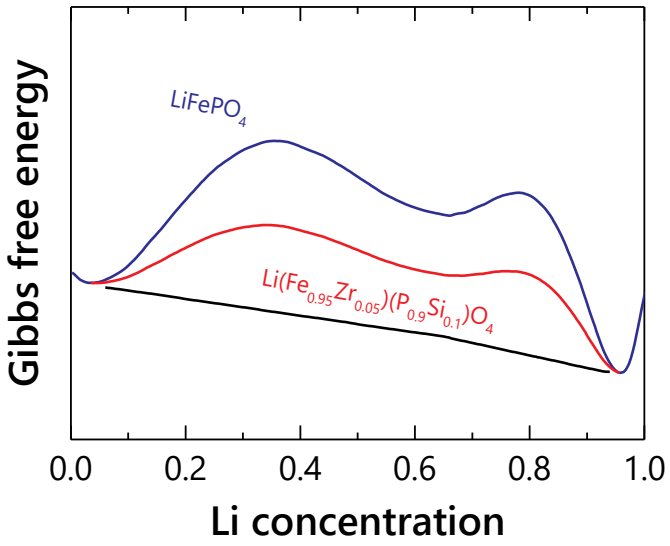

Figure 4.5. Schematic illustration of Gibbs free energy curves of $LiFePO_4$ ***and*** $Li(Fe_{0.95}Zr_{0.05})(P_{0.9}Si_{0.1})O_4$***.***

The idea that the intermediate phase is stabilized kinetically as well as thermodynamically is a crucial approach to make high-power Li-ion battery electrodes.

4.4. Conclusion

The role of the intermediate phase in $LiFePO_4$ and $Li(Fe_{0.95}Zr_{0.05})(P_{0.9}Si_{0.1})O_4$ is analyzed by combining time-resolved XRD, temperature-controlled XRD, and the electrochemical

tests at high temperature with the molten salt electrolyte. The metastable intermediate phase of $Li(Fe_{0.95}Zr_{0.05})(P_{0.9}Si_{0.1})O_4$ participates in a wider compositional range of itself and the total reaction than that of $LiFePO_4$ under high rate cycling, leading to the high rate performance with the consecutive phase transition. The intermediate phase of $Li(Fe_{0.95}Zr_{0.05})(P_{0.9}Si_{0.1})O_4$ is also thermodynamically more stable than that of $LiFePO_4$. To stabilize the intermediate phase kinetically as well as thermodynamically is a key to develop the high-power Li-ion battery material.

References

1. Huang, H.; Yin, S. C.; Nazar, L. F., Approaching Theoretical Capacity of $LiFePO_4$ at Room Temperature at High Rates. *Electrochem. Solid-State Lett.* **2001,** *4* (10), A170-A172.

2. Delacourt, C.; Poizot, P.; Levasseur, S.; Masquelier, C., Size Effects on Carbon-Free $LiFePO_4$ Powders. *Electrochem. Solid-State Lett.* **2006,** *9* (7), A352-A355.

3. Kobayashi, G.; Nishimura, S. I.; Park, M. S.; Kanno, R.; Yashima, M.; Ida, T.; Yamada, A., Isolation of Solid Solution Phases in Size-Controlled Li_xFePO_4 at Room Temperature. *Adv. Funct. Mater.* **2009,** *19* (3), 395-403.

4. Wagemaker, M.; Singh, D. P.; Borghols, W. J. H.; Lafont, U.; Haverkate, L.; Peterson, V. K.; Mulder, F. M., Dynamic Solubility Limits in Nanosized Olivine $LiFePO_4$. *J. Am. Chem. Soc.* **2011,** *133* (26), 10222-10228.

5. Burch, D.; Bazant, M. Z., Size-Dependent Spinodal and Miscibility Gaps for Intercalation in Nanoparticles. *Nano Lett.* **2009,** *9* (11), 3795-3800.

6. Meethong, N.; Huang, H. Y. S.; Carter, W. C.; Chiang, Y. M., Size-Dependent Lithium Miscibility Gap in Nanoscale $Li_{1-x}FePO_4$. *Electrochem. Solid-State Lett.* **2007,** *10* (5), A134-A138.

7. Yamada, A.; Koizumi, H.; Nishimura, S. I.; Sonoyama, N.; Kanno, R.; Yonemura, M.; Nakamura, T.; Kobayashi, Y., Room-Temperature Miscibility Gap in Li_xFePO_4. *Nat. Mater.* **2006,** *5* (5), 357-360.

8. Dodd, J. L.; Yazami, R.; Fultz, B., Phase Diagram of Li_xFePO_4. *Electrochem. Solid-State Lett.* **2006,** *9* (3), A151-A155.

9. Meethong, N.; Kao, Y. H.; Carter, W. C.; Chiang, Y. M., Comparative Study of Lithium Transport Kinetics in Olivine Cathodes for Li-Ion Batteries. *Chem. Mater.* **2010,** *22* (3), 1088-1097.

10. Omenya, F.; Chernova, N. A.; Wang, Q.; Zhang, R. B.; Whittingham, M. S., The Structural and Electrochemical Impact of Li and Fe Site Substitution in $LiFePO_4$. *Chem. Mater.* **2013,** *25* (13), 2691-2699.

11. Yamada, A.; Kudo, Y.; Liu, K. Y., Phase Diagram of $Li_x(Mn_yFe_{1-y})PO_4$ ($0 <= x, y <= 1$). *J. Electrochem. Soc.* **2001,** *148* (10), A1153-A1158.

12. Gwon, H.; Seo, D. H.; Kim, S. W.; Kim, J.; Kang, K., Combined First-Principle Calculations and Experimental Study on Multi-Component Olivine Cathode for Lithium Rechargeable Batteries. *Adv. Funct. Mater.* **2009,** *19* (20), 3285-3292.

13. Nam, K. W.; Wang, X. J.; Yoon, W. S.; Li, H.; Huang, X. J.; Haas, O.; Bai, J. M.; Yang, X. Q., In Situ X-ray Absorption and Diffraction Studies of Carbon Coated $LiFe_{1/4}Mn_{1/4}Co_{1/4}Ni_{1/4}PO_4$ Cathode during First Charge. *Electrochem. Commun.* **2009,** *11* (4), 913-916.

14. Park, K. Y.; Hong, J.; Kim, J.; Park, Y. U.; Kim, H.; Seo, D. H.; Kim, S. W.; Choi, J. W.; Kang, K., Factors that Affect the Phase Behavior of Multi-Component Olivine ($LiFe_xMn_yCo_{1-x-y}PO_4$; $0 < x, y < 1$) in Lithium Rechargeable Batteries: One-Phase Reaction vs. Two-Phase Reaction. *J. Electrochem. Soc.* **2013,** *160* (3), A444-A448.

15. Ravnsbaek, D. B.; Xiang, K.; Xing, W. T.; Borkiewicz, O. J.; Wiaderek, K. M.; Gionet, P.; Chapman, K. W.; Chupas, P. J.; Tang, M.; Chiang, Y. M., Engineering the Transformation Strain in $LiMn_yFe_{1-y}PO_4$ Olivines for Ultrahigh Rate Battery Cathodes. *Nano Lett.* **2016,** *16* (4), 2375-2380.

16. Nishijima, M.; Ootani, T.; Kamimura, Y.; Sueki, T.; Esaki, S.; Murai, S.; Fujita, K.; Tanaka, K.; Ohira, K.; Koyama, Y.; Tanaka, I., Accelerated Discovery of Cathode Materials with Prolonged Cycle Life for Lithium-Ion Battery. *Nat. Commun.* **2014,** *5*.

17. Yoshinari, T.; Yamamoto, K.; Nishijima, M.; Fukuda, K.; Kuwabara, A.; Tanaka, I.; Maeda, K.; Kageyama, H.; Orikasa, Y.; Uchimoto, Y., High Rate Performance of Dual-Substituted $LiFePO_4$ Based on Controlling Metastable Intermediate Phase. *ACS Appl. Energy Mater.* **2018,** *1* (12), 6736-6740.

18. Ravnsbaek, D. B.; Xiang, K.; Xing, W.; Borkiewicz, O. J.; Wiaderek, K. M.; Gionet, P.; Chapman, K. W.; Chupas, P. J.; Chiang, Y. M., Extended Solid Solutions and Coherent Transformations in Nanoscale Olivine Cathodes. *Nano Lett.* **2014,** *14* (3), 1484-1491.

19. Orikasa, Y.; Maeda, T.; Koyama, Y.; Murayama, H.; Fukuda, K.; Tanida, H.; Arai, H.; Matsubara, E.; Uchimoto, Y.; Ogumi, Z., Direct Observation of a Metastable Crystal Phase of Li_xFePO_4 under Electrochemical Phase Transition. *J. Am. Chem. Soc.* **2013,** *135* (15), 5497-5500.

20. Delacourt, C.; Poizot, P.; Tarascon, J. M.; Masquelier, C., The Existence of a Temperature-Driven Solid Solution in Li_xFePO_4 for $0 <= x <= 1$. *Nat. Mater.* **2005,** *4* (3), 254-260.

21. Chen, G. Y.; Song, X. Y.; Richardson, T. J., Metastable Solid-Solution Phases in the $LiFePO_4/FePO_4$ System. *J. Electrochem. Soc.* **2007,** *154* (7), A627-A632.

22. Koyama, Y.; Uyama, T.; Orikasa, Y.; Naka, T.; Komatsu, H.; Shimoda, K.; Murayama, H.; Fukuda, K.; Arai, H.; Matsubara, E.; Uchimoto, Y.; Ogumi, Z., Hidden Two-Step Phase Transition and Competing Reaction Pathways in $LiFePO_4$. *Chem. Mater.* **2017,** *29* (7), 2855-2863.

23. Bai, P.; Cogswell, D. A.; Bazant, M. Z., Suppression of Phase Separation in $LiFePO_4$ Nanoparticles during Battery Discharge. *Nano Lett.* **2011,** *11* (11), 4890-4896.

24. Malik, R.; Zhou, F.; Ceder, G., Phase Diagram and Electrochemical Properties of Mixed Olivines from First-Principles Calculations. *Phys. Rev. B* **2009,** *79* (21).

25. Omenya, F.; Chernova, N. A.; Zhang, R. B.; Fang, J.; Huang, Y. Q.; Cohen, F.; Dobrzynski, N.; Senanayake, S.; Xu, W. Q.; Whittingham, M. S., Why Substitution Enhances the Reactivity of $LiFePO_4$. *Chem. Mater.* **2013,** *25* (1), 85-89.

Chapter 5.

Fast lithium ion intercalation/deintercalation at the interface between surface-nitrided $LiFePO_4$ electrode and electrolyte

Improving rate performance in lithium ion batteries is important to spread utilization of electric vehicles and/or energy grids. Because rate-determining step of cathode materials proceed via a two-phase reaction is nucleation at material surface, surface modification is a promising approach to improve the rate performance of cathode material in lithium ion battery. However, the reaction mechanism at the interface between the surface-modified cathode and electrolyte has not been understood clearly. Herein we prepared a surface-nitrided $LiFePO_4$ thin film and investigated the electrochemical property. Also, we examined the surficial structure of the surface-nitrided $LiFePO_4$ thin film by surface-sensitive X-ray absorption spectroscopy (XAS) measurements and first principles calculations, discussing a correlation between the rate performance and the interfacial reaction. The experiments proved a new energy level formation and extended Fe-O bond distance at the surface of $LiFePO_4$ by the surface-nitride treatment. The electronic and local structure changes accelerate lithium ions transportation at the interface between surface-nitrided $LiFePO_4$ and electrolyte, improving the rate performance.

5.1. Introduction

Lithium ion batteries (LIBs) are key for realizing electric vehicles and/or sustainable energy grids because their energy density is highest among commercially available batteries[1], but further performance improvement is demanded. The rate performance is a pivotal property of LIBs. $LiFePO_4$ exhibits a large capacity at high rates of charge and discharge.[2] Although charge and discharge reactions proceed via a two-phase reaction between $LiFePO_4$ and $FePO_4$, which is detrimental for the electrochemical capacity at higher electrochemical reaction rates,[3,4] reducing the particle size and carbon coating of the $LiFePO_4$ solved this problem.[5-7]

In order to improve the rate performance of two-phase system, controlling the interface between electrode and electrolyte is important because nucleation reaction at interface is the starting point.[8] In the $LiFePO_4$, the nucleation reaction is considerably slower than the nuclear growth reaction.[9-13] Anion surface modification of $LiFePO_4$ has been reported as a promising approach for accelerating the interfacial reaction.[14] It has been predicted by theoretical calculation that the surface modification of $LiFePO_4$ with nitrogen or sulfur anions changes the electronic and local structure of $LiFePO_4$, reducing the energy barrier of the interfacial reaction.[15,16] However, the electronic and local structure of the surface-modified $LiFePO_4$ has not been experimentally investigated, and the mechanism behind improving the interfacial reaction rate upon anion surface modification is not clearly understood.

Herein, a correlation among the nucleation behavior, electronic and local structure of surface-modified $LiFePO_4$ was investigated. A surface-nitrided $LiFePO_4$ thin-film was prepared as a model electrode because focus on the interfacial reaction between electrode and electrolyte in composite electrode is difficult due to the complex three-dimensional matrix. We measured the surficial structure of the surface-nitrided $LiFePO_4$ thin film by surface-sensitive X-ray absorption spectroscopy (XAS) and discuss the relationship between the rate performance and the surficial structure by combination of first principles calculations.

5.2. Experimental

5.2.1. Synthesis of materials and Electrochemical characterization

The model $LiFePO_4$ thin-films electrodes were prepared on Au polycrystalline substrates using a pulsed laser deposition technique (PLD). A Nd:YAG 4HG laser with a wavelength of 266 nm was used as the light source. The pulse irradiation frequency was fixed at 10 Hz, and the laser power was adjusted to 200 mW. $LiFePO_4$ (Mitsui Engineering & Shipbuilding) was pelletized to use as the target. The distance between the target and substrate was 40 mm. The prepared $LiFePO_4$ thin-film was polycrystalline with thicknesses of 70 nm, respectively, as previously reported.[1] The preparation of the $LiFePO_4$ thin-films was conducted under Ar of 0.0001 Pa at 923 K for 30 min of deposition time. For surface-nitrided treatment, the prepared $LiFePO_4$ thin-film was annealed at 600°C for 10 min under and NH_3 atmosphere.

Three-electrode cells were used for electrochemical measurements. The working electrode was the prepared thin-film electrode, the counter electrode was Li metal and the reference electrode was Li metal. A 1 mol dm^{-3} of $LiClO_4$ in propylene carbonate was used as the electrolyte. Galvanostatic measurements were performed at various C rate from 2 C to 100 C at 25°C. Because charge and discharge reaction of the prepared thin-film finished about 1 hour, respectively with the current value of 0.5 μA, 0.5 μA was defined as 1 C rate. Cyclic voltammetry was conducted at various scan rate from 0.10 mV/s to 10 mV/s under the potential range between 3.0 and 4.0 V at 25°C using a potentiostat (HZ-5000, Hokuto Denko Corp.). Potential-step chronoamperometry was performed to the prepared thin-film electrodes under the potential range between 3.3–4.0 V with 10 mV of potential step at 25°C using a potentiostat (HZ-5000, Hokuto Denko Corp.). The thickness of the prepared thin-film was estimated from the capacity of cyclic voltammogram at potential range between 3.0 and 4.0 V at 25°C with a scan rate of 0.1 mV by using the bulk density of $LiFePO_4$ (3.6 g/cm^3) and the reaction area (ca. φ 6 mm).

5.2.2. Materials characterization

Depth-resolved X-ray absorption spectroscopy (DR-XAS) measurements were performed at the beamline BL37XU of SPring-8 with a two-dimensional pixel array detector, PILATUS (Dectris, Switzerland). Fe *K*-edge fluorescence XAS spectra were measured. Experimental detail of DR-XAS has been described in previous studies.[2,3] Soft X-ray absorption spectroscopy measurements were performed for N *K*-edge, O *K*-edge, Fe *L*-edge with total electron yield mode and fluorescence mode. The measurements

with total electron mode and partial fluorescence mode were conducted at the beamline BL11 of Ritsumeikan SR center and beamline BL27SU of SPring-8, Japan, respectively. Data analysis was performed with the REX2000 data analysis software, the backscattering phases and the amplitude were theoretically calculated by the code FEFF8. For the curve fitting of the Fe *K*-edge spectrum, we used a single Fe-O distance and fixed the coordination number to six.

5.3. Results and Discussion

The $LiFePO_4$ thin-film was prepared by pulsed laser deposition. The surface-nitride treatment was conducted to anneal the as-prepared $LiFePO_4$ thin-film at 600°C under an NH_3 atmosphere. Further details regarding the sample preparation conditions are described in supporting information. Hereafter, the as-prepared $LiFePO_4$ thin-film and the surface-nitrided $LiFePO_4$ thin-film are referred to as Bare-LFP and N-LFP, respectively. Galvanostatic charging and discharging measurements were performed for the Bare-LFP and N-LFP samples at 25°C as shown in **Figure 5.1**. Both of the samples exhibited a typical plateau at 3.45 V, which is attributed to the two-phase reaction of $LiFePO_4$ and $FePO_4$.[2] The charge capacity of the Bare-LFP at a 2 C rate was 165 mAh/g, which decreased to 91 mAh/g at a 100 C rate. On the other hand, the N-LFP showed 137 mAh/g the charge capacity at a 100 C rate. The rate performance enhancement of $LiFePO_4$ by surface-nitride treatment agrees with a previous report.[14]

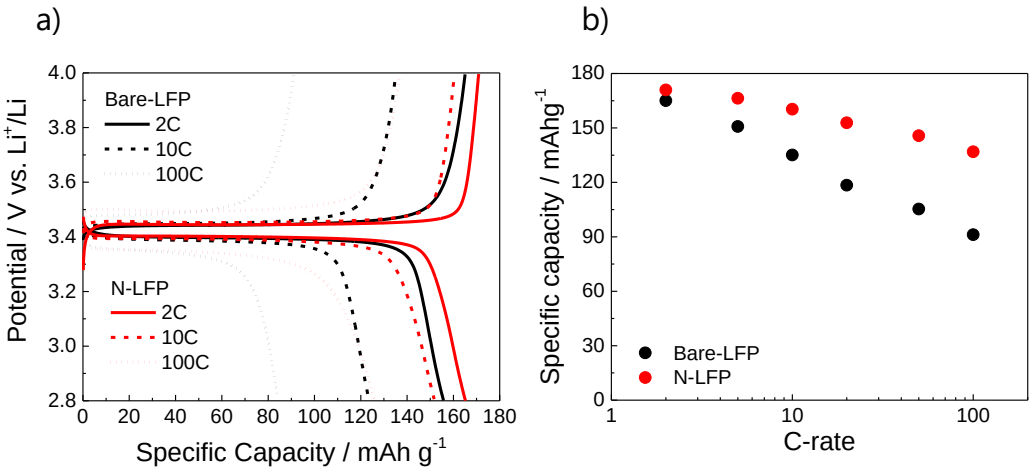

Figure 5.1. Electrochemical properties of the Bare-LFP and N-LFP. *(a) Charge and discharge curves and (b) Specific charge and discharge capacity as a function of C-rate.*

To evaluate the diffusion coefficient of lithium ions (D_{Li+}) during the charging process, we performed cyclic voltammetry and potentiostatic intermittent titration technique (PITT) measurements on the Bare-LFP and N-LFP (**Figure 5.2** and **Figure 5.3**). The D_{Li+} values of the Bare-LFP obtained from the CV and PITT measurements were 3.0×10^{-14} and 1.2×10^{-14} cm^2/s, respectively. These values agree with previous studies, which reported CV-determined vales between 10^{-14} and 10^{-13} cm^2/s[17-19] and PITT-determined values was between 10^{-14} and 10^{-12} cm^2/s.[17] The D_{Li+} value of the N-LFP obtained from PITT measurement was 1.7×10^{-14} cm^2/s, which is similar to the value of the Bare-LFP. However, the D_{Li+} value obtained from CV measurements for the N-LFP was 8.0×10^{-14} cm^2/s that is much higher than that of the Bare-LFP. D_{Li+} value obtained from the PITT measurements mainly reflects the diffusion of lithium ions in bulk,[20] whereas the D_{Li+} value obtained from the CV measurements reflects the reaction over the entire electrode including in the bulk and at the electrode/electrolyte interface.[21,22] These results indicate that the surface-nitride treatment enhanced the lithium ion transportation at the electrode/electrolyte interface and the bulk lithium ion diffusion remained unaffected by the treatment.

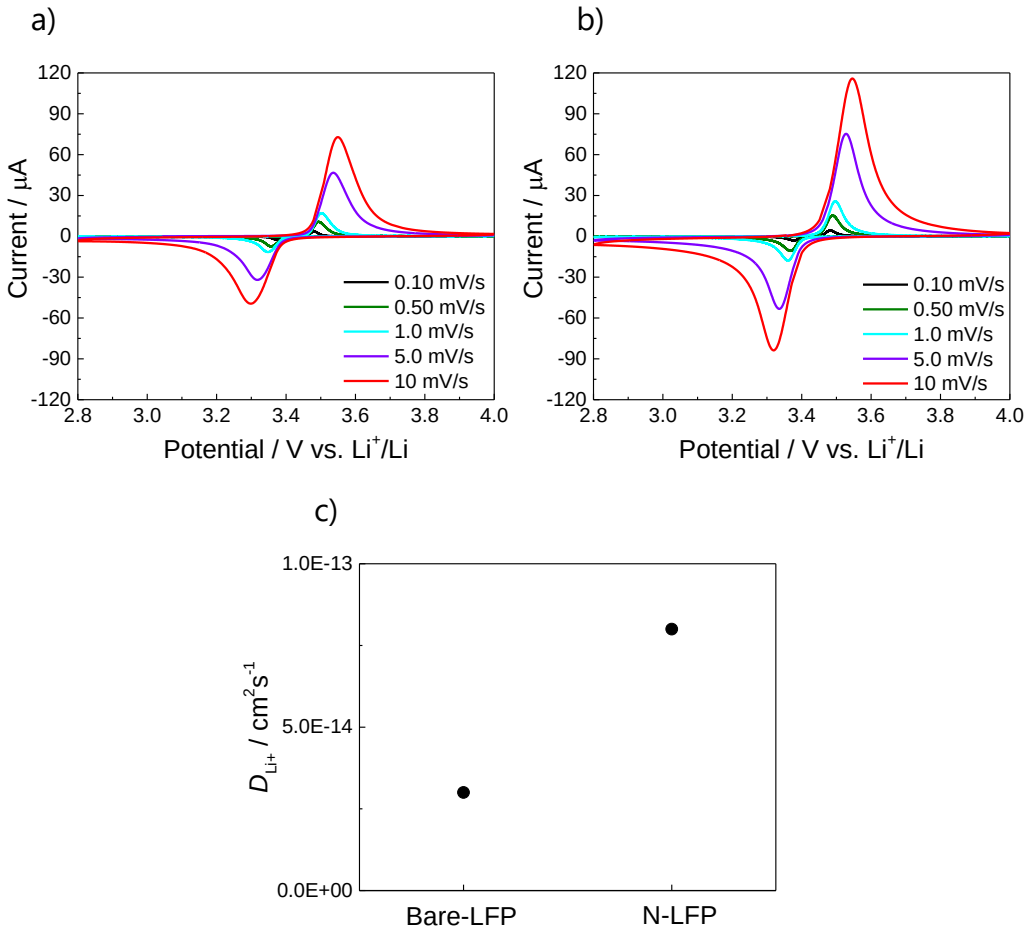

Figure 5.2. *Cyclic voltammograms of (a) the Bare-LFP and (b) the N-LFP at scan rates ranging from 0.1 mV/sec to 2.0 mV/sec. (c) Diffusion coefficients calculated from the CVs under charging process for the Bare LFP and N-LFP.*

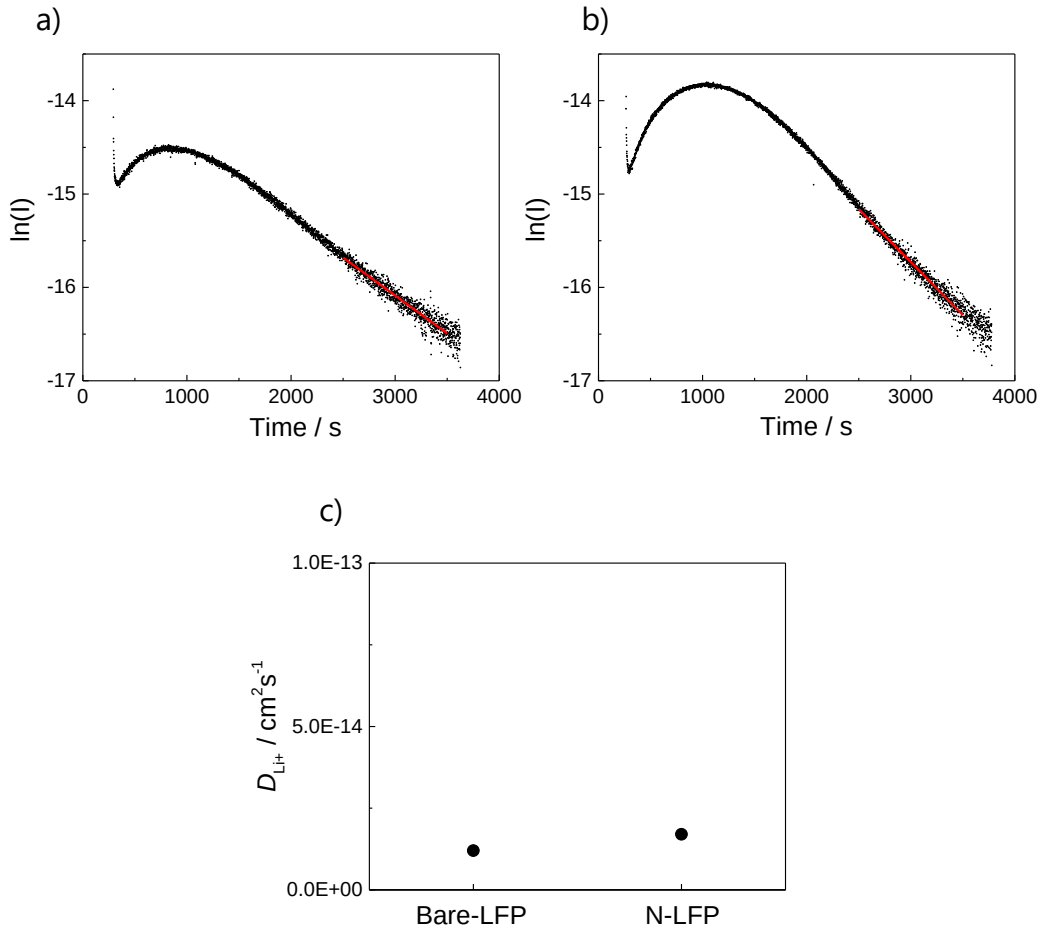

***Figure* 5.3.** *Time dependence of the transient current of (a) the Bare-LFP with a potential step from 3.43 to 3.44 V and (b) the N-LFP with a potential step from 3.44 to 3.45 V. (c) Diffusion coefficients calculated from the PITT method for the Bare LFP and N-LFP. The red line drawn in (a) and (b) is fitting result to calculate the diffusion coefficient for the Bare LFP and N-LFP.*

To examine the electronic structure of the Bare-LFP and N-LFP, soft X-ray absorption spectroscopy (SXAS) was performed in the energy region of the N *K*-edge and O *K*-edge. **Figure 5.4a** shows the N *K*-edge SXAS spectra of the Bare-LFP and N-LFP. No response was observed in the Bare-LFP spectrum, whereas a sharp peak at 401 eV was observed in the N-LFP spectrum, indicating that nitrogen species exist in the N-LFP. Similar spectral features were observed for the N-LFP with nitrogen-implanted ZrO_2.[23] **Figure 5.4**b and **c** show the O *K*-edge SXAS spectra obtained via total electron yield (TEY) and partial fluorescence yield (PFY) modes for the Bare-LFP and N-LFP. The TEY mode obtains data regarding sample surface, while the PFY mode probes mainly the bulk of

the sample.[24,25] The spectra obtained in the PEY mode for both samples show a broad peak above 532 eV, which is attributed to the transition of the O 1*s* electron to the hybridized states of Fe 4*sp* and O 2*p* orbitals.[26] The N-LFP spectrum was almost same as that of the Bare-LFP, indicating that the surface-nitride treatment did not change the electronic structure of the bulk. In contrast to the PFY mode, the TEY mode showed a difference between the spectra of the Bare-LFP and N-LFP. The spectra obtained in TEY mode of the Bare-LFP mode shows a pre-edge peak at approximately 531.8 eV in addition to the broad peak above 532 eV. The energy of the pre-edge was previously reported to be 531.8 eV,[27] which is agreement with the results presented herein. This pre-edge peak is attributed to the transition of the O 1*s* electron to the hybridized states of the Fe 3*d* and O 2*p* orbitals.[26]Although the N-LFP also shows a pre-edge at 531.8 eV, the new peak at 528 eV appeared. Because the peak position of the pre-edge of $FePO_4$ was reported to be 531.8 eV[27], the new peak of the N-LFP was not attributed to the peak of $FePO_4$. In addition, for Fe *L*-edge SXAS measurements of the Bare-LFP and N-LFP, the TEY mode exhibited a change between the spectra of the Bare-LFP and N-LFP, supporting the electronic structure change of $LiFePO_4$ by surface-nitride treatment (**Figure 5.5**). This indicates that nitrogen species were introduced to the surface of $LiFePO_4$ by surface-nitride treatment and formed new energy level with the Fe 3*d* and O 2*p* orbitals.

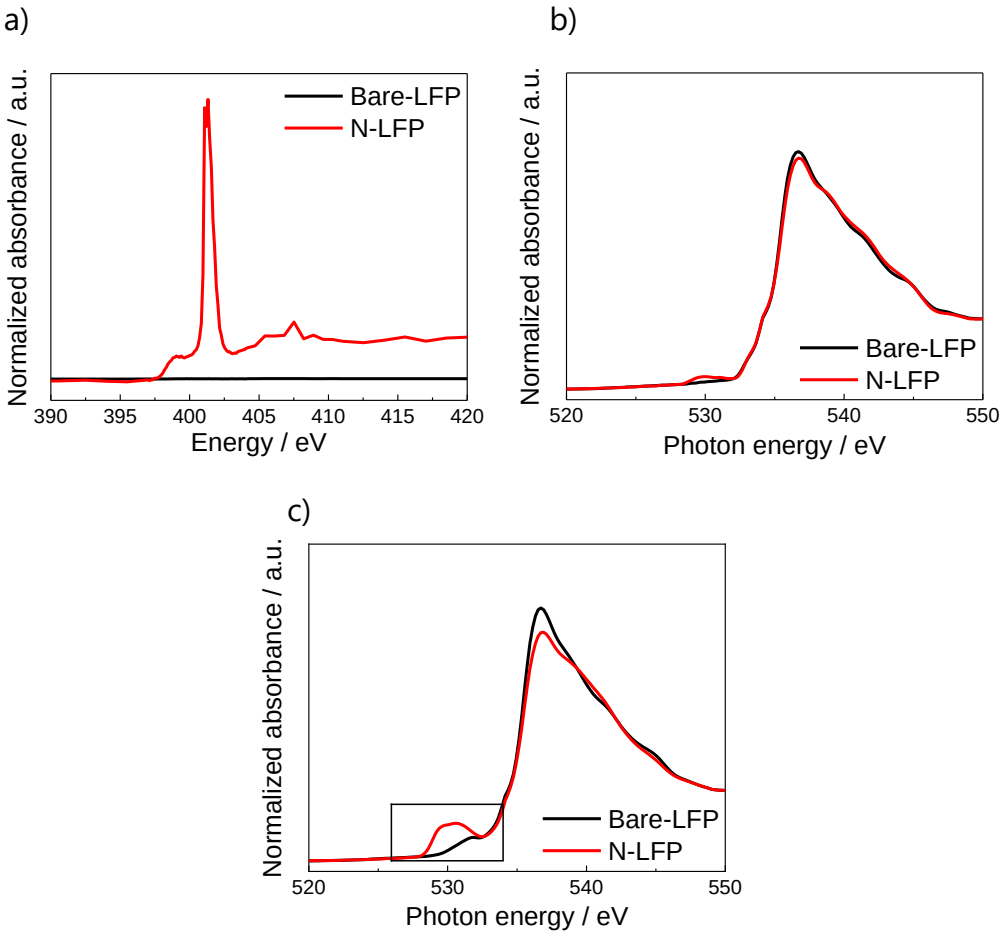

Figure 5.4. Soft X-ray absorption spectra of the Bare-LFP and N-LFP. *(a) N K-edge SXAS spectra obtained via PEY mode, (b) O K-edge SXAS spectra obtained via PFY mode and (c) O K-edge SXAS spectra obtained via TEY mode.*

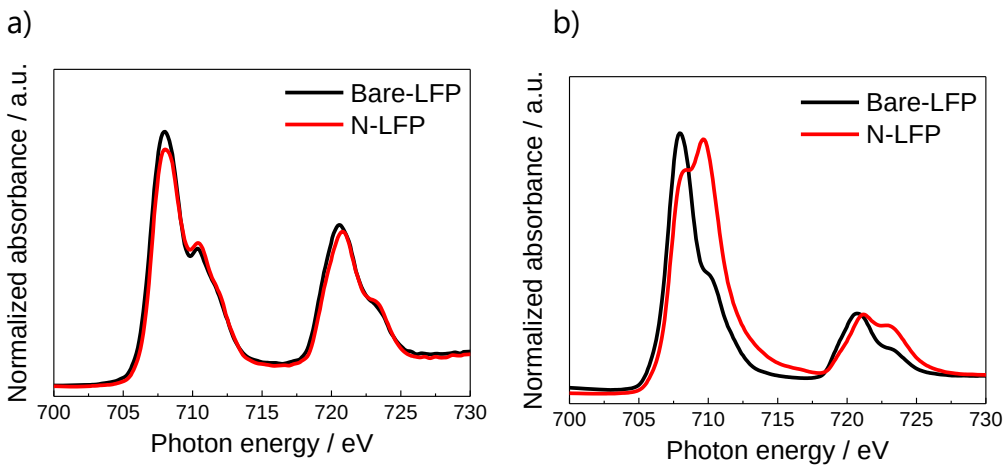

Figure 5.5. *Soft X-ray absorption spectra of the Bare-LFP and N-LFP. (a) Fe L-edge SXAS spectra obtained via PFY mode, (b) Fe L-edge SXAS spectra obtained via TEY mode.*

The electronic structures of the Bare-LFP and N-LFP were also examined using first-principles calculations. The density of states of states (DOS) at the (010) surface of the Bare-LFP and N-LFP are shown in **Figure 5.6**. The partial density of states (pDOS) for Fe at the (010) surface for the Bare-LFP, N-LFP and $FePO_4$ are shown in **Figure 5.7**, and the pDOS of nitrogen and oxygen at the (010) surface are shown in **Figure 5.8**. The DOS suggests that nitrogen doping forms new energy level between the valence and conduction bands in $LiFePO_4$. At the (010) surface in the N-LFP, energy levels hardly exist within the bandgap of the pDOS of Fe coordinated by O, whereas a sharp energy level exist in the bandgap of the pDOS of Fe coordinated by N. In addition, the pDOS of Fe coordinated by O in the N-LFP resembles that of the Fe coordinated by O in $LiFePO_4$, whereas the pDOS of Fe coordinated by N in the N-LFP resembles that of the Fe coordinated by O in $FePO_4$. This suggests that oxidation occurs in the Fe coordinated by N, which agrees with the SXAS measurements. Moreover, the pDOS of N exhibits a sharp energy level in the unoccupied molecular orbital above ca. 2 eV from the Fermi energy. This is coincident with the sharp peak observed in the N *K*-edge XAS, supported that N was successfully doped on the surface of the $LiFePO_4$.

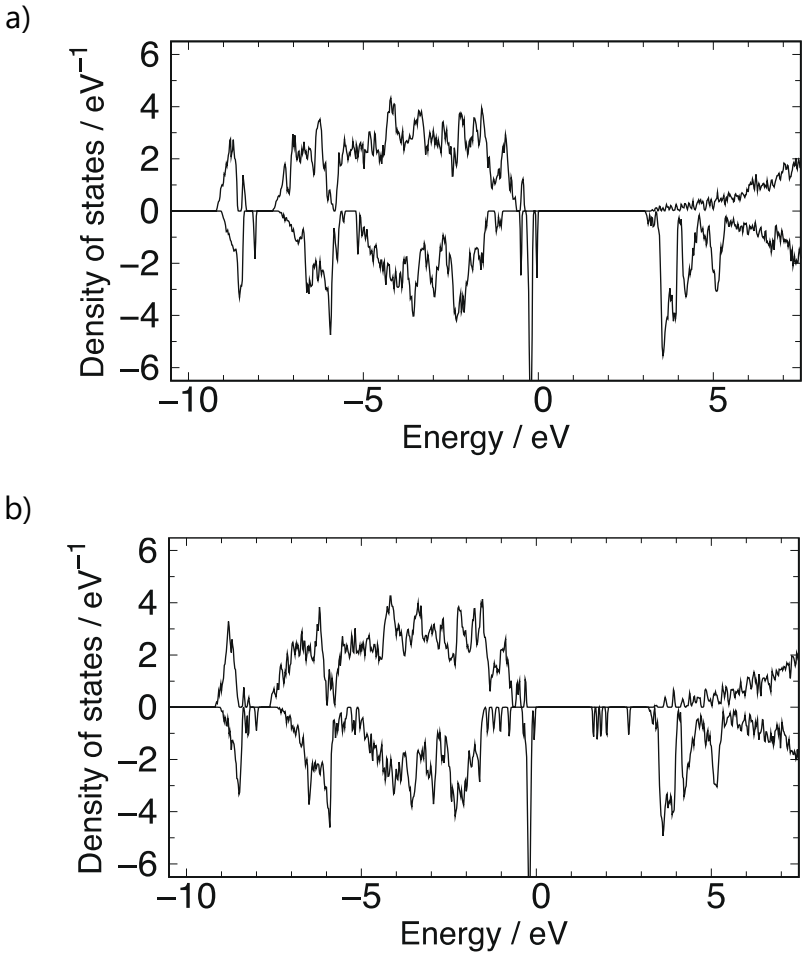

Figure 5.6. *Density of States of the (010) surface for (a) the Bare-LFP and (b) N-LFP.*

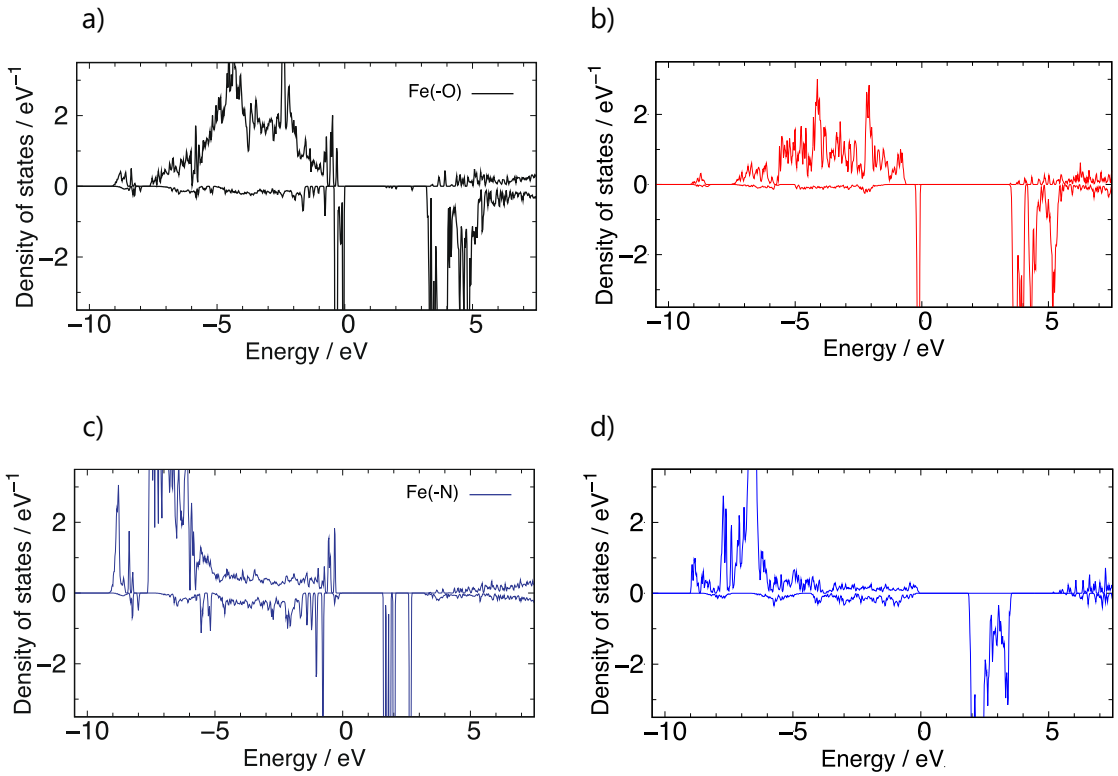

Figure 5.7. *Partial density of states for Fe. (a) pDOS for Fe coordinated by O at the (010) surface in N-LFP , (b) pDOS for Fe coordinated by O in $LiFePO_4$, (c) pDOS for Fe coordinated by N at the (010) surface in N-LFP and (d) pDOS for Fe coordinated by O in $FePO_4$.*

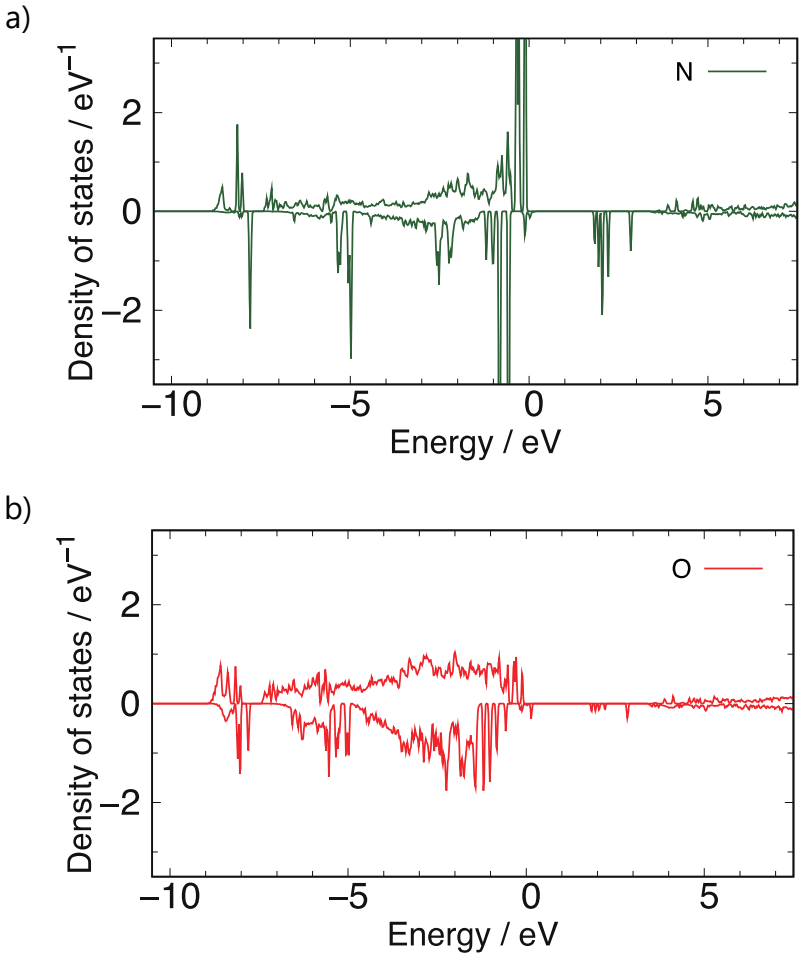

Figure 5.8. *Partial density of states for (a) N and (b) O in the N-LFP.*

To examine the electronic and local structure change around the Fe species in $LiFePO_4$ with surface-nitride treatment, we applied depth resolved-XAS (DR-XAS) technique of the Fe *K*-edge in both samples. The DR-XAS can monitor electronic and local structure from the surface to bulk with a depth resolution of 3–4 nm.[28] In the DR-XAS spectra obtained at lower exit angles, information from the surface of a thin-film can be obtained, while the spectra obtained at higher exit angles includes more information from both the surface and bulk of the thin-film.[28] The oxidation state of both samples was analyzed by X-ray absorption near edge structure (XANES) in the obtained XAFS spectra (**Figure 5.9**). The edge energy as a function of exit angle is plotted in **Figure 5.10a**. The edge energy of the Bare-LFP was nearly constant at all exit angles, whereas that of the N-LFP increased from 7117.8 to 7118.5 eV from 0.352° to 0.176°. The edge energy of the N-LFP

was higher than that of the Bare-LFP by at least 0.3 eV. This indicates that Fe ions at the surface of the N-LFP were oxidized to a larger extent than those of the Bare-LFP.

The interatomic distance and Debye-Waller (DW) factor for the Fe-O bonds were derived from extended X-ray absorption fine structure (EXAFS) analysis for both samples and are plotted as a function of exit angle in **Figure 5.10b** and **c**. The fitting results of the EXAFS oscillation are shown in **Figure 5.11** and **Figure 5.12**. The DW factor reflects static local distortions of the Fe-O bonds. The standard error of the Fe-O distance was less than 0.011 Å and the DW factor of the Fe-O bond was less than 0.015 $Å^{-1}$. Although the EXAFS analysis in the DR-XAFS exhibited relatively large standard errors, the tendencies of the bond distance and DW factors of Fe-O from the surface to the bulk can still be discussed, as has been previously reported.[28,29] The surface-nitride treatment changed the local structure at the surface of the $LiFePO_4$. The Fe-O bond distance of the N-LFP was longer than that of the Bare-LFP at lower exit angles. In addition, at lower exit angles it was observed that the DW factor of the N-LFP was larger than that of the Bare-LFP. This indicates that the local distortion around the Fe species increases at the surface of $LiFePO_4$ by the surface-nitride treatment. The XANES for the Fe *K*-edge obtained from DR-XAFS indicates oxidation of the Fe species at the surface of the N-LFP. However, the Fe-O bond distance obtained from the EXAFS analysis increased. Although these results seem discrepancy, it is caused by the local structure change with the substitution of oxygen coordinating to iron with nitrogen.

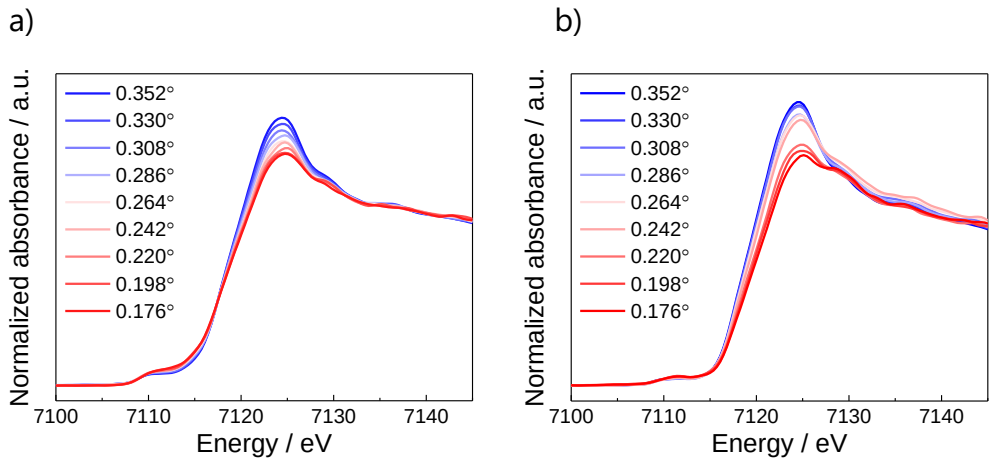

Figure 5.9. *XAS spectra of (a) the Bare-LFP and (b) N-LFP obtained from DR-XAS for Fe K-edge of at various exit angle. Low exit angles show closer to the surface.*

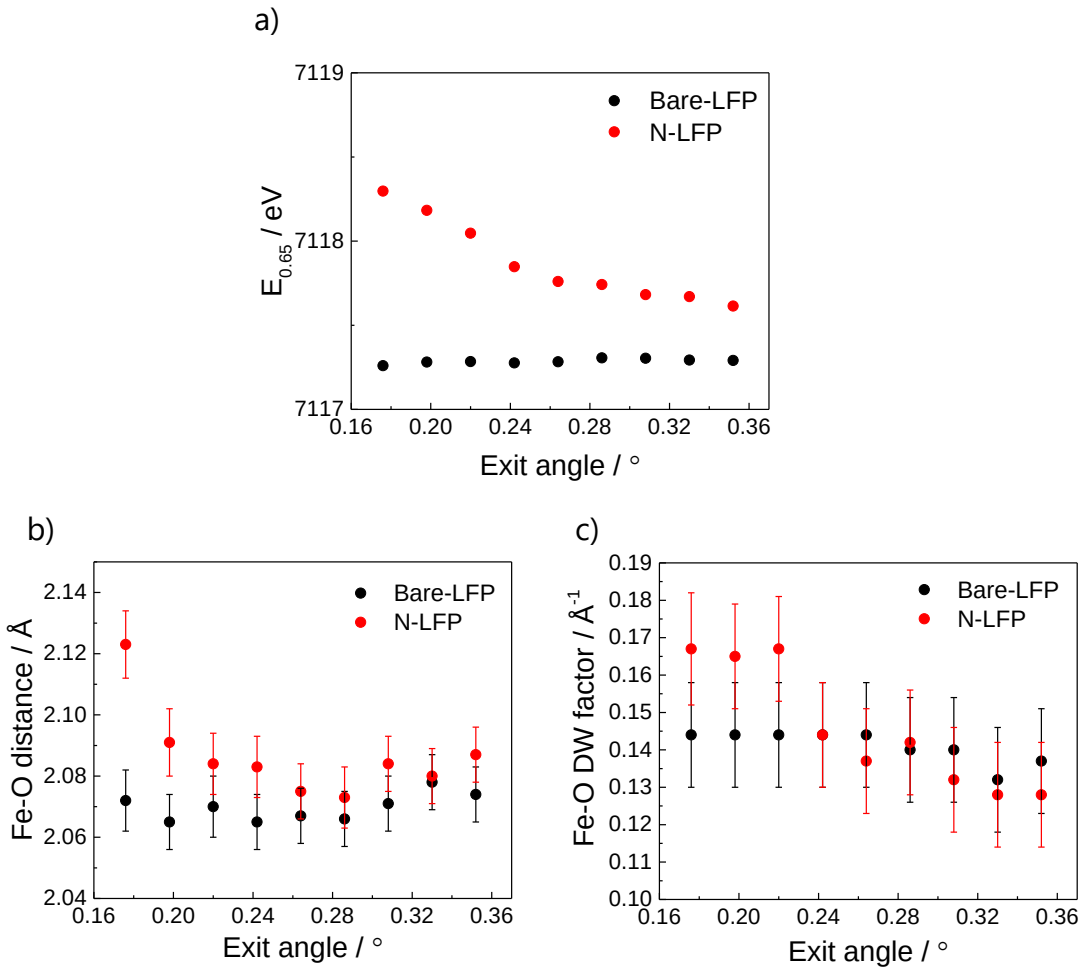

Figure 5.10. *Absorption edge energy and EXAFS analysis results obtained from Fe K-edge DR-XAS spectra for the Bare-LFP and N-LFP. (a) Absorption edge energy at a normalized intensity of 0.65, (b) Fe-O interatomic distance, and (c) Fe-O Debye Waller factors of the Bare-LFP and N-LFP at various exit angle. Low exit angles show closer to the surface.*

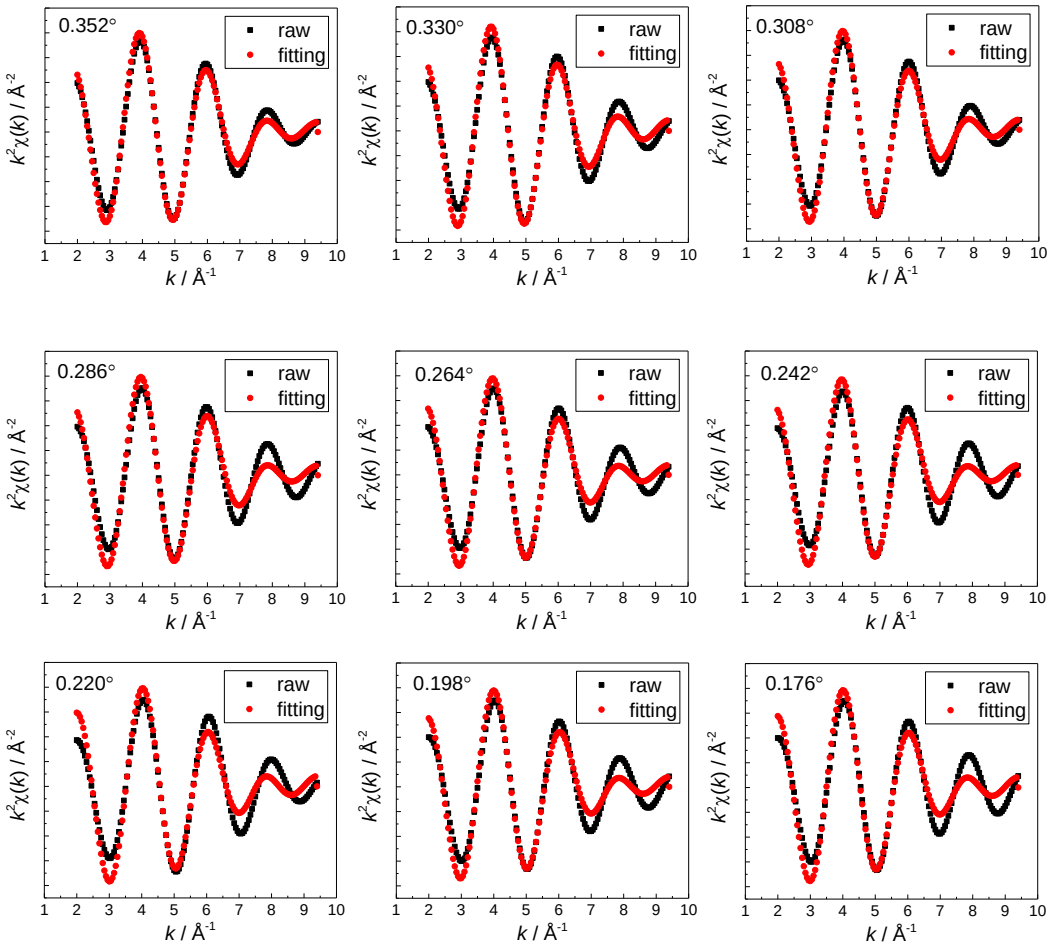

Figure 5.11. *The k²-weighted EXAFS oscillations and the fitting results of the Bare-LFP obtained at various exit angles. Low exit angles show closer to the surface.*

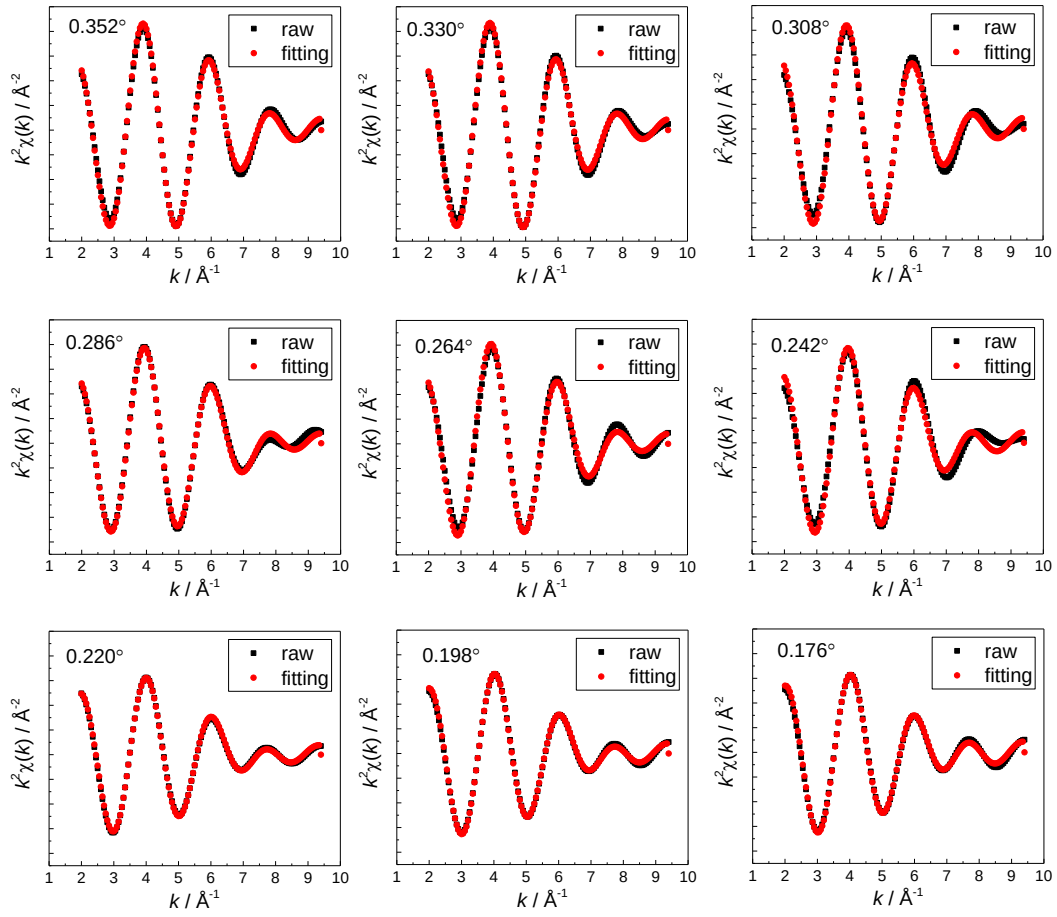

Figure 5.12. *The k²-weighted EXAFS oscillations and the fitting results of the N-LFP obtained at various exit angles. Low exit angles show closer to the surface.*

Herein, we explain the surface-nitride treatment enhancement of the rate performance of $LiFePO_4$ based on the electronic and local structure change. SXAS for the O *K*-edge and DR-XAS for the Fe *K*-edge showed that the surface-nitride treatment forms a new energy level and extends the Fe-O bond distance at the surface of $LiFePO_4$ (Figure 5). The formation of the new energy level was confirmed by first principles calculations. The improved rate performance by the surface-nitride treatment can be attributed to enhanced electronic conductivity and lithium ion transportation at the interface between $LiFePO_4$ and electrolyte. The new energy level reduces the bandgap of $LiFePO_4$, improving the electronic conductivity at the surface. The extended Fe-O bond distance caused by surface-nitride treatment weakens electrostatic repulsion between Li and Fe during lithium ion hopping, enhancing lithium ion transportation at the interface. The

enhanced electronic conductivity and lithium ion transportation accelerate nucleation reaction at the interface, resulting in fast lithium ion intercalation/deintercalation.

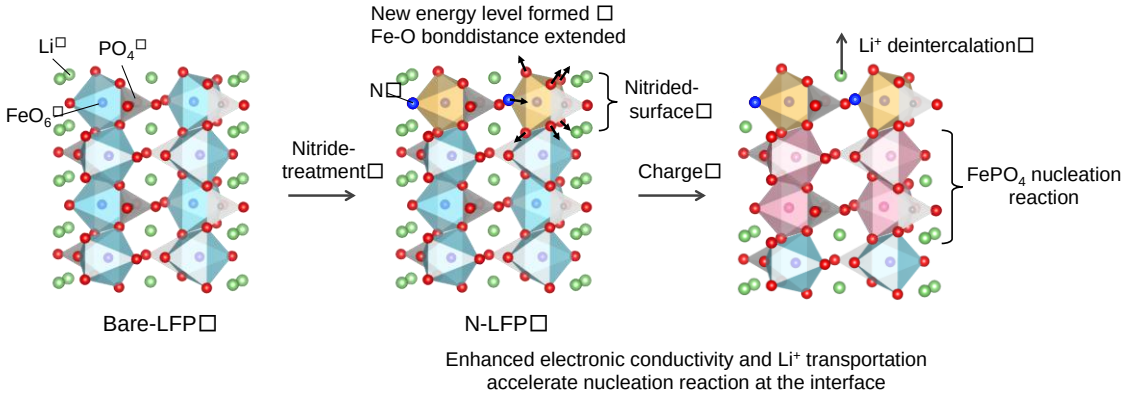

Figure 5.13. *Schematic illustration of the improvement mechanism of the rate performance of $LiFePO_4$ with surface-nitride treatment.*

5.4. Conclusion

In summary, we prepared a surface-nitrided $LiFePO_4$ thin film and examined the correlation between the electrochemical properties and surficial structure. The surface-nitride treatment increased the interfacial reaction rate between electrode and electrolyte interface. The SXAS for O *K*-edge and first principle calculations exhibited a new energy level formation at the surface of $LiFePO_4$ by the surface-nitride treatment. The DR-XAS showed that the Fe-O bond distance increased at the surface of $LiFePO_4$ by the surface-nitride treatment. The new energy level and extended Fe-O bond distance accelerates electronic conductivity and lithium ions transportation at the interface between surface-nitrided $LiFePO_4$ and electrolyte, improving the rate performance. The controlling electronic and local structure by anion doping to prepare mixed-anion compound[30] demonstrated in this study can be applied for $LiFePO_4$ but also for other two-phase systems to improve the rate performance.

References

1. B. Dunn, H. Kamath, J.-M. Tarascon, *Science* **2011**, 334, 928–935.

2. A. K. Padhi, K. S. Nanjundaswamy, J. B. Goodenough. *J. Electrochem. Soc.* **1997**, 144,

1188–1194.

3. C. Delacourt, P. Poizot, J.-M. Tarascon, C. Masquelier, *Nat. Mater.* **2005**, 4, 254–260.

4. A. Yamada, H. Koizumi, S.-I. Nishimura, N. Sonoyama, R. Kanno, M. Yonemura, T. Nakamura, Y. Kobayashi, *Nat. Mater.* 2006, 5, 357–360.

5. A. Yamada, S. C. Chung, K. Hinokuma, *J. Electrochem. Soc.* **2001**, 148, A224–A229.

6. H. Huang, S.-C. Yin, L. F. Nazar, *Electrochem. Solid-State Lett.* **2001**, 4, A170–A172.

7. Y. Wang, Y. Wang, E. Hosono, K. Wang, H. Zhou, *Angew. Chem. Int. Ed.* 2008, 47, 7461–7465.

8. K. Xu, A. v. Cresce, A. *J. Mater. Chem.* **2011**, 21, 9849.

9. C. Delmas, M. Maccario, L. Croguennec, F. Le Cras, F. Weill, *Nat. Mater.* **2008**, 7, 665–671.

10. Y. Orikasa, T. Maeda, Y. Koyama, T. Minato, H. Murayama, K. Fukuda, H. Tanida, H. Arai, E. Matsubara, Y. Uchimoto, Z. Ogumi, *J. Electrochem. Soc.* **2013**, 160, A3061–A3065.

11. Y. Orikasa, T. Maeda, Y. Koyama, H. Murayama, K. Fukuda, H. Tanida, H. Arai, E. Matsubara, Y. Uchimoto, Z. Ogumi, *Chem. Mater.* **2013**, 25, 1032−1039.

12. Y. Orikasa, T. Maeda, T. Koyama, H. Murayama, K. Fukuda, H. Tanida, H. Arai, E. Matsubara, Y. Uchimoto, Z. Ogumi, *J. Am. Chem. Soc.* **2013**, 135, 5497−5500.

13. Y. Koyama , T. Uyama, Y. Orikasa, T. Naka, H. Komatsu, K. Shimoda, H. Murayama, K. Fukuda, H. Arai, E. Matsubara, Y. Uchimoto, and Z. Ogumi, *Chem. Mater.* **2017**, 29, 2855–2863.

14. K.-S. Park, P. Xiao, S.-Y. Kim, A. Dylla, Y.-M. Choi, G. Henkelman, K. J. Stevenson, J. B. Goodenough, *Chem. Mater.* **2012**, 24, 3212–3218.

15. G. Xu, K. Zhong, J.-M. Zhang, Z. Huang, *J. Appl. Phys.* **2014**, 116, 063703.

16. G. Xu, K. Zhong, J.-M. Zhang, Z. Huang, *Solid State Ionics* **2015**, 281, 1–5.

17. J. Xie, N. Imanishi, T. Zhang, A. Hirano, Y. Takeda, O. Yamamoto, *Electrochim. Acta* **2009**, 54, 4631–4637.

18. K. Tang, X. Yu, J. Sun, H. Li, X. Huang, *Electrochim. Acta* **2011**, 56, 4869–4875.

19. M. Köhler, F. Berkemeier, T. Gallasch, G. Schmitz, *J. Power Sources* **2013**, 236, 61–67.

20. C. J. Wen, B. A. Boukamp, R. A. Huggins, *J. Electrochem. Soc.* **1979**, 126, 2258–2266.

21. A. J. Bard, L. R. Faulkner, Electrochemical Methods: Fundamentals and Applications, 2nd ed., Wiley, New York, **2001**.

22. D. Y. W. Yu, C. Fietzek, W. Weydanz, K. Donoue, T. Inoue, H. Kurokawa, S. Fujitani, *J. Electrochem. Soc.* **2007**, 154, A253–A257.

23. G. Wang, G. Luo, Y. L. Soo, R. F. Sabirianov, H.-J. Lin, W.-N. Mei, F. Namavar, C. L. Cheung, *Phys. Chem. Chem. Phys.* **2011**, 13, 19517–9.

24. F. M. F. de GrootJ, *J. Electron Spectrosc. Relat. Phenom.* **1994**, 67, 529–622.

25. W.-S. Yoon, M. Balasubramanian, K. Y. Chung, X.-Q. Yang, J. McBreen, C. P. Grey, D. A. Fischer, *J.Am. Chem. Soc.* **2005**, 127, 17479–17487.

26. A. Augustsson, G. V. Zhuang, S. M. Butorin, J. M. Osorio-Guillen, C. L. Dong, R. Ahuja, C. L. Chang, P. N. Ross, J. Nordgren, J.-H. Guo, *J. Chem. Phys.* 2005, **123,** 184717.

27. S. Yang, D. Wang, G. Liang, Y. M. Yiu, J. Wang, L. Liu, X. Sun, T.-K. Sham, *Energy Environ. Sci.* **2012**, 5, 7007–7016.

28. D. Takamatsu, T. Nakatsutsumi, S. Mori, Y. Orikasa, M. Mogi, H. Yamashige, K. Sato, T. Fujimoto, Y. Takanashi, H. Murayama, M. Oishi, H. Tanida, T. Uruga, H. Arai, Y. Uchimoto, Z. Ogumi, *J. Phys. Chem. Lett.* **2011**, 2, 2511–2514.

29. T. Okumura, T. Nakatsutsumi, T. Ina, Y. Orikasa, H. Arai, T. Fukutsuka, Y. Iriyama, T. Uruga, H. Tanida, Y. Uchimoto, Z. Ogumi, *J. Mater. Chem.* **2011**, 21, 10051–10060.

30. H. Kageyama, K. Hayashi, K. Maeda, J. P. Attfield, Z. Hiroi, J. M. Rondinelli, K. R. Poeppelmeier, *Nat. Commun.* **2018**, 9, 772.

Chapter 6.

Design Principle for Metal/Metal Fluoride-ion Electrode Materials for High-energy Density Storages

Li-ion batteries is approaching to the physicochemical limit of the energy density, requiring new concepts for the electrochemical energy storage. All-solid-state fluoride-ion batteries, where a monovalent fluoride-ion is an anion charge carrier, offer an attractive option for the high energy density, but their reaction mechanism is not understood. Here we present Cu thin-film model cathode exhibits the discharge capacity of 670 mAh/g as well as the Coulombic efficiency of 91%. The two-phase transition between Cu and CuF_2 occurs during the electrochemical reaction and the phase boundary would be the origin of the contact loss for the capacity fade due to the repeating volume expansion and contraction. Cu_3Au alloy with the reduced lattice mismatch offers the fast phase transition kinetics along with the stability for cycling. Alloying opens up new possibilities for materials strategy.

6.1. Introduction

High energy density electrochemical energy storage is a key device for energy diversification to achieve a sustainable future[1, 2]. So far, Li-ion batteries, which are typical but reaching physicochemical limit, have been predominate in a market for 30 years[3], but other intercalation batteries such as Mg^{2+}, Ca^{2+}, Zn^{2+} are still in odyssey[4]. Although the multivalent ions could offer the high capacity with acceptable voltage, the strong electrostatic interactions between the diffusing multivalent cation and the anion lattice hinders the reversible application. For a game-changing technology, all-solid-state fluoride-ion batteries have the great potential to enable the high energy density as well as the high safety[5]. As a monovalent fluoride-ion is an anion charge carrier, the possibility of materials design based on the counter cation is infinity even restricted in simple metal or metal alloy. In general, the redox potential to produce fluorine gas from metal fluoride is higher than that in case of the oxygen lattice, indicating the reliable energy storage system along with the solid-state use.

All-solid-state fluoride-ion batteries have been reported in recent 7 years for metal/metal fluoride[6-14] and the oxide intercalation compounds[15-18]. The tysonite-type $La_{0.9}Ba_{0.1}F_{2.9}$ is commonly used as solid electrolyte and stable within a potential range in battery operation[19]. For metal/metal fluoride system, some combinations are used to evaluate their battery performance, but the reaction mechanism has been poorly understood.

Here we demonstrate the Cu/CuF_2 cathode offers the high capacity reaching the theoretical value and the electrochemical (de)fluorination proceeds via two-phase reaction. Alloying reduces the huge lattice mismatch between metal and metal fluoride to improve the battery performance that Cu_3Au exhibits the high rate capability as well as the long cycle life. Suppression of the strain energy within the phase boundary is a crucial strategy for materials design in all-solid-state fluoride-ion batteries.

6.2. Experimental

6.2.1. Battery preparation

The thin-film all-solid-state fluoride-ion battery cell was fabricated on LaF_3 solid electrolyte by RF sputtering method. The polycrystalline LaF_3 (xx%, Pier Optics) was used as the separator electrolyte as well as the substrate with the thickness of 0.5 mm.

The surface of the substrate to be the cathode side was mirror-polished and its roughness was evaluated by AFM images. The same surface was processed by the reverse sputtering with argon plasma and annealed for 1 h at 300°C in NF_3 gas atmosphere. The ionic conductivity of the solid electrolyte was xxx S/cm at 150°C. Afterwards, Cu and Pb thin-films were deposited on the substrate and used as the working and reference electrodes, respectively. Cu_3Au alloy thin-film electrode was prepared by the annealing at 300°C for 1 h after the deposition of Au onto Cu. The thickness of both electrodes was estimated by stylus profiler. The La metal could be produced from LaF_3 and was used as the counter electrode. For the current collectors, Pt and W was deposited on the side of the working and counter electrodes, respectively. These metal were selected due to the intact during the electrochemical measurements. All sputtering conditions are listed in. Finally, as-deposited Pb was fluorinated along with the production of La for the counter electrode to be the stable reference potential.

6.2.2. XRD measurements

The thin-film electrodes deposited on a synthetic silica glass substrate were characterized by XRD using Ultima IV (Rigaku) with Cu Ka radiation. The X-ray tube current and voltage were set to 40 mA and 40 kV, respectively. The data were taken in the range from $2\theta = 20°$ to 80° with the sample-stage rotation at xxx rpm.

6.2.3. Charge/discharge measurements

The battery assembly and the measurements were conducted in an inert atmosphere. The galvanostatic charge/discharge cycling was performed at various C-rates (1C = 843 mA/g) with the potential range of 0 to 1.25 V vs. Pb/PbF_2 at 150, 60, and 25°C using PARSTAT MC2000 (Princeton Applied Research). The specific weight was normalized by Cu. The amount of the reaction surface area on the counter electrode is a surplus in comparison with the working electrode, or Cu thin-film, not to be the limiting factor when investigating the cathode side.

6.2.4. XAS measurements

The samples were prepared by the electrochemical (de)fluorination at particular fluorine contents in CuF_x or $(Cu_3Au)_{1/3}F_x$ ($0 \leq x \leq 2$). They were transferred from an argon-filled glovebox to the analysis chamber using sealed containers without air exposure. Cu K-edge XANES measurements were undertaken at BL01B1 and BL37XU (SPring-8, Japan). The absorption spectra were collected in partial fluorescence mode using 19-elements SSD.

6.3. Results and Discussion

6.3.1. Battery performance of metal/metal fluoride

The thin-film model cell was fabricated with a reference electrode to have deep insight from electrochemical properties (**Figure 6.1a**). Galvanostatic charge/discharge curves depending on temperatures are shown in **Figure 6.1b**. At 25°C, the Cu cathode reacts with more than one fluoride-ion on the charge and then it releases about 0.7F per Cu atom on the discharge. With increasing temperature, the higher capacity as well as the lower polarization is exhibited. At 150°C, the highly reversible profile is observed as almost 1.75 fluoride-ions are reacted on the charge and the subsequent Coulombic efficiency achieves 91% at first cycle. The electrochemical reaction proceeds in a wide fluoride-ion compositional range according to the theoretical limitation of 2 fluoride-ions in Cu, or CuF_2. The average discharge potential of 0.66 V vs. Pb/PbF_2 is consistent with the theoretical value, which indicates the ideal electrochemical reaction takes place in this arrangement. Note that this is also hundreds of mV higher than that of previous reports[6, 12].

The delivered capacities remarkably exceed those of the conventional lithium-ion battery cathodes even at 25°C and are 3.5 times larger at 150°C. With an assumption of the configuration such as Cu/CuF_2 as a cathode and Li/LiF as an anode, over 3 V battery system would be realized (**Figure 6.1c**). The metal/metal fluoride batteries have the potential to enable high energy storage with appropriate electrodes combination.

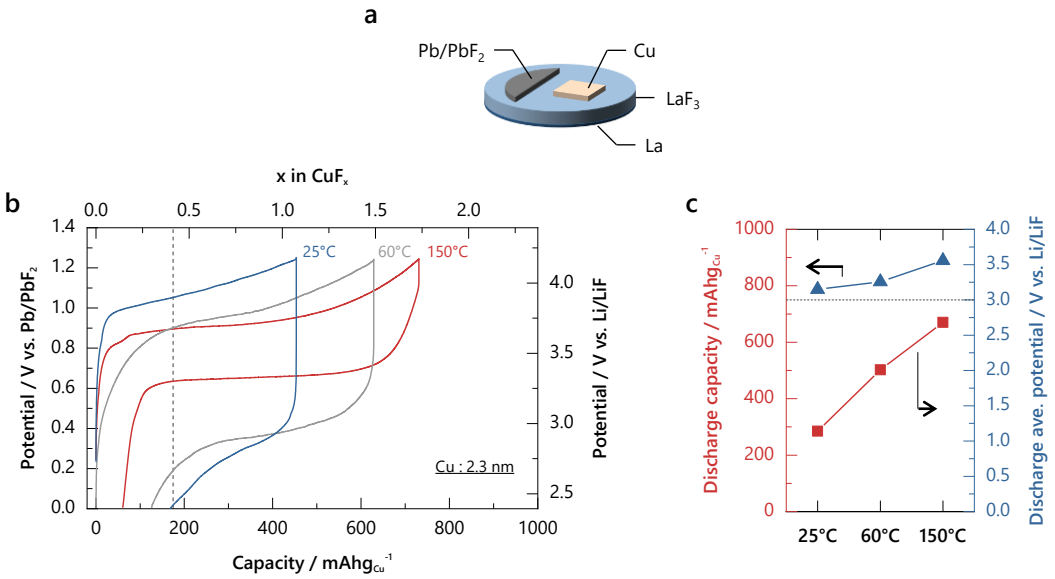

***Figure 6.1. Battery performance of the model system. a**, Schematic illustration for the battery configuration of the thin-film model cell. Cu and Pb thin-films are deposited on LaF_3 solid electrolyte substrate and used as the working and reference electrodes, respectively. La is produced by the self-forming reaction of LaF_3 solid electrolyte. **b**, Galvanostatic charge/discharge curves of the battery cycled at 150, 60, 25°C. The current density is 84.3 mA/g. The right axis indicates the potential based on Li/LiF. The capacity is calculated from the amount of Cu. A dashed line represents capacity for conventional lithium-ion battery cathodes. **c**, Discharge capacity and average potential at 150, 60, 25°C. Red rectangles and blue triangles are attributed to left and right axes, respectively. A dashed line represents 3.0 V vs. Li/LiF.*

Figure 6.2 shows the cycling characteristics. During 20 cycles, the capacity at 150°C falls down from 670 to 254 mAh/g, which is less than half of the initial cycle, whereas the reversible behavior was found at lower temperatures. The cycled capacity at 60°C exceeds the result at 150°C and the value is 344 mAh/g, corresponding to 68% of the initial cycle. The cyclability is further improved at 25°C, although the absolute capacity is always low for cycling.

No major changes was found in the charge/discharge curves and the average potential on the charge/discharge is constant at each temperature. The electrode/electrolyte interface would remain intact and involve no side reaction. Metal fluoride solid electrolyte is stable until fluorine gas produces and/or fluorination of current collectors occurs. It has been reported that $La_{0.9}Ba_{0.1}F_{2.9}$, similar to LaF_3, has wide oxidation electrochemical potential window up to 6 V vs. Li/LiF.[19] This is uncommon compared to Li-ion batteries. In a Li-ion battery employing liquid electrolyte, degradation of a cathode active material occurs in contact with typical organic electrolyte[20] without coating[21] or additives[22]. In an all-solid-state battery with sulfide electrolyte, as the interphase formation as well as the contact loss is generated upon cycling, the decomposition products from the former could be the resistive layer, which raises the cell impedance and leads to the voltage decay[23, 24].

The capacity fade without voltage decay indicates the contact loss between an electrode and electrolyte mainly occurs in Cu cathode material. The lattice volume expiation from Cu to CuF_2 is quite large 46.8%. This could be the origin of the degradation in metal/metal fluoride batteries as reported previously.[6]

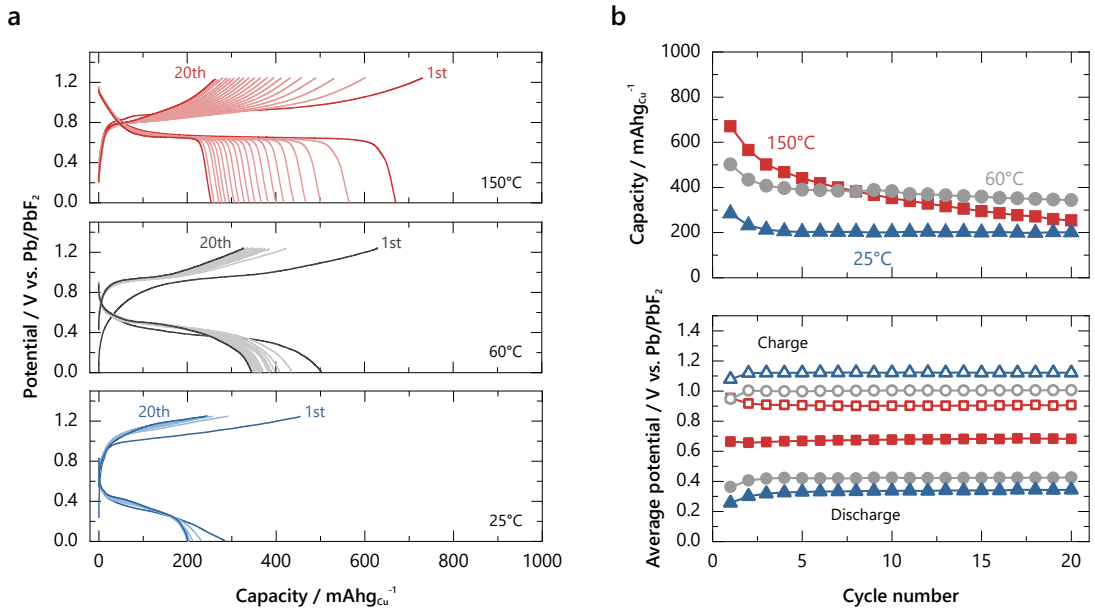

Figure 6.2. Cycle behavior depending on temperatures. ***a****, Galvanostatic charge/discharge curves during 20 cycles at 150 (top), 60 (middle), and 25°C (bottom). Dark color represents the 1st and the 20th cycle for each graph.* ***b****, Discharge capacity (top) and average charge/discharge potential (bottom) during 20 cycles. Red, gray, and blue represent the data at 150, 60, 25°C, respectively. Open and filled symbols indicate charge and discharge, respectively.*

6.3.2. Electrochemical (de)fluorination processes

The electrochemical reaction of Cu/CuF_2 accompanying with phase transition was carefully investigated. **Figure 6.3a** shows X-ray absorption near edge structure (XANES) spectra on the charge/discharge. The XANES spectrum of the prepared Cu electrode deposited by RF sputtering overlaps with that of Cu foil for the reference spectrum. On the charge, or the fluorination process from Cu to $CuF_{1.7}$, the spectra changes towards CuF_2 reference spectrum having an isosbestic point at 8990 eV. The opposite trend is observed on the discharge that the spectra changes from CuF_2 to Cu having the isosbestic point at the same position as the charge. No additional peaks or exceptional changes are detectable.

According to the XANES spectra having the isosbestic point, linear combination fitting with two spectra, Cu and CuF_2, was conducted as shown in **Figure 6.3b**. On the charge, the fraction of Cu decreases with increasing that of CuF_2 along the line that fluorination of Cu generates only CuF_2. The opposite and reversible trend is observed on the

discharge. This demonstrates the electrochemical (de)fluorination of Cu/CuF_2 proceeds via two-phase reaction. The good consistency between the actual fraction change and the ideal phase transition line suggests that no undesirable side reactions occur and no intermediate phases such as CuF form.

The phase boundary movement accompanying with the nucleation and growth is strongly correlated with phase transition kinetics. Kolmogorov-Johnson-Mehl-Avrami (KJMA) analysis has been applied to the electrochemical reaction to predict the phase transition mechanism[25, 26]. With an assumption of two-phase transition, volume fraction of a new phase, V, as a function of t is

$$V = 1 - \exp(-kt^n) \quad (1)$$

where k is the rate constant of phase transition and n is the Avrami exponent. The equation (1) can be rearranged as follows:

$$\ln\ln[1/(1-V)] = n\ln t + \ln k. \quad (2)$$

The slope of $\ln\ln[1/(1-V)]$ against $\ln t$ plot gives the Avrami exponent, which is consisted of three components:

$$n = a + bc \quad (3)$$

where a is the nucleation index ($a = 0$ for nucleation rate zero, $0 < a < 1$ for decreasing nucleation rates, $a = 1$ for constant nucleation, and $a > 1$ for increasing nucleation rates), b is the dimension of growth ($b = 1, 2, 3$ for 1D, 2D, 3D growth, respectively), and c is a growth index dependent on the rate-determining step of the transformation ($c = 1$ for phase-boundary-controlled growth, and $c = 1/2$ for diffusion-controlled growth).

In the case of the Cu/CuF_2 reaction, the potential-step chronoamperometry was used to induce the phase transition for KJMA analysis (**Figure 6.3c**). The current shows the momentary increase for 2 h and the gradual decline afterwards, corresponding to the nucleation and growth processes. Converting the current to volume fraction of a new phase, the Avrami plot was obtained (**Figure 6.3d**). The linear fitting was conducted at the nucleation process, except for the electric double layer capacity at an early stage of the reaction by potential-step chronoamperometry. The obtained Avrami exponent is $n = 1.15$. Following the above scheme, the Avrami exponent could be interpreted in (i) diffusion-controlled two-dimensional phase transition ($a = 0.15$, $b = 2$, and $c = 1/2$)

or (ii) phase-boundary-controlled one-dimensional phase transition ($a = 0.15$, $b = 2$, and $c = 1/2$). The nucleation index, a, governs the time dependence of the number of nuclei per unit volume of untransformed material, N, as a function of time[27, 28]:

$$N \propto t^a. \tag{3}$$

In both cases, $a = 0.15$ represents the decreasing nucleation rate, which is in good agreement with the nucleation behavior. For the parameter c, the diffusion-controlled, or parabolic, growth ($c = 1/2$) would be kinetically unfavorable due to the high strain energy produced by the large lattice volume change 46.8%. Consequently, the second model of the phase-boundary-controlled one-dimensional phase transition should be the plausible interpretation.

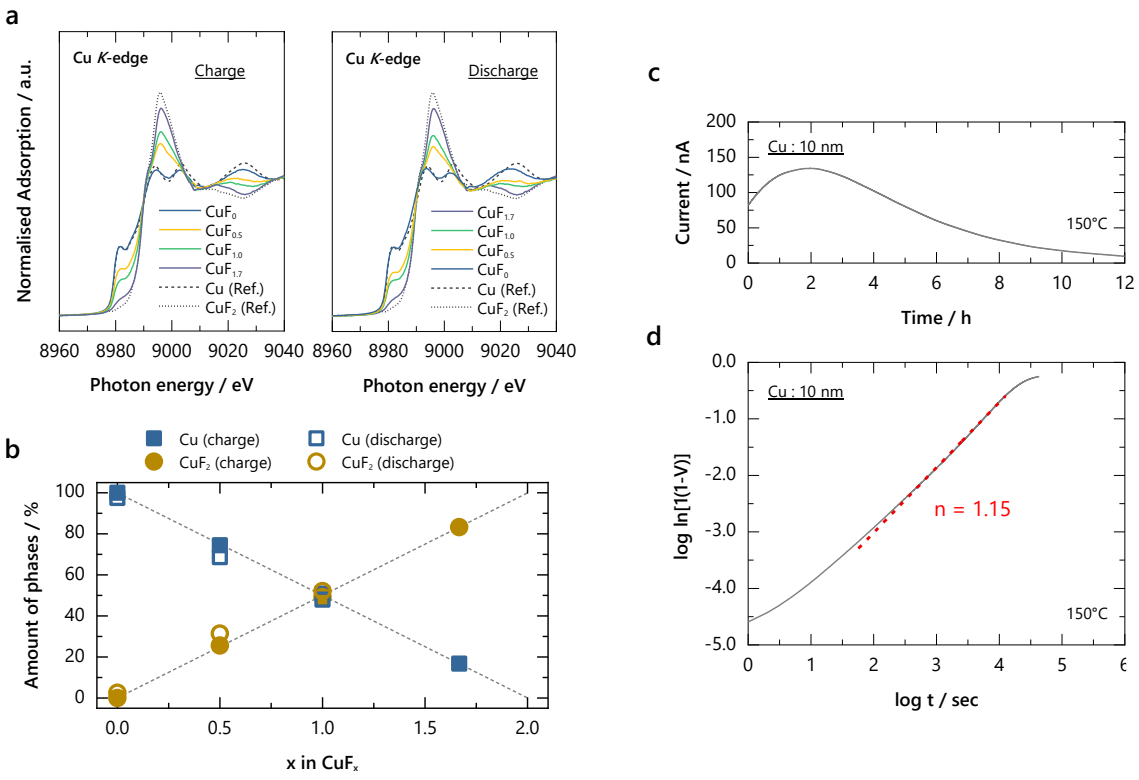

Figure 6.3. Phase transition mechanism on electrochemical (de)fluorination. ***a****, XANES spectra on the charge (left) and discharge (right). Dotted and dashed lines represent Cu and* CuF_2 *reference spectra, respectively.* ***b****, Amount of Cu and* CuF_2 *phases during the charge and discharge. Dotted lines are a guide to the eye.* ***c****, Current change after the potential step with 0.68 to 0.66 V vs. Pb/*PbF_2 *at 150°C.* ***d****, Avrami plots converted from the potential step treatment. The slope of the line is equal to the Avrami exponent. A dashed red line represents the linear fitted result for the Avrami exponent n.*

6.3.3. Alloying effect to metal/metal fluoride battery

The huge lattice mismatch hinders the fast phase transition as well as the reversible expansion and contraction within the material. Alloying appropriate metal with Cu could offer the small lattice volume change. Cu_3Au alloy was prepared and confirmed to have the larger lattice volume due to the larger ionic radius of Au (**Figure 6.4a,b**). Considering the lattice volume change between Cu or Cu_3Au and CuF_2, which are 46.8% and 27.8%, respectively, the alloying could reduce 19%.

The Cu_3Au cathode also successfully cycled and the phase transition mechanism was studied by XANES (**Figure 6.5**). The XANES spectrum of Cu_3Au slightly shifts lower energy compared to that of Cu[29] (**Figure 6.5b**). During the charge/discharge, the intermediate fluorination of Cu_3Au spectra changes between Cu_3Au and CuF_2 reference spectrum having an isosbestic point in the same manner as Cu, although the value of the isosbestic point is a bit higher 8991 eV (**Figure 6.5d**). The results of linear combination fitting with two spectra, Cu_3Au and CuF_2 demonstrate the two-phase nature of Cu_3Au during the electrochemical (de)fluorination (**Figure 6.5e**). Note that the Cu_3Au spectra of before and after cycle completely overlapping suggests Cu_3Au is reproducible even after the phase transition to CuF_2 and Au.

The charge/discharge properties before and after alloying were investigated. While the Cu cathode delivers 365 mAh/g at C/5, which is less than half that at C/50, the Cu_3Au still maintains the capacity of 504 mAh/g at C/5 as shown in **Figure 6.4c**. The alloying to be the small lattice strain enhances the rate capability summarizing in **Figure 6.4d**. The identical charge/discharge potential at low rate indicates the same redox active element of Cu being responsible for the charge transfer. The cycle deterioration is suppressed after alloying that the capacity of Cu_3Au at 20th cycle is almost double in comparison with that of Cu (**Figure 6.4d**). The reduction of the lattice mismatch by alloying is effective for the high rate performance as well as the long cycle life due to the smooth phase transition.

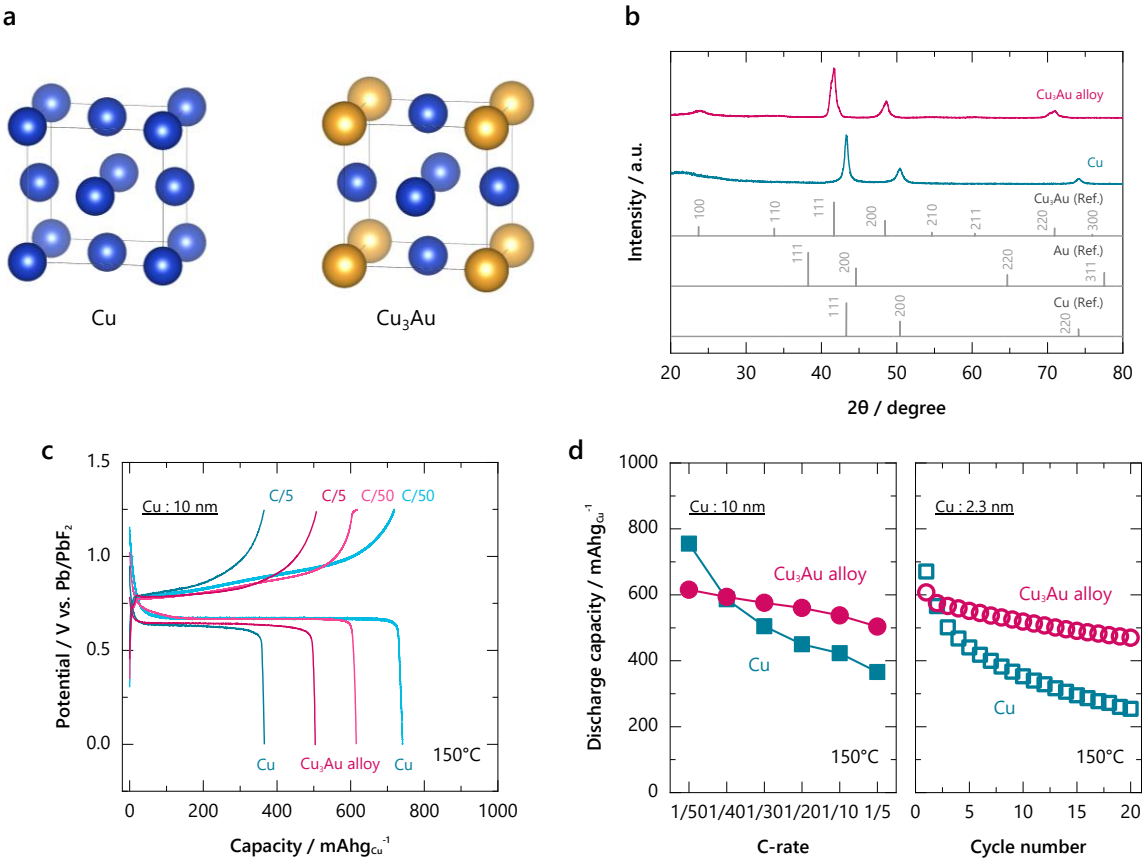

Figure 6.4. Controlling lattice volume change by alloying. ***a****, Crystal structure of Cu (left) and Cu3Au (right). Blue and gold represent Cu and Au, respectively.* ***b****, XRD patterns of Cu and Cu3Au.* ***c****, Charge/discharge curves of Cu and Cu3Au at 150°C.* ***d****, Rate performance (left) and cyclability (right) of Cu and Cu3Au at 150°C.*

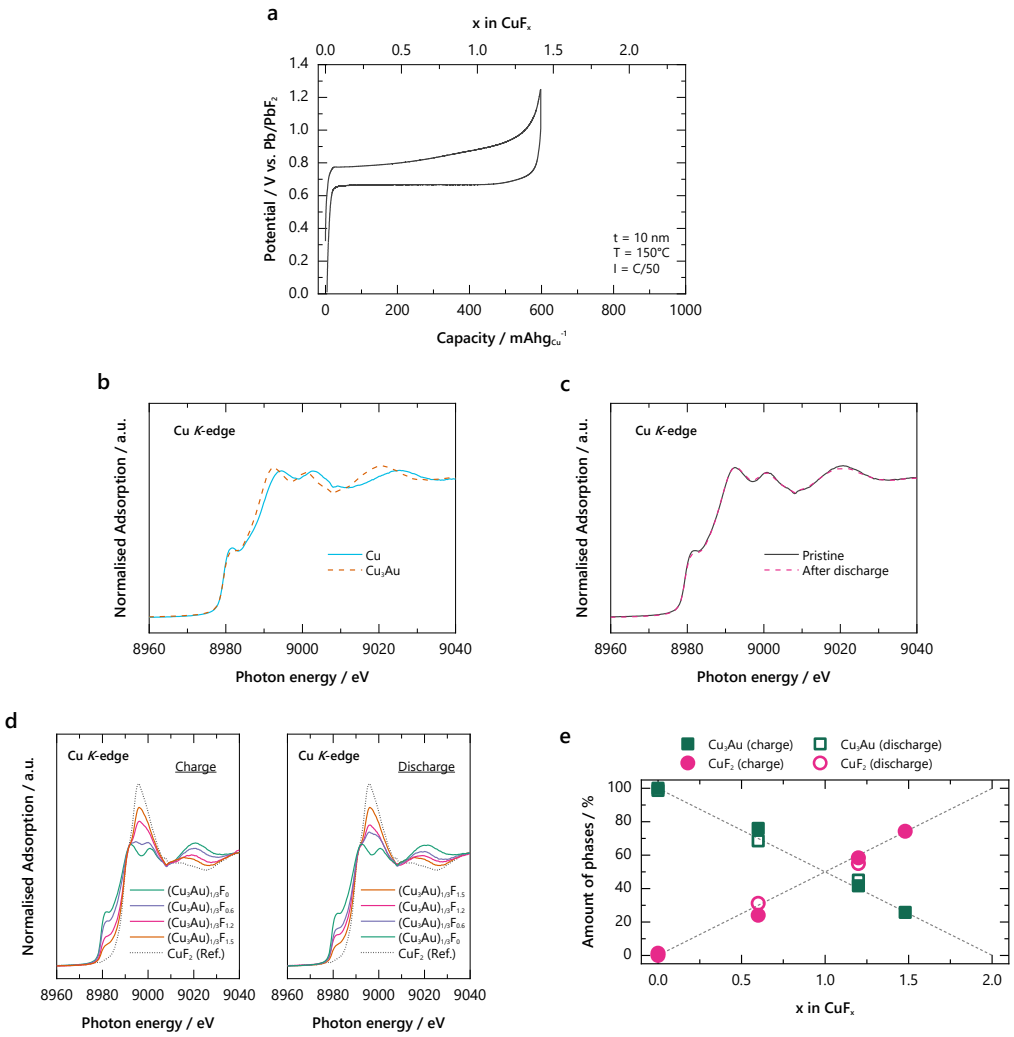

Figure 6.5. Charge compensation mechanism of Cu-Au alloy. ***a****, Charge/discharge curves of Cu-Au alloy electrode for XAS measurement.* ***b****, XAS spectra of as-deposited Cu and* Cu_3Au*.* ***c****, XAS spectra of before and after cycle.* ***d****, XAS spectra on the charge (left) and on the discharge (right). Dashed lines represent* CuF_2 *reference spectra.* ***e****, Amount of* Cu_3Au *and* CuF_2 *phases during the charge and discharge. Dotted lines are a guide to the eye.*

The phase transition kinetics was investigated quantitatively. With an assumption of the one-dimensional phase transition, a ratio of charge at certain time and total time is equivalent to a ratio of a new phase and total thickness of an electrode[30, 31]:

$$\frac{Q_{t'}}{Q_\infty} = \frac{l-(l-\xi)}{l} \tag{4}$$

where $Q_{t'}$ is the charge at time t, Q_∞ is the total charge to finish the phase transition,

ξ is the thickness of a new phase, and l is the total thickness of the end of the phase transition. Thus, ξ is presented as a function of t. According to the Wagner model for diffusion in a binary system containing a phase boundary[32], phase boundaries move linearly with $t'^{1/2}$:

$$\xi = 2\gamma(Dt')^{1/2} = k't'^{1/2} \quad (4)$$

where γ is the dimensionless parameter, D is diffusion co-efficient for a new phase, and k' is phase boundary rate constant.

The potential-step chronoamperometry was used to induce the phase transition in the Cu or Cu_3Au cathode (**Figure 6.6a**). The Cu_3Au cathode shows the pronounced nucleation and growth behavior at high current and the fast decline to settling down to zero current compared to Cu. The current is converted to ξ (**Figure 6.6b**). The linear fitting was conducted at the nucleation process, except for the electric double layer capacity at an early stage of the reaction by potential-step chronoamperometry. The obtained phase boundary rate constant is 1.1×10^{-9} cm $s^{1/2}$ for Cu_3Au, which is three times higher than 3.7×10^{-10} cm $s^{1/2}$ for Cu. Although the phase transition kinetics is enhanced by alloying, the quantitative value is still 10^4 times lower than that of $LiFePO_4$[33], which is the two-phase cathode material in lithium-ion batteries.

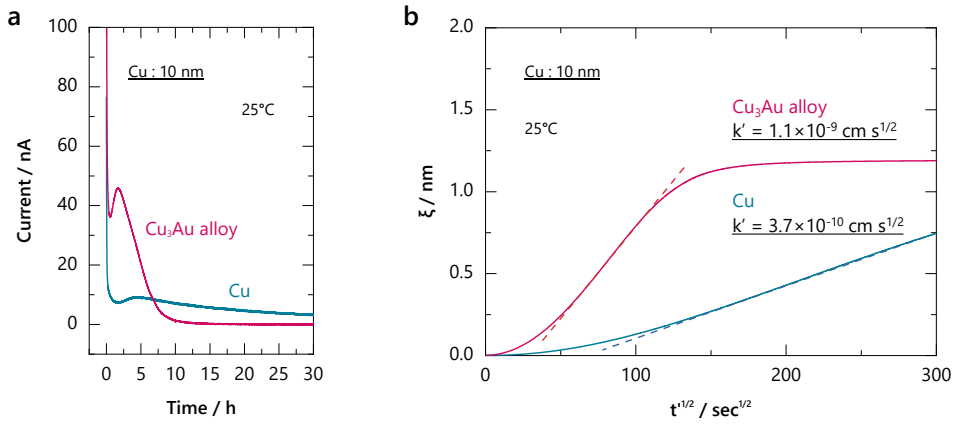

Figure 6.6. Phase boundary movement of two-phase materials. ***a****, Chronoamperometry with the potential step from 0.76 to 0 V at 25°C after charged to 1.25 V vs. Pb/PbF_2 at 150°C.* ***b****, Distance for phase transition ξ vs. $t'^{1/2}$ plots based on Wagner model. The phase transition rate constant k' is 3.7 $\times10^{-10}$ cm $s^{1/2}$ for Cu and 1.1 $\times10^{-9}$ cm $s^{1/2}$ for Cu_3Au.*

6.4. Conclusion

The thin-film Cu cathode was fabricated as a model metal electrode in fluoride-ion battery system. As the polarization decreases with increasing temperature, the discharge capacity of 670 mAh/g is delivered with the average potential of 0.66 V vs. Pb/PbF_2 at 150°C. With an assumption of 3 V battery configuration with an appropriate anode, the energy density would achieve 2,000 Wh/kg. The electrochemical reaction of Cu/CuF_2 proceeds with separation into two phases, Cu and CuF_2. The one-dimensional phase transition under the limitation of phase-boundary-controlled movement is predicted by KJMA analysis. The huge lattice mismatch between metal/metal fluorides should be improved for better battery performance. Metal alloys offer the tremendous possibility to design materials to be reduced the lattice strain at phase boundary. Cu_3Au alloy was prepared for one of the candidate with 19% lower volume change and successfully worked as a fluoride-ion battery electrode. The two-phase reaction between Cu_3Au and CuF_2 is also observed and highly reversible. Cu_3Au alloy provides the high rate performance as well as the long cycle life compared to Cu metal. Although the alloying is effective to enhance the battery performance, the phase transition rate constant calculated from the Wagner model is still four orders of magnitude lower than that of $LiFePO_4$ that is the commercialized two-phase material in Li-ion batteries. Our findings have implication for battery design and utilization, which could be realized by such as materials informatics.

References

1. Grey, C. P.; Tarascon, J. M., Sustainability and in situ monitoring in battery development. *Nat. Mater.* **2017,** *16* (1), 45-56.

2. Chu, S.; Cui, Y.; Liu, N., The path towards sustainable energy. *Nat. Mater.* **2017,** *16* (1), 16-22.

3. Janek, J.; Zeier, W. G., A solid future for battery development. *Nat. Energy* **2016,** *1*.

4. Canepa, P.; Gautam, G. S.; Hannah, D. C.; Malik, R.; Liu, M.; Gallagher, K. G.; Persson, K. A.; Ceder, G., Odyssey of Multivalent Cathode Materials: Open Questions and Future Challenges. *Chem. Rev.* **2017,** *117* (5), 4287-4341.

5. Gschwind, F.; Rodriguez-Garcia, G.; Sandbeck, D. J. S.; Gross, A.; Weil, M.; Fichtner, M.; Hormann, N., Fluoride ion batteries: Theoretical performance, safety, toxicity, and a combinatorial screening of new electrodes. *J. Fluorine Chem.* **2016,** *182*, 76-90.

6. Reddy, M. A.; Fichtner, M., Batteries based on fluoride shuttle. *J. Mater. Chem.* **2011,** *21* (43),

17059-17062.

7. Rongeat, C.; Reddy, M. A.; Witter, R.; Fichtner, M., Nanostructured Fluorite-Type Fluorides As Electrolytes for Fluoride Ion Batteries. *J. Phys. Chem. C* **2013,** *117* (10), 4943-4950.

8. Rongeat, C.; Reddy, M. A.; Diemant, T.; Behm, R. J.; Fichtner, M., Development of new anode composite materials for fluoride ion batteries. *J. Mater. Chem. A* **2014,** *2* (48), 20861-20872.

9. Grenier, A.; Gutierrez, A. G. P.; Groult, H.; Dambournet, D., Modified coin cells to evaluate the electrochemical properties of solid-state fluoride-ion batteries at 150 degree C. *J. Fluorine Chem.* **2016,** *191*, 23-28.

10. Fawey, M. H.; Chakravadhanula, V. S. K.; Reddy, M. A.; Rongeat, C.; Scherer, T.; Hahn, H.; Fichtner, M.; Kubel, C., In Situ TEM Studies of Micron-sized All-solid-state Fluoride Ion Batteries: Preparation, Prospects, and Challenges. *Microsc. Res. Tech.* **2016,** *79* (7), 615-624.

11. Grenier, A.; Porras-Gutierrez, A. G.; Groult, H.; Beyer, K. A.; Borkiewicz, O. J.; Chapman, K. W.; Dambournet, D., Electrochemical reactions in fluoride-ion batteries: mechanistic insights from pair distribution function analysis. *J. Mater. Chem. A* **2017,** *5* (30), 15700-15705.

12. Thieu, D. T.; Hammad, M.; Bhatia, H.; Diemant, T.; Chakravadhanula, V. S. K.; Behm, R. J.; Kubel, C.; Fichtner, M., CuF_2 as Reversible Cathode for Fluoride Ion Batteries. *Adv. Funct. Mater.* **2017,** *27* (31).

13. Zhang, L.; Reddy, M. A.; Gao, P.; Diemant, T.; Behm, R. J.; Fichtner, M., Study of all solid-state rechargeable fluoride ion batteries based on thin-film electrolyte. *J. Solid State Electrochem.* **2017,** *21* (5), 1243-1251.

14. Zhang, L.; Reddy, M. A.; Fichtner, M., Electrochemical performance of all solid-state fluoride-ion batteries based on thin-film electrolyte using alternative conductive additives and anodes. *J. Solid State Electrochem.* **2018,** *22* (4), 997-1006.

15. Clemens, O.; Rongeat, C.; Reddy, M. A.; Giehr, A.; Fichtner, M.; Hahn, H., Electrochemical fluorination of perovskite type $BaFeO_{2.5}$. *Dalton Trans.* **2014,** *43* (42), 15771-15778.

16. Nowroozi, M. A.; Wissel, K.; Rohrer, J.; Munnangi, A. R.; Clemens, O., $LaSrMnO_4$: Reversible electrochemical intercalation of fluoride ions in the context of fluoride ion batteries. *Chem. Mater.* **2017,** *29* (8), 3441-3453.

17. Nowroozi, M. A.; Ivlev, S.; Rohrer, J.; Clemens, O., La_2CoO_4: A new intercalation based cathode material for fluoride ion batteries with improved cycling stability. *J. Mater. Chem. A* **2018,** *6* (11), 4658-4669.

18. Nowroozi, M. A.; de Laune, B.; Clemens, O., Reversible Electrochemical Intercalation and Deintercalation of Fluoride Ions into Host Lattices with Schafarzikite-Type Structure. *Chemistryopen* **2018,** *7* (8), 617-623.

19. Grenier, A.; Porras-Gutierrez, A. G.; Body, M.; Legein, C.; Chretien, F.; Raymundo-Pinero, E.; Dolle, M.; Groult, H.; Dambournet, D., Solid Fluoride Electrolytes and Their Composite with Carbon: Issues and Challenges for Rechargeable Solid State Fluoride-Ion Batteries. *J. Phys. Chem. C* **2017,** *121* (45), 24962-24970.

20. Takamatsu, D.; Koyama, Y.; Orikasa, Y.; Mori, S.; Nakatsutsumi, T.; Hirano, T.; Tanida, H.;

Arai, H.; Uchimoto, Y.; Ogumi, Z., First In Situ Observation of the $LiCoO_2$ Electrode/Electrolyte Interface by Total-Reflection X-ray Absorption Spectroscopy. *Angew Chem Int Edit* **2012,** *51* (46), 11597-11601.

21. Orikasa, Y.; Takamatsu, D.; Yamamoto, K.; Koyama, Y.; Mori, S.; Masese, T.; Mori, T.; Minato, T.; Tanida, H.; Uruga, T.; Ogumi, Z.; Uchimoto, Y., Origin of Surface Coating Effect for MgO on $LiCoO_2$ to Improve the Interfacial Reaction between Electrode and Electrolyte. *Adv Mater Interfaces* **2014,** *1* (9).

22. Takamatsu, D.; Orikasa, Y.; Mori, S.; Nakatsutsumi, T.; Yamamoto, K.; Koyama, Y.; Minato, T.; Hirano, T.; Tanida, H.; Arai, H.; Uchimoto, Y.; Ogumi, Z., Effect of an Electrolyte Additive of Vinylene Carbonate on the Electronic Structure at the Surface of a Lithium Cobalt Oxide Electrode under Battery Operating Conditions. *J. Phys. Chem. C* **2015,** *119* (18), 9791-9797.

23. Koerver, R.; Aygun, I.; Leichtweiss, T.; Dietrich, C.; Zhang, W. B.; Binder, J. O.; Hartmann, P.; Zeier, W. G.; Janek, J., Capacity Fade in Solid-State Batteries: Interphase Formation and Chemomechanical Processes in Nickel-Rich Layered Oxide Cathodes and Lithium Thiophosphate Solid Electrolytes. *Chem. Mater.* **2017,** *29* (13), 5574-5582.

24. Koerver, R.; Walther, F.; Aygun, I.; Sann, J.; Dietrich, C.; Zeier, W. G.; Janek, J., Redox-active cathode interphases in solid-state batteries. *J. Mater. Chem. A* **2017,** *5* (43), 22750-22760.

25. Allen, J. L.; Jow, T. R.; Wolfenstine, J., Kinetic study of the electrochemical FePO4 to LiFePO4 phase transition. *Chem. Mater.* **2007,** *19* (8), 2108-2111.

26. Orikasa, Y.; Maeda, T.; Koyama, Y.; Minato, T.; Murayama, H.; Fukuda, K.; Tanida, H.; Arai, H.; Matsubara, E.; Uchimoto, Y.; Ogumi, Z., Phase Transition Analysis between LiFePO4 and FePO4 by In-Situ Time-Resolved X-ray Absorption and X-ray Diffraction. *J. Electrochem. Soc.* **2013,** *160* (5), A3061-A3065.

27. Ranganathan, S.; Vonheimendahl, M., The Three Activation Energies with Isothermal Transformations: Applications to Metallic Glasses. *J Mater Sci* **1981,** *16* (9), 2401-2404.

28. Ruitenberg, G.; Petford-Long, A. K.; Doole, R. C., Determination of the Isothermal Nucleation and Growth Parameters for the Crystallization of Thin $Ge_2Sb_2Te_5$ Films. *J. Appl. Phys.* **2002,** *92* (6), 3116-3123.

29. Kuhn, M.; Sham, T. K., Charge Redistribution and Electronic Behavior in a Series of Au-Cu Alloys. *Phys. Rev. B* **1994,** *49* (3), 1647-1661.

30. Levi, M. D.; Markevich, E.; Aurbach, D., Comparison between Cottrell diffusion and moving boundary models for determination of the chemical diffusion coefficients in ion-insertion electrodes. *Electrochim. Acta* **2005,** *51* (1), 98-110.

31. Levi, M. D.; Aurbach, D., The application of electroanalytical methods to the analysis of phase transitions during intercalation of ions into electrodes. *J. Solid State Electrochem.* **2007,** *11* (8), 1031-1042.

32. Funabiki, A.; Inaba, M.; Abe, T.; Ogumi, Z., Stage transformation of lithium-graphite intercalation compounds caused by electrochemical lithium intercalation. *J. Electrochem. Soc.* **1999,** *146* (7), 2443-2448.

33. Hong, J.; Wang, C. S.; Kasavajjula, U., Kinetic behavior of LiFeMgPO4 cathode material for

Li-ion batteries. *J. Power Sources* **2006,** *162* (2), 1289-1296.

Chapter 7.
Interfacial stability of phosphate-NASICON solid electrolytes in Ni-rich NCM cathode-based solid-state batteries

A non-degrading, low-impedance interface between a solid electrolyte and cathode active materials remains a key challenge for the development of functional all-solid-state batteries (ASSB). The widely employed thiophosphate-based solid electrolytes are not stable towards oxidation and suffer from a growing interface resistance and thus rapid capacity fading in a solid-state battery. In contrast, NASICON-type materials such as $Li_{1+x}Al_xTi_{2-x}(PO_4)_3$ and $Li_{1+x}Al_xGe_{2-x}(PO_4)_3$ are stable at high potentials, but their mechanical rigidity and high grain boundary resistance is thought to impede their application in bulk-type solid-state batteries. In this work, we present a comparative study of a $LiNi_{0.8}Co_{0.1}Mn_{0.1}O_2$ (NCM-811) cathode composite employing either β–Li_3PS_4 (LPS) or $Li_{1.5}Al_{0.5}Ti_{1.5}(PO_4)_3$ (LATP) as a solid electrolyte. LPS is employed as a separator in both cases to assemble a functional ASSB. In order to avoid high temperature processing of LATP, along with subsequent detrimental interfacial reactions with NCM materials, the solid-state batteries are constructed and operated in a hot-press setup at 150 °C. The cathode interfaces are investigated using *in-situ* electrochemical impedance spectroscopy and X-ray photoelectron spectroscopy, which reveals that the incremental interface resistance is extremely suppressed and the chemical state is unchanged during cycling when employed with LATP. The cell using LATP is reversibly charged and discharged for multiple cycles and outperforms a comparable cell serving a thiophosphate composite electrode. The results indicate that LATP represents an excellent candidate to overcome interfacial challenges in bulk-type solid-state batteries.

7.1. Introduction

The ongoing push for electrification of transport and the increasing amount of portable electronic devices drives the research for safer energy storage technologies. Lithium ion batteries (LIBs) are expected to serve in future mass-market generations of electric vehicles and thus have to be prepared for contingencies. Safety concerns arise particularly in the use of organic, mostly toxic liquid electrolytes that, in case of a collision, may leak, catch fire or even explode. In this regard, all-solid-state batteries (ASSBs) appear to represent a safer alternative to conventional LIBs.[1, 2] In ASSBs, the liquid-soaked separator membrane is replaced by a ceramic or glassy solid electrolyte (SE). It is now well accepted that ASSBs can only be competitive as a mass product once they offer at least the same performance and lifetime as LIBs with liquid electrolyte. During the development of LIBs within the last 30 years it was found that the liquid electrolyte allows stable and reversible operation due to solid electrolyte interface (SEI) formation at the graphite anode and sufficient interface stability at the cathode.[3, 4] Due to extensive research efforts, our knowledge of LIBs interfaces and their degradation is today quite detailed.

Within the recent years of ASSB research, several solid electrolytes have been reported that offer comparable lithium ion conductivity compared to their liquid counterparts.[5-8] Especially glass ceramic electrolytes in the Li_2S–P_2S_5 system and related systems exhibit high lithium ion conductivity.[9-13] Moreover, thiophosphate electrolytes, such as Li_3PS_4, $Li_7P_3S_{11}$, Li_6PSX or $Li_{10}GeP_2S_{12}$ offer favorable mechanical properties,[14-16] which allow an easy preparation and processing by cold pressing.[17] Unfortunately, the thermodynamic stability of the thiophosphate SE is very limited. Mo and co-workers recently calculated the electrochemical stability window of several solid electrolytes and reported the thiophosphate has very narrow stability window.[18, 19] The reactivity between lithium metal and thiophosphate SE is well understood and has been reported multiple times.[20, 21] The oxidative degradation at the cathode side represents an additional factor contributing to the capacity fading of solid-state batteries.[22-30] In particular, for application of high-capacity nickel-rich layered oxides or high-voltage cathode materials, the electrochemical stability of thiophosphate electrolytes towards high potentials is insufficient.[24, 27] Hence, it is challenging to address all requirements using a single solid electrolyte, so that a combination of multiple materials may be required for superior functionalities in the solid-state battery.

When moving away from sulfide-based electrolytes, the crystalline NASICON-type materials $Li_{1+x}Al_xGe_{2-x}(PO_4)_3$ and $Li_{1+x}Al_xTi_{2-x}(PO_4)_3$ represent promising alternatives to avoid the strong oxidative degradation during battery charging.[10, 19] For instance, it has been reported that $Li_{1.5}Al_{0.5}Ge_{1.5}(PO_4)_3$ is stable up to 6 V vs Li/Li^+.[31] Further, NASICON-type materials are not only oxidatively but also chemically stable when exposed to air or moisture,[32, 33] which is a huge benefit over thiophosphate compounds producing hydrogen sulfide gas.[34] NASICONs offer an acceptable lithium ion conductivity of 10^{-4} S/cm and the bulk conductivity can be increased up to 10^{-3} S/cm at room temperature by elemental substitution.[35-38] An inherent problem of phosphate SE is their huge grain boundary resistance and their mechanical rigidity.[39-41] In order to reach high ionic conductivity of polycrystalline ceramics, samples have to be prepared with very high density to reduce grain boundaries, which is usually only achieved by compressive sintering at above 900 °C.[42] With respect to battery fabrication, such high temperature sintering will induce unwanted side reactions with the other battery components, in particular with the cathode active materials.[43, 44] So far, reports of functional bulk solid-state batteries employing NASICON-type materials as SE is limited. Because of the required heat treatment, electrodes are mainly deposited as a thin film[45] on sintered SE pellets,[46] rather than as a thick composite electrode with high areal capacity as usually reported for sulfide-based batteries.[25] Another option to circumvent the high grain boundary resistance is the application as quasi-all-solid-state electrolyte in combination with either a conventional liquid electrolyte [47-49], an ionic liquid or polymers[50, 51]. However, introduction of liquids or hybrid concepts reverse the benefits of an all-solid-state approach and adds new interfaces that can possibly lead to additional degradation effects.[52]

Due to the remaining interfacial challenges of degrading interfaces in sulfide electrolytes as well as the interface resistances using phosphate electrolytes, we present a comparative study of ASSB using $LiNi_{0.8}Co_{0.1}Mn_{0.1}O_2$ (NCM-811) as a cathode material in combination with β–Li_3PS_4 (LPS) or $Li_{1.5}Al_{0.5}Ti_{1.5}(PO_4)_3$ (LATP) at the cathode interface. The batteries are prepared by cold pressing and the LATP/NCM-811 composite is assembled with a LPS separator to form a bilayer solid-electrolyte (**Figure 7.1**). By preparing the cells in a hot-press setup, the battery configuration is heated up to 150 °C, allowing to employ LATP in a bulk-type solid-state battery without a sintering step of the full cell. Our experiments show that despite the comparably lower ionic conductivity of LATP, the investigated cells show a higher capacity retention and thus better interfacial stability. The interfacial stability is investigated by the means of

electrochemical impedance spectroscopy (EIS) during cycling. From the interpretation of the impedance data, we derive the cathode interfacial resistance for both cell architectures and find that the interface between NCM-811 and LATP is more stable than in the case of LPS. The interphase formation was further investigated using X-ray photoelectron spectroscopy (XPS), which confirmed that the chemical state of the cathode components remains nearly unchanged when LATP is used for the electrode composite. In case of the thiophosphate, the previously observed oxidative degradation is even more pronounced when the solid-state battery is operated at elevated temperatures. Our results clearly encourage further investigation of the application of phosphate-based electrolytes to avoid interface degradation at the positive electrode. This work indicates that LATP can serve as an excellent component in a cathode composite, whether it is as a bulk solid electrolyte or rather a protective coating layer to shield the cathode active material from the solid electrolyte.

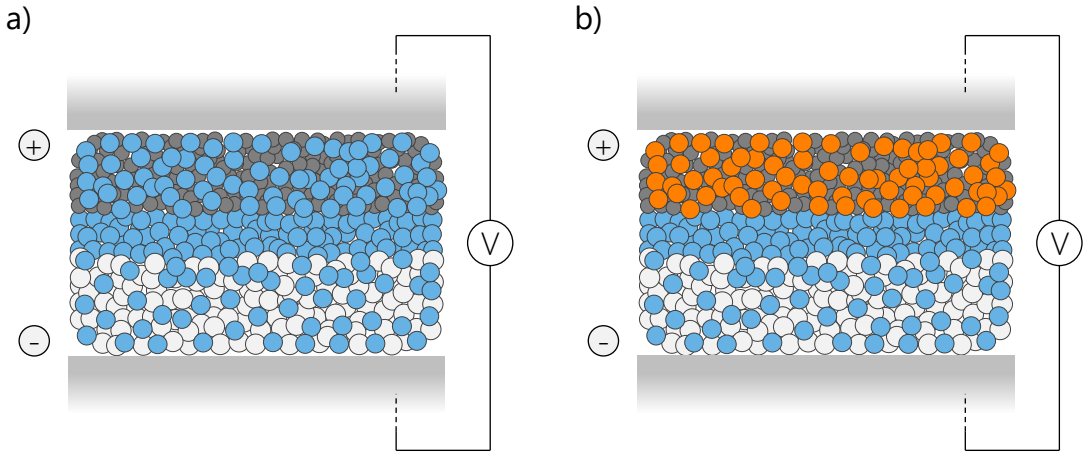

Figure 7.1. *Schematic illustration of (a) the LPS cell (LTO/LPS|LPS|NCM-811/LPS) and (b) the LATP-LPS cell (LTO/LPS|LPS|NCM-811/LATP). Grey, blue, orange, dark grey represent LTO, LPS, LATP, and NCM-811, respectively. Both cells are compressed by stainless steels and conducted the electrochemical measurements under certain pressure.*

7.2. Experimental

7.2.1. Synthesis

The solid electrolyte $Li_{1.5}Al_{0.5}Ti_{1.5}(PO_4)_3$ (LATP) was prepared by mixing lithium carbonate (Li_2CO_3, Acros Organics, 99+%), aluminum hydroxide ($Al(OH)_3$, Sigma-

Aldrich, reagent grade) and titanium dioxide (TiO_2, Sigma-Aldrich, ≥99%) in the stoichiometric ratio and thoroughly ground in an agate mortar. A 5 wt.% excess of Li_2CO_3 was added to compensate the loss of lithium at higher synthesis temperatures. The mixture was added step by step to phosphoric acid (H_3PO_4 85 wt.%, Sigma-Aldrich, 99.99%) under constant stirring. To avoid a too viscous mixture, some amount of deionized water was added. After stirring at room temperature, the mixture was heated to 200°C and kept at the target temperature for 12 h. Afterwards, the remaining solid residual was grounded and the resulting powder was then ball milled for 30 minutes at 300 rpm using a zirconium dioxide milling set (45 mL vial, one milling media with a diameter of 13 mm). The obtained powder was pelletized uniaxially at 226 MPa. Finally, the pellet was sintered in a magnesia crucible at 900°C for 24 h in air using a heating rate of 250 °C/h and sacrificial powder to prevent contact with the crucible.

The crystalline solid electrolyte of β–Li_3PS_4 (LPS), the cathode material of $LiNi_{0.8}Co_{0.1}Mn_{0.1}O_2$ (NCM-811), as well as the anode material of $Li_4Ti_5O_{12}$ (LTO) were received from BASF SE. The two electrode materials were dried in a vacuum oven at 250°C for 24 h to remove any moisture.

7.2.2. Cell assembly

The solid electrolyte LATP is used as powder rather than as sintered pellets with electrode materials to avoid any undesirable side reactions[43, 44] and to be flexible for battery assembly processes (**Figure 7.2** and **Figure 7.3**). The cathode composites consist of NCM-811 and LPS or LATP with a mass ratio of 70:30 and the anode composites of LTO and LPS with a mass ratio of 50:50, respectively (**Figure 7.1**). These composites were mixed in an agate mortar by hand for 15 min. The electrochemical cell was prepared in a previously described hot-press setup inside an argon-filled glovebox.[53] First, 100 mg of LPS were compressed between two stainless steel pistons in a ceramic cylinder at 90 MPa for 5 minutes to form a well-defined pellet of the separator. Afterwards, 20 mg of the cathode composite (2.48 mAh/cm²) and 40 mg (3.10 mAh/cm²) of the anode composite were placed and spread out on the top and the bottom of the separator, respectively. The capacity of the anode was balanced to have a surplus of capacity and not to be the limiting factor when investigating the cathode side. A pressure of 265 MPa was applied through the steel pistons and the temperature was set to 150°C. Pressure and temperature were maintained during the electrochemical measurements. Ni-rich NCM materials show decreasing thermal stability with increasing nickel content.[54-56] An electrochemically charged NCM-811 composite with an organic liquid electrolyte up to

4.3 V vs. Li/Li^+ undergoes structural changes with releasing oxygen gas at around 150°C.[55] The thermal stability depends on the surface condition[57, 58] and the preparation process.[59] In our experiment, however, all cell studies were run in an argon-filled glovebox and the solid-state battery cells provide sufficient electrochemical properties at 150°C, being comparable to the result at room temperature.[24] The reactivity of NCM materials in solid-state environment is different from that after the charge in a liquid electrolyte cell.

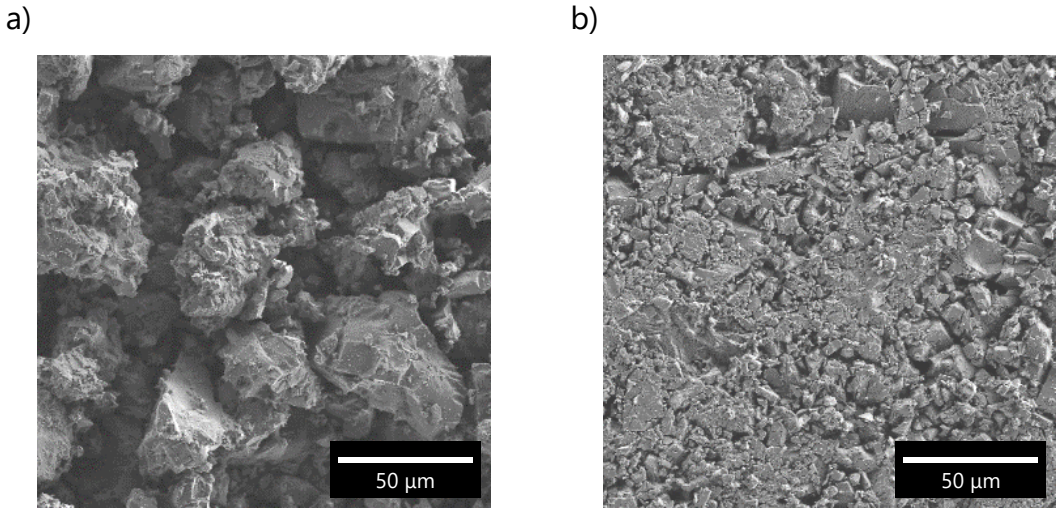

Figure 7.2. *SEM images of the LATP (a) powder and (b) its pellet by the cold press. The particle size is several µm and the density of the pellet is 2.49 g/cm³, corresponding to the ratio of 85% calculated from the theoretical value of 2.94 g/cm³. The solid electrolyte of LATP is used as powder rather than as sintered pellets with electrode materials to avoid any undesirable side reactions[43, 44] and to be flexible for battery assembly processes.*

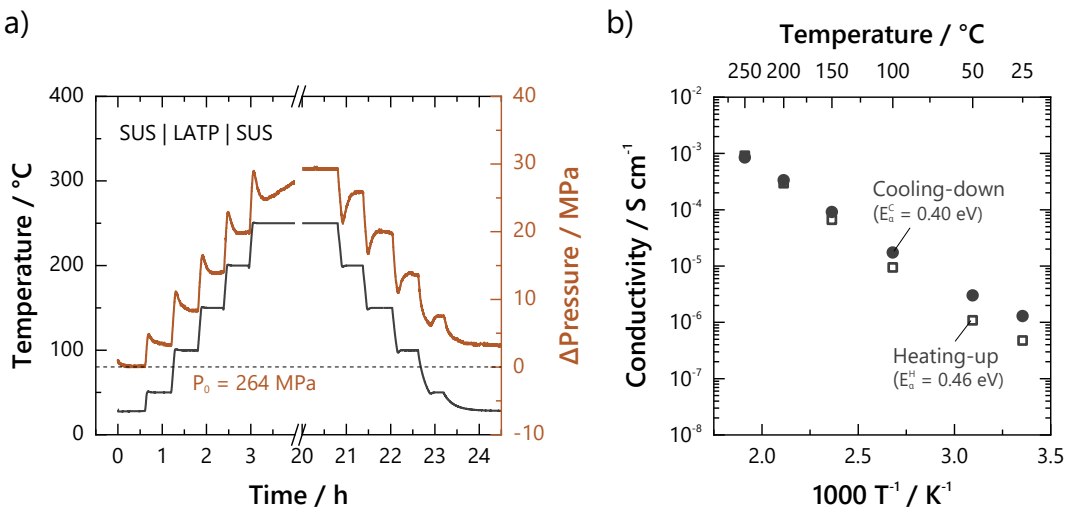

Figure 7.3. *(a) Temperature and pressure profiles upon EIS measurements. The base pressure of 264 MPa was applied. (b) Temperature dependent conductivity upon heating-up and cooling-down. From 25 to 250°C, the total conductivity increases from 5 × 10^{-7} to 9 × 10^{-4} S/cm with the pressure change due to sintering. The activation energy of ionic conductivity is 0.46 eV upon heating-up and 0.40 eV upon cooling-down. This difference comes from annealing effect that the sample was kept at 250°C overnight. The total conductivity of the LATP powder by the cold press is 5 × 10^{-7} S/cm at room temperature although the sintered pellet, which is not grounded, has a conductivity of 2 × 10^{-4} S/cm. For LATP, the total conductivity mostly depends on the grain boundary.*[39, 40] *In the grounded powder, the lack of an intimate grain contact between the SE particles hinders fast Li diffusion in the separator electrolyte. The thermal treatment, however, helps the SE to make a good contact within the grain. The battery employing LATP as the SE might work at intermediate temperature, where the total conductivity is around 10^{-4} S/cm, corresponding to the value of β-Li_3PS_4 at room temperature.*[27, 60]

7.2.3. Electrochemical Characterizations

Battery cycling and electrochemical impedance spectroscopy (EIS) were carried out using an SP-150 potentiostat/galvanostat (Bio-Logic Science Instruments). The galvanostatic charge/discharge cycling was performed at a C-rate of 0.1C (248 μA/cm²) in a voltage range of 1.1-2.8 V vs. $Li_4Ti_5O_{12}/Li_7Ti_5O_{12}$, corresponding to approximately 2.65-4.35 V vs. Li^+/Li with an assumption that the potential for lithium titanate is 1.55 V vs. Li^+/Li.[61] After each discharge step and a subsequent electrochemical relaxation of 1 hour, EIS measurements were conducted with an amplitude of 20 mV in a frequency range of 1 MHz to 0.1 Hz.

7.2.4. Scanning Electron Microscopy

Microstructural images of the cathode composites were obtained using a Merlin high-resolution scanning electron microscope (Carl Zeiss AG, Germany). The batteries were disassembled inside an argon-filled glovebox and the samples were carried to the analysis chamber using a transfer vessel (Leica EM VC500) under inert gas atmosphere. Energy-dispersive X-ray spectroscopy of the cathode composites was carried out using an XMAX EXTREME EDX detector (Oxford Instruments, UK) with an acceleration voltage of 10 kV and a probing current of 2 nA.

7.2.5. X-ray Photoelectron Spectroscopy

Measurements were carried out using a PHI5000 Versa Probe II (Physical Electronics GmbH) with an Al anode. To avoid air exposure, the samples were transferred from an argon-filled glovebox to the analysis chamber using a transfer vessel filled with argon gas. The probed surface area was 100 μm × 1400 μm (X-ray spot size) and an X-ray power of 100 W was used. The pass energy of the analyzer was set to 23.5 eV for detail spectra and to 187.9 eV for survey scans. The chamber pressure was in the range of 10^{-7} Pa during the measurements.

7.3. Results and Discussion

7.3.1. Cell characteristics

In order to investigate and compare the interfaces between LPS and LATP in contact with NCM-811 in an ASSB setup, two types of cells, cathode composites NCM-811/LPS or NCM-811/LATP and the separator LPS with anode composites LTO/LPS were assembled: LTO/LPS|LPS|NCM-811/LPS (LPS cell) as well as LTO/LPS|LPS|NCM-811/LATP (LATP-LPS cell). The schematic illustration is described in **Figure 7.1**.

The LPS cell serves as a reference cell. In case of the LATP-LPS cell, a bilayer approach was chosen and LPS was used as a separator to reduce the overall cell resistance and to avoid contact with an anode. While lithium, or a lithium-indium alloy is commonly employed in thiophosphate-based batteries as anode, here LTO is used as it is stable against the thiophosphate electrolyte[19, 62] and at elevated temperature, so that all possible changes can be attributed to the cathode interface.

The microstructures of the prepared cathode composites were investigated by the means

of scanning electron microscopy, as shown in **Figure 7.4**. To better differentiate the materials, energy dispersive X-ray (EDX) mapping was conducted simultaneously. The cathode composites consist of 70 wt.% NCM-811 and 30 wt.% SE in both cells, which results in a volumetric ratio of *V*(NCM):*V*(SE) = 48:52 in the LPS cell and 60:40 in the LATP-LPS cell. The active material is well surrounded by the SE in both cells. In contrast to the LPS cell, which shows a very dense pellet and good interfacial contact, the LATP-LPS cell necessarily has a denser packing of NCM-811 particles. The grain boundaries are still visible and the pores are also detectable in the LATP-LPS cell.

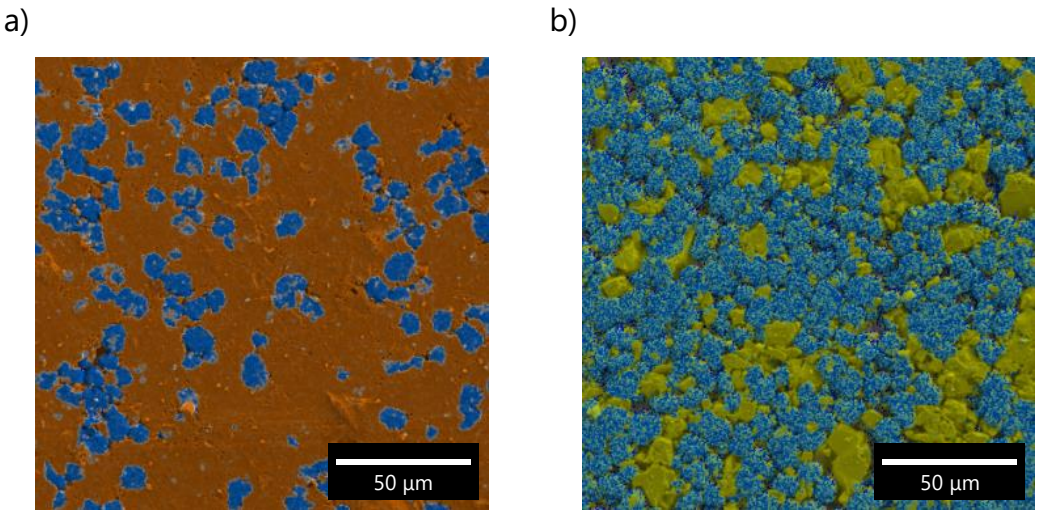

Figure 7.4. *Energy-dispersive X-ray spectroscopy mapping taken from the cathode side of (a) LTO/LPS|LPS|NCM-811/LPS cell (LPS cell) and (b) LTO/LPS|LPS|NCM811/LATP cell (LATP-LPS cell). Blue, orange, and yellow denote NCM811, LPS, and LATP particles, respectively.*

In order to remove the bulk transport barrier in the SE and compare the interfacial properites between LATP and LPS, thermal treatment helps the SE to increase the ion conductivity. Temperature dependent electrochemical impedance spectra were collected before any battery cycling to estimate the environment, which allows LATP to provide the sufficient bulk kinetics (see **Figure 7.5**). The impedance spectra **Figure 7.5a,b**) are separated into a high, a middle, and a low frequency region, where we attribute to the bulk and grain boundary responses of the separator electrolyte, and the processes at the electrode/electrolyte interface (*RQ* elements, in line with a previous report).[24] While the interface processes coming from the cathode or the anode composites cannot be deconvoluted, the stability of LTO against LPS makes the analysis simpler. The bulk

transport of the separator electrolyte can only be detected at 25°C, and afterwards the process is shifted to too high frequencies to be resolved with the employed potentiostat. Consequently, the equivalent circuit of (*RQ*)(*RQ*) is used above 25°C as shown in insets of **Figure 7.5c,d**. The bulk and grain boundary resistances of the separator electrolyte are almost the same in both cells (**Figure 7.5c,d**), as expected. The interface resistances are reduced substantially from more than 10^4 Ohm at 25°C to about 10^2 Ohm at 150°C (**Figure 7.5c,d**). On the basis of these results for the electrode impedance, both cells were investigated at a temperature of 150°C, where the interface resistance of the LATP-LPS cell is as small as that of the LPS cell. Note that the total conductivity of LATP is around 10^{-4} S/cm at 150°C (**Figure 7.3**), corresponding to the value of β–Li_3PS_4 at room temperature.[27, 60]

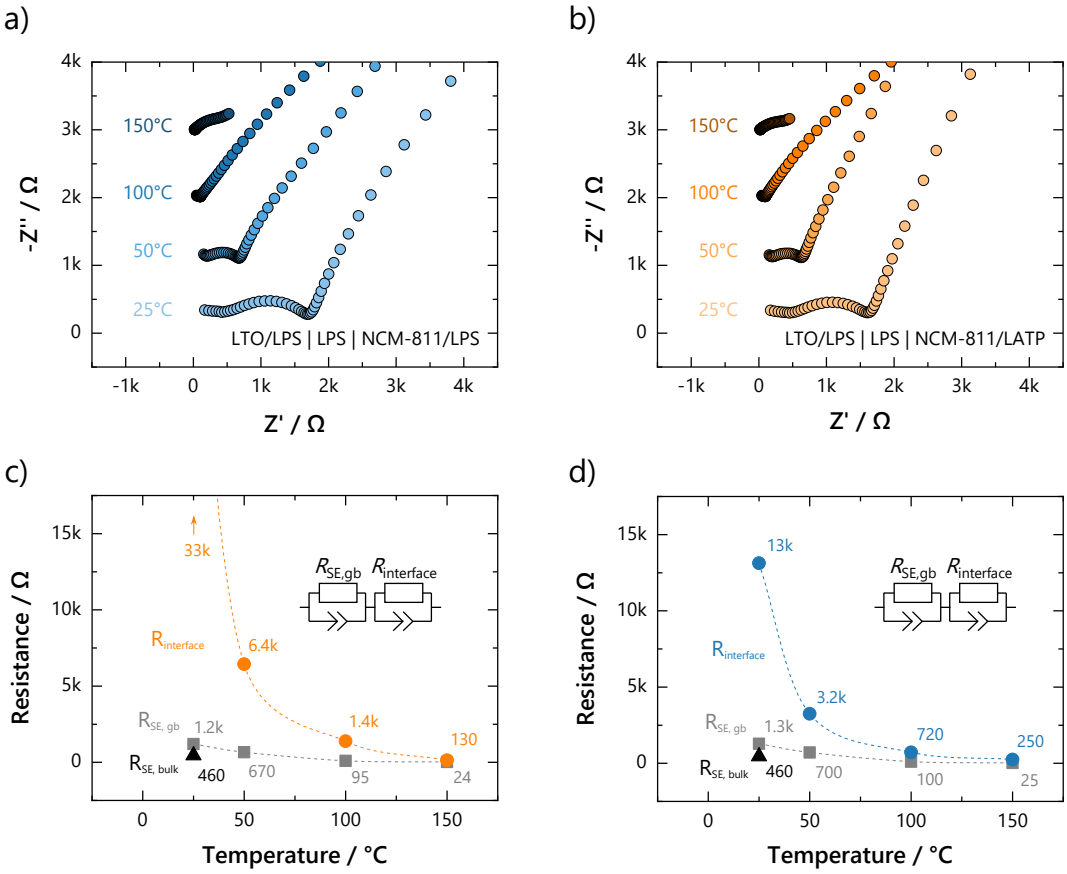

Figure 7.5. *Temperature dependent Nyquist plots of (a) the LPS cell and (b) the LATP-LPS cell at 25, 50, 100, 150°C. The spectra are stacked with an offset of 1k Ohms in the –Z'' direction. The colored circles represent the experimental data. The bulk and grain boundary resistances of the separator electrolyte as well as the interface resistances between the electrode and electrolyte in (c) the LPS cell and (d) the LATP-LPS cell. The dotted lines are guides to the eye. The equivalent circuit consists of the bulk and grain boundary responses of the separator electrolyte, and the processes at the electrode/electrolyte interface. Inset indicates the applied equivalent circuit above 25°C.*

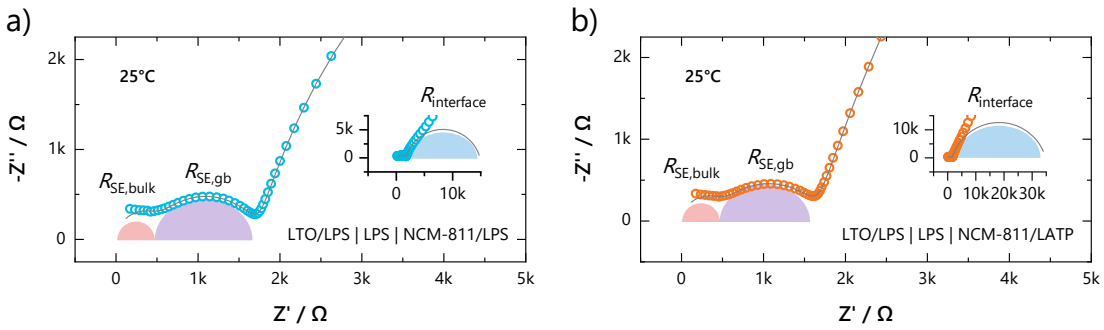

Figure 7.6. *Nyquist plots of the fitted EIS data of (a) the LPS cell and (b) LATP-LPS cell at 25°C. Colored open circles represent the experimental data and grey solid lines indicate the fited data. The employed resistances are illustrated as colored semicircles, which are a guide-to-the-eye.* $R_{SE,bulk}$ *= bulk resistance of the SE,* $R_{SE,gb}$ *= grain boundary resistance of the SE, and* $R_{interface}$ *= interface resistance between the electrode and electrolyte.*

7.3.2. Battery performance.

Figure 7.7 shows the impact of the replacement of LPS by LATP in the cathode composite upon cell cycling. The first charge and discharge capacity of both cells is around 180 and 145 mAh/g, respectively. The initial irreversible capacity and the voltage decay in the subsequent cycles can be correlated to the contact loss between the SE and the cathode particles as well as the interphase formation among them.[24] In the subsequent cycles, the LATP-LPS cell shows the higher discharge capacity and average voltage (**Figure 7.8**). The discharge capacity retention and the Coulombic efficiency of the LATP-LPS cell after 50 cycles are more than 80% and 99%, respectively, which are superior to the LPS cell.

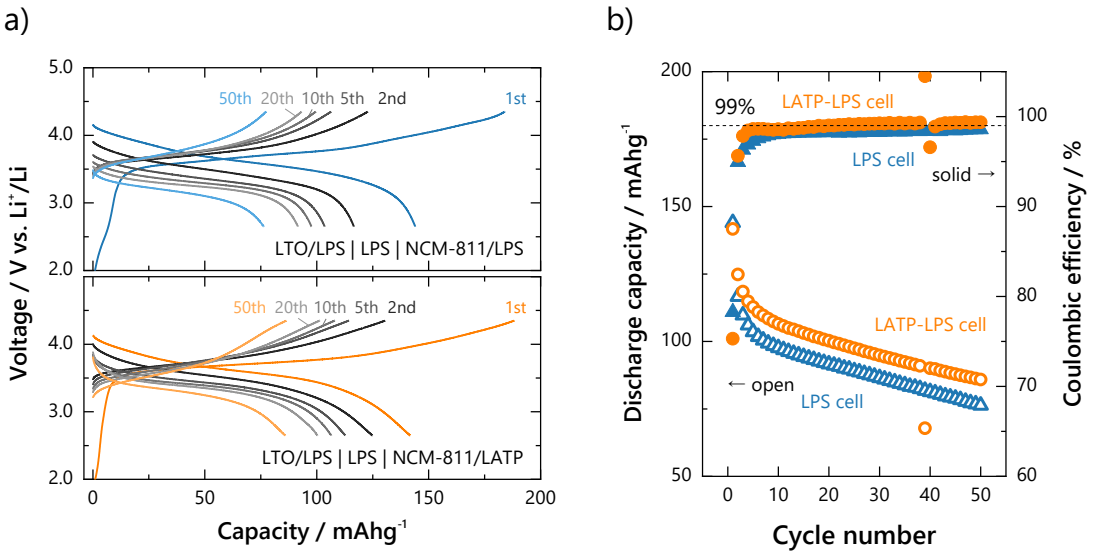

Figure 7.7. *(a) The galvanostatic charge/discharge curves of the LPS cell (top) and the LATP-LPS cell (bottom) during 50 cycles at 150°C. Blue and orange lines denote the first cycle of the LPS cell and the LATP-LPS cell, respectively. The subsequent cycles are shown as grey lines. (b) The discharge capacities and the Coulombic efficiency of the LPS cell and the LATP-LPS cell. The solid and the open blue triangle denote the discharge capacity and the Coulombic efficiency of the LPS cell. The solid and the open orange circle denote the discharge capacity and the Coulombic efficiency of the LATP-LPS cell.*

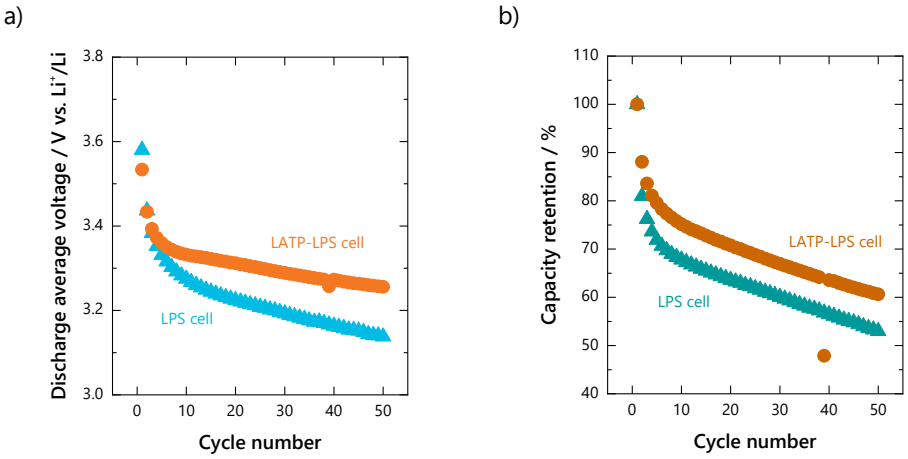

Figure 7.8. *(a) The discharge capacity retention calculated from the first cycle as 100% and (b) the discharge average voltage during the battery cycling. Blue triangle and orange circle denote the LPS cell and the LATP-LPS cell, respectively.*

Taking a closer look at the voltage profiles, the differential capacity plots are shown in **Figure 7.9**. During the first charge, several peaks can be observed at 3.60, 3.74, 4.00, and 4.19 V vs. Li/Li$^+$ in the LPS cell and 3.71, 4.00, and 4.20 V vs. Li/Li$^+$ in the LATP-LPS cell. The peak at lowest voltage in the LATP-LPS cell may represent combination of the two individual low voltage peaks in the LPS cell. The observed peaks as likely caused by the phase transitions from hexagonal to monoclinic (H1 → M), monoclinic to hexagonal (M → H2), and hexagonal to hexagonal (H2 → H3).[63-65] The voltages at the local maxima are in good agreement with previous reports.[54, 66, 67] The similarity of the differential capacity plots with those of LIBs with liquid electrolyte indicates that the total ionic conductivity within the cathode composite is comparable to the one in liquid electrolyte cells.

After the first charge, it is difficult to assign the observed curves to the three or four peaks due to an increasing peak broadening, which might arise from an inhomogeneous electrochemical reaction and could be an indicator for contact loss[68-71]. The cell potential is constituted from the combination of each individual electrode particle potential. Indeed, after the initial formation in the first charge, where contact loss and/or interface reactions may take place,[24] the inhomogeneous Li ion and electron transportation pathways and lithium concentration within the particles results in a wide potential distribution.

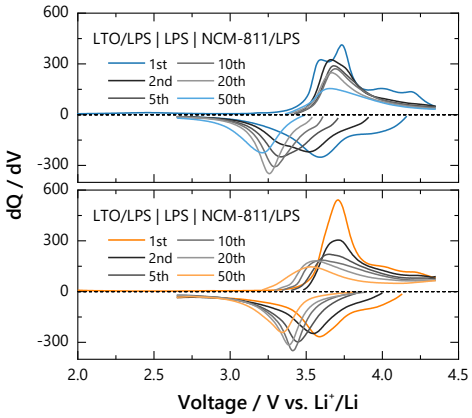

Figure 7.9. *The differential capacity plots calculated from the charge/discharge curves of the LPS cell (top) and the LATP-LPS cell (bottom) for 50 cycles at 150°C. Blue and orange lines denote the first cycle of the LPS cell and the LATP-LPS cell, respectively. The subsequent cycles are shown as grey lines.*

The frequency dependent contributions of the cathode interface to the increasing impedance are shown in **Figure 7.10** and **Table 7.1**. The EIS data were obtained after

discharge and a subsequent electrochemical relaxation for 1 h in open-circuit. Both cells show almost the same Z′ values above 10 kHz, related to the bulk and grain boundary responses of the separator SE, which is reasonable considering the cell configuration. The predominant growth of a resistive layer is seen in the low frequency region. For the LPS cell, the Z′ values increase below 10 kHz, in the frequency region which includes the cathode and anode interfacial resistances, as reported previously[23-25]. Interestingly, for the LATP-LPS cell, the Z′ values increase only below 100 Hz, which is lower by two orders of magnitude compared to the LPS cell. The Z′ values are independent of the cycle numbers down to 100 Hz, suggesting that the decomposition of the SE and/or the contact loss at the cathode interface is successfully suppressed. The long-term cycling performance can be achieved when employed LATP with NCM active materials in solid-state batteries, if the cathode interface is indeed stable.

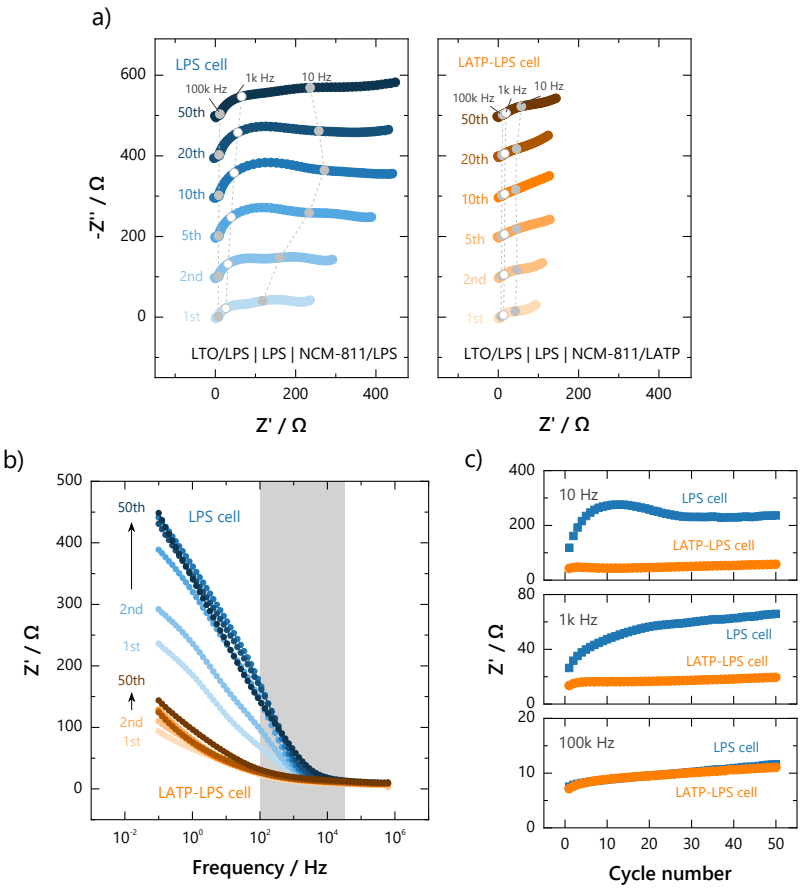

Figure 7.10. *(a) Nyquist plots of the LPS cell (top) and the LATP-LPS cell (bottom) after the 1st, 2nd, 5th, 10th, 20th, and 50th discharge. The spectra are stacked with an offset of 100 Ohms in the –Z'' direction. (b) The real part (Z') of the complex impedance (Z) of the LPS cell and the LATP-LPS cell versus frequency. The grey shadow indicates the frequency region from 10k to 100 Hz. (c) The Z' values versus cycle numbers collected at 100k (bottom), 1k (middle), and 10 (top) Hz. The blue triangles and orange circles denote the LPS cell and the LATP-LPS cell, respectively.*

Table 7.1. *The rate of increase in the Z' values depending on the frequency magnitude from 1st to 50th cycle in the LPS cell and in the LATP-LPS cell.*

Cell	$(Z'_{50th} - Z'_{1st})/Z'_{1st} \times 100$ / %				
	10 Hz	**100 Hz**	**1k Hz**	**10k Hz**	**100k Hz**
LPS	100	110	151	91.1	54.6
LATP-LPS	36.2	34.6	45.5	55.6	54.8

7.3.3. Cathode interface.

The decomposition products at the electrode/electrolyte interface play an important role for the battery performance. The chemical state of the cathode composites before and after cycling was investigated by the means of X-ray photoelectron spectroscopy (XPS) as shown in **Figure 7.11**. The measurements were conducted for the cathode composites from the collect corrector side to avoid the effect of the separator electrolyte. The analysis of electrochemically treated β–Li_3PS_4 followed by previous reports.[24, 27] For the cycled LPS cell, the SE of the cathode composite is partly oxidized as seen in the formation of additional sulfur species with higher binding energies. The deconvolution of the S 2p signals indicates the presence of S–S bonds such as found in polysulfides[72] as well as P–S bonds in the PS_4^{3-} unit and some bridging P–S–P bonds in the $P_2S_7^{4-}$ unit as seen in a pristine LPS sample. The P 2p signals show the same trend as the S 2p signals (**Figure 7.12a**). The electrochemical degradation products have a lower ionic conductivity[73] and thus hinder the lithium ion transport to and from the cathode interface. The accelerated oxidation of LPS compared to room temperature[24] occurs because the degradation reaction is thermodynamically favorable and furthermore kinetically aggressive at elevated temperatures.

In contrast, for the cycled LATP-LPS cell, the SE of the cathode composite maintains its original condition, rather than producing oxidation products, which should have resulted in a change of the XPS profile.[18, 19] The Ti 2p signals as well as the P 2p signals (see **Figure 7.12b**) are unchanged and no additional peak is found even after 50 cycles, which further corroborates the stability of LATP against NCM-811. Obviously, LATP is a promising candidate for interface modifications on the cathode side, due to its oxidation stability. Even at elevated temperature, where diffusion-driven reactions are kinetically favoured, the LATP/NCM-811 interface appears to remain intact. This is well in agreement with the impedance data that remain constant for the cathode interface in the LATP-LPS cell.

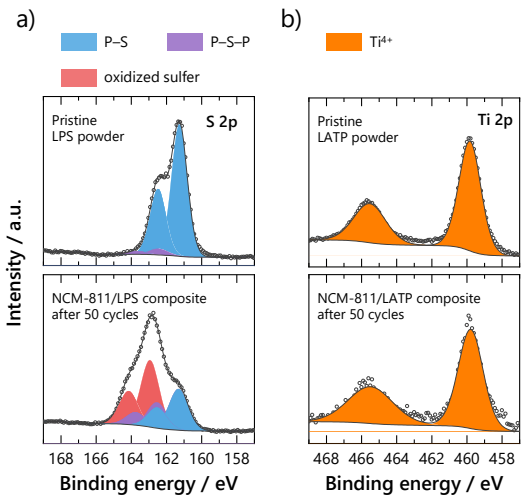

Figure 7.11. *X-ray photoemission spectra of (a) S 2p signals of the pristine LPS powder (top) and the cathode composite in the LPS cell after 50 cycles (bottom), and (b) Ti 2p signals of the pristine LATP powder (top) and the cathode composite in the LATP-LPS cell after 50 cycles (bottom). Blue and purple peaks are attributed to P–S bonds in the PS_4^{3-} unit and P–S–P bridging in the $P_2S_7^{4-}$ unit, respectively. The red peaks are assigned to more oxidized sulfur species such as polysulfides. The orange peaks represent Ti^{4+} species. The open black circles and the solid lines indicate the experimental data and the fitted ones, respectively.*

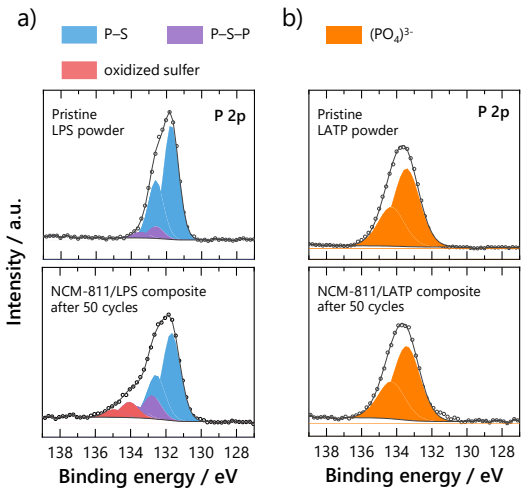

Figure 7.12. *XPS spectra of (a) P 2p signals of the pristine LPS powder (top) and the cathode composite of the LPS cell after cycling (bottom), and (b) P 2p signals of the pristine LATP powder (top) and the cathode composite of the LATP-LPS cell after 50 cycles (bottom). Blue and purple peaks are attributed to P–S bonds in the PS_4^{3-} unit and P–S–P bridging in the $P_2S_7^{4-}$ unit, respectively. The red peaks are assigned to more oxidized phosphorus species. The orange peaks represent PO_4^{3-} species. The open black circles and the solid lines indicate the experimental data and the fitted ones, respectively.*

Degradation of the electrolyte hinders unlocking the potential of electrode materials to their maximum. The onset of the potential for the rapid capacity fade of NCM materials is around 4.3 V in liquid electrolyte battery systems,[66, 74] although structurally related deterioration appears at higher potentials.[75] Replacing the electrolyte salt[76] or using electrolyte additives[77] can increase the onset and may serve for longer lifetime. The wider potential window then allows the cathodes to supply extra lithium for high capacity. This could also be used in the SSBs environment, once the SE allows high voltage operation. As thiophosphate SE are oxidized already at potentials of about 2.3 V[18, 19], LATP coatings might be a reasonable concepts for the protection of thiophosphate SE against cathode materials or the other way around. LATP could enable the use of high-voltage cathode active materials in SSBs by employing it as a composite or as a protective coating[78].

7.4. Conclusions

In this work, we have evaluated the concept of using the phosphate electrolyte

$Li_{1.5}Al_{0.5}Ti_{1.5}(PO_4)_3$ with NCM-811 cathode composite in a solid-state battery in addition to the crystalline lithium-thiophosphate β–Li_3PS_4 separator. For a fair comparison, a conventional solid-state battery system employed β–Li_3PS_4 with the cathode composite as well as the separator was constructed. In order to investigate the cahode interfaces the solid-state batteries fabricated in a hot-press setup were cycled at elevated temperatures and studied by *in-situ* electrochemical impedance spectroscopy and X-ray photoemission spectroscopy. It was found that the growth of the interface impedance is negligible and no interfacial degradation occurs when NCM-811 particles are in contact with $Li_{1.5}Al_{0.5}Ti_{1.5}(PO_4)_3$, rather than β–Li_3PS_4.

The work shows that phosphate-based electrolytes can be used in solid-state batteries, resulting in good long-term stability as no detrimental side reactions occur due to the higher oxidative stability. Indeed, while solid-state batteries are not likely run at 150°C, the stability of the phosphate electrolyte as well as the lack of an additional interface impedance during cycling suggests that $Li_{1.5}Al_{0.5}Ti_{1.5}(PO_4)_3$ may be used as a coating for cathode active materials. As $Li_{1.5}Al_{0.5}Ti_{1.5}(PO_4)_3$ has already been shown to avoid electrochemical degradation of the bulk separator for liquid electrolytes[78], this work provides a better understanding of the interfacial chemistry in solid-state battery and hopefully guides the design of long-term performance cells.

References

1. Janek, J.; Zeier, W. G., A solid future for battery development. *Nat. Energy* **2016,** *1*.

2. Culver, S. P.; Koerver, R.; Krauskopf, T.; Zeier, W. G., Designing Ionic Conductors: The Interplay between Structural Phenomena and Interfaces in Thiophosphate-Based Solid-State Batteries. *Chem. Mater.* **2018,** *30* (13), 4179-4192.

3. Goodenough, J. B.; Kim, Y., Challenges for Rechargeable Li Batteries. *Chem. Mater.* **2010,** *22* (3), 587-603.

4. Goodenough, J. B., Evolution of Strategies for Modern Rechargeable Batteries. *Acc. Chem. Res.* **2013,** *46* (5), 1053-1061.

5. Mizuno, F.; Hayashi, A.; Tadanaga, K.; Tatsumisago, M., New, highly ion-conductive crystals precipitated from Li_2S-P_2S_5 glasses. *Adv. Mater.* **2005,** *17* (7), 918-921.

6. Hayashi, A.; Minami, K.; Mizuno, F.; Tatsumisago, M., Formation of Li^+ superionic crystals from the Li_2S-P_2S_5 melt-quenched glasses. *J. Mater. Sci.* **2008,** *43* (6), 1885-1889.

7. Kamaya, N.; Homma, K.; Yamakawa, Y.; Hirayama, M.; Kanno, R.; Yonemura, M.; Kamiyama, T.; Kato, Y.; Hama, S.; Kawamoto, K.; Mitsui, A., A lithium superionic conductor. *Nat. Mater.* **2011,**

10 (9), 682-686.

8. Kato, Y.; Hori, S.; Saito, T.; Suzuki, K.; Hirayama, M.; Mitsui, A.; Yonemura, M.; Iba, H.; Kanno, R., High-power all-solid-state batteries using sulfide superionic conductors. *Nat. Energy* **2016,** *1*.

9. Dietrich, C.; Weber, D. A.; Sedlmaier, S. J.; Indris, S.; Culver, S. P.; Walter, D.; Janek, J.; Zeier, W. G., Lithium ion conductivity in Li_2S-P_2S_5 glasses - building units and local structure evolution during the crystallization of superionic conductors Li_3PS_4, $Li_7P_3S_{11}$ and $Li_4P_2S_7$. *J. Mater. Chem. A* **2017,** *5* (34), 18111-18119.

10. Bachman, J. C.; Muy, S.; Grimaud, A.; Chang, H. H.; Pour, N.; Lux, S. F.; Paschos, O.; Maglia, F.; Lupart, S.; Lamp, P.; Giordano, L.; Shao-Horn, Y., Inorganic Solid-State Electrolytes for Lithium Batteries: Mechanisms and Properties Governing Ion Conduction. *Chem. Rev.* **2016,** *116* (1), 140-162.

11. Sakuda, A.; Hayashi, A.; Tatsumisago, M., Recent progress on interface formation in all-solid-state batteries. *Curr. Opin. Electrochem.* **2017,** *6* (1), 108-114.

12. Takada, K., Progress in solid electrolytes toward realizing solid-state lithium batteries. *J. Power Sources* **2018,** *394*, 74-85.

13. Zhang, Z. Z.; Shao, Y. J.; Lotsch, B.; Hu, Y. S.; Li, H.; Janek, J.; Nazar, L. F.; Nan, C. W.; Maier, J.; Armand, M.; Chen, L. Q., New horizons for inorganic solid state ion conductors. *Energy Environ. Sci.* **2018,** *11* (8), 1945-1976.

14. Kraft, M. A.; Culver, S. P.; Calderon, M.; Bocher, F.; Krauskopf, T.; Senyshyn, A.; Dietrich, C.; Zevalkink, A.; Janek, J.; Zeier, W. G., Influence of Lattice Polarizability on the Ionic Conductivity in the Lithium Superionic Argyrodites Li_6PS_5X (X = Cl, Br, I). *J. Am. Chem. Soc.* **2017,** *139* (31), 10909-10918.

15. Krauskopf, T.; Culver, S. P.; Zeier, W. G., Bottleneck of Diffusion and Inductive Effects in $Li_{10}Ge_{1-x}Sn_xP_2S_{12}$. *Chem. Mater.* **2018,** *30* (5), 1791-1798.

16. Deng, Z.; Wang, Z. B.; Chu, I. H.; Luo, J.; Ong, S. P., Elastic Properties of Alkali Superionic Conductor Electrolytes from First Principles Calculations. *J. Electrochem. Soc.* **2016,** *163* (2), A67-A74.

17. Sakuda, A.; Hayashi, A.; Tatsumisago, M., Sulfide Solid Electrolyte with Favorable Mechanical Property for All-Solid-State Lithium Battery. *Sci. Rep.* **2013,** *3*.

18. Zhu, Y. Z.; He, X. F.; Mo, Y. F., Origin of Outstanding Stability in the Lithium Solid Electrolyte Materials: Insights from Thermodynamic Analyses Based on First-Principles Calculations. *ACS Appl. Mater. Interfaces* **2015,** *7* (42), 23685-23693.

19. Zhu, Y. Z.; He, X. F.; Mo, Y. F., First principles study on electrochemical and chemical stability of solid electrolyte-electrode interfaces in all-solid-state Li-ion batteries. *J. Mater. Chem. A* **2016,** *4* (9), 3253-3266.

20. Wenzel, S.; Randau, S.; Leichtweiss, T.; Weber, D. A.; Sann, J.; Zeier, W. G.; Janek, J., Direct Observation of the Interfacial Instability of the Fast Ionic Conductor $Li_{10}GeP_2S_{12}$ at the Lithium Metal Anode. *Chem. Mater.* **2016,** *28* (7), 2400-2407.

21. Wenzel, S.; Sedlmaier, S. J.; Dietrich, C.; Zeier, W. G.; Janek, J., Interfacial reactivity and

interphase growth of argyrodite solid electrolytes at lithium metal electrodes. *Solid State Ionics* **2018,** *318*, 102-112.

22. Ohta, N.; Takada, K.; Sakaguchi, I.; Zhang, L. Q.; Ma, R. Z.; Fukuda, K.; Osada, M.; Sasaki, T., $LiNbO_3$-coated $LiCoO_2$ as cathode material for all solid-state lithium secondary batteries. *Electrochem. Commun.* **2007,** *9* (7), 1486-1490.

23. Sakuda, A.; Hayashi, A.; Tatsumisago, M., Intefacial Observation between $LiCoO_2$ Electrode and Li_2S-P_2S_5 Solid Electrolytes of All-Solid-State Lithium Secondary Batteries Using Transmission Electron Microscopy. *Chem. Mater.* **2010,** *22* (3), 949-956.

24. Koerver, R.; Aygun, I.; Leichtweiss, T.; Dietrich, C.; Zhang, W. B.; Binder, J. O.; Hartmann, P.; Zeier, W. G.; Janek, J., Capacity Fade in Solid-State Batteries: Interphase Formation and Chemomechanical Processes in Nickel-Rich Layered Oxide Cathodes and Lithium Thiophosphate Solid Electrolytes. *Chem. Mater.* **2017,** *29* (13), 5574-5582.

25. Zhang, W. B.; Weber, D. A.; Weigand, H.; Arlt, T.; Manke, I.; Schroder, D.; Koerver, R.; Leichtweiss, T.; Hartmann, P.; Zeier, W. G.; Janek, J., Interfacial Processes and Influence of Composite Cathode Microstructure Controlling the Performance of All-Solid-State Lithium Batteries. *ACS Appl. Mater. Interfaces* **2017,** *9* (21), 17835-17845.

26. Zhang, W. B.; Leichtweiss, T.; Culver, S. P.; Koerver, R.; Das, D.; Weber, D. A.; Zeier, W. G.; Janek, J., The Detrimental Effects of Carbon Additives in $Li_{10}GeP_2S_{12}$-Based Solid-State Batteries. *ACS Appl. Mater. Interfaces* **2017,** *9* (41), 35888-35896.

27. Koerver, R.; Walther, F.; Aygun, I.; Sann, J.; Dietrich, C.; Zeier, W. G.; Janek, J., Redox-active cathode interphases in solid-state batteries. *J. Mater. Chem. A* **2017,** *5* (43), 22750-22760.

28. Zhang, W. B.; Richter, F. H.; Culver, S. P.; Leichtweiss, T.; Lozano, J. G.; Dietrich, C.; Bruce, P. G.; Zeier, W. G.; Janek, J., Degradation Mechanisms at the $Li_{10}GeP_2S_{12}$/$LiCoO_2$ Cathode Interface in an All-Solid-State Lithium-ion Battery. *ACS Appl. Mater. Interfaces* **2018,** *10* (26), 22226-22236.

29. Auvergniot, J.; Cassel, A.; Foix, D.; Viallet, V.; Seznec, V.; Dedryvere, R., Redox activity of argyrodite Li_6PS_5Cl electrolyte in all-solid-state Li-ion battery: An XPS study. *Solid State Ionics* **2017,** *300*, 78-85.

30. Auvergniot, J.; Cassel, A.; Ledeuil, J. B.; Viallet, V.; Seznec, V.; Dedryvere, R., Interface Stability of Argyrodite Li_6PS_5Cl toward $LiCoO_2$, $LiNi_{1/3}Co_{1/3}Mn_{1/3}O_2$, and $LiMn_2O_4$ in Bulk All-Solid-State Batteries. *Chem. Mater.* **2017,** *29* (9), 3883-3890.

31. Xu, X. X.; Wen, Z. Y.; Wu, X. W.; Yang, X. L.; Gu, Z. H., Lithium Ion-Conducting Glass-Ceramics of $Li_{1.5}Al_{0.5}Ge_{1.5}(PO_4)_3$-$x$$Li_2O$ (x=0.0-0.20) with Good Electrical and Electrochemical Properties. *J. Am. Ceram. Soc.* **2007,** *90* (9), 2802-2806.

32. Imanishi, N.; Hasegawa, S.; Zhang, T.; Hirano, A.; Takeda, Y.; Yamamoto, O., Lithium anode for lithium-air secondary batteries. *J. Power Sources* **2008,** *185* (2), 1392-1397.

33. Hasegawa, S.; Imanishi, N.; Zhang, T.; Xie, J.; Hirano, A.; Takeda, Y.; Yamamoto, O., Study on lithium/air secondary batteries-Stability of NASICON-type lithium ion conducting glass-ceramics with water. *J. Power Sources* **2009,** *189* (1), 371-377.

34. Muramatsu, H.; Hayashi, A.; Ohtomo, T.; Hama, S.; Tatsumisago, M., Structural change of Li_2S-P_2S_5 sulfide solid electrolytes in the atmosphere. *Solid State Ionics* **2011,** *182* (1), 116-119.

35. Aono, H.; Sugimoto, E.; Sadaoka, Y.; Imanaka, N.; Adachi, G. Y., Ionic-Conductivity of the Lithium Titanium Phosphate ($Li_{1+x}M_xTi_{2-x}(PO_4)_3$, M = Al, Sc, Y, and La) Systems. *J. Electrochem. Soc.* **1989,** *136* (2), 590-591.

36. Aono, H.; Sugimoto, E.; Sadaoka, Y.; Imanaka, N.; Adachi, G., Ionic-Conductivity of Solid Electrolytes Based on Lithium Titanium Phosphate. *J. Electrochem. Soc.* **1990,** *137* (4), 1023-1027.

37. Aono, H.; Sugimoto, E.; Sadaoka, Y.; Imanaka, N.; Adachi, G., Ionic-Conductivity and Sinterability of Lithium Titanium Phosphate System. *Solid State Ionics* **1990,** *40-1*, 38-42.

38. Weiss, M.; Weber, D. A.; Senyshyn, A.; Janek, J.; Zeier, W. G., Correlating Transport and Structural Properties in $Li_{1+x}Al_xGe_{2-x}(PO_4)_3$ (LAGP) Prepared from Aqueous Solution. *ACS Appl. Mater. Interfaces* **2018,** *10* (13), 10935-10944.

39. Arbi, K.; Mandal, S.; Rojo, J. M.; Sanz, J., Dependence of ionic conductivity on composition of fast ionic conductors $Li_{1+x}Ti_{2-x}Al_x(PO_4)_3$, $0 <= x <= 0.7$. A parallel NMR and electric impedance study. *Chem. Mater.* **2002,** *14* (3), 1091-1097.

40. Breuer, S.; Prutsch, D.; Ma, Q. L.; Epp, V.; Preishuber-Pflugl, F.; Tietz, F.; Wilkening, M., Separating bulk from grain boundary Li ion conductivity in the sol-gel prepared solid electrolyte $Li_{1.5}Al_{0.5}Ti_{1.5}(PO_4)_3$. *J. Mater. Chem. A* **2015,** *3* (42), 21343-21350.

41. Mertens, A.; Yu, S. C.; Schon, N.; Gunduz, D. C.; Tempel, H.; Schierholz, R.; Hausen, F.; Kungl, H.; Granwehr, J.; Eichel, R. A., Superionic bulk conductivity in $Li_{1.3}Al_{0.3}Ti_{1.7}(PO_4)_3$ solid electrolyte. *Solid State Ionics* **2017,** *309*, 180-186.

42. Xu, X. X.; Wen, Z. Y.; Wu, J. G.; Yang, X. L., Preparation and Electrical Properties of NASICON-type Structured $Li_{1.4}Al_{0.4}Ti_{1.6}(PO_4)_3$ Glass-ceramics by the Citric Acid-assisted Sol-gel Method. *Solid State Ionics* **2007,** *178* (1-2), 29-34.

43. Kato, T.; Yoshida, R.; Yamamoto, K.; Hirayama, T.; Motoyama, M.; West, W. C.; Iriyama, Y., Effects of sintering temperature on interfacial structure and interfacial resistance for all-solid-state rechargeable lithium batteries. *J. Power Sources* **2016,** *325*, 584-590.

44. Kim, H. S.; Oh, Y.; Kang, K. H.; Kim, J. H.; Kim, J.; Yoon, C. S., Characterization of Sputter-Deposited $LiCoO_2$ Thin Film Grown on NASICON-type Electrolyte for Application in All-Solid-State Rechargeable Lithium Battery. *ACS Appl. Mater. Interfaces* **2017,** *9* (19), 16063-16070.

45. Hoshina, K.; Yoshima, K.; Kotobuki, M.; Kanamura, K., Fabrication of $LiNi_{0.5}Mn_{1.5}O_4$ Thin Film Cathode by PVP Sol-gel Process and its Application of All-solid-state Lithium Ion Batteries Using $Li_{1+x}Al_xTi_{2-x}(PO_4)_3$ Solid Electrolyte. *Solid State Ionics* **2012,** *209*, 30-35.

46. Iwasaki, S.; Hamanaka, T.; Yamakawa, T.; West, W. C.; Yamamoto, K.; Motoyama, M.; Hirayama, T.; Iriyama, Y., Preparation of Thick-film $LiNi_{1/3}Co_{1/3}Mn_{1/3}O_2$ Electrodes by Aerosol Deposition and its Application to All-solid-state Batteries. *J. Power Sources* **2014,** *272*, 1086-1090.

47. Zhao, E. Q.; Ma, F. R.; Guo, Y. D.; Jin, Y. C., Stable LATP/LAGP double-layer solid electrolyte prepared via a simple dry-pressing method for solid state lithium ion batteries. *RSC Adv.* **2016,** *6* (95), 92579-92585.

48. Lee, S. S.; Lim, Y. J.; Kim, H. W.; Kim, J. K.; Jung, Y. G.; Kim, Y., Electrochemical properties of a ceramic-polymer-composite-solid electrolyte for Li-ion batteries. *Solid State Ionics* **2016,** *284*, 20-24.

49. Xu, H. H.; Wang, S. F.; Wilson, H.; Zhao, F.; Manthiram, A., Y-Doped NASICON-type $LiZr_2(PO_4)_3$ Solid Electrolytes for Lithium Metal Batteries. *Chem. Mater.* **2017,** *29* (17), 7206-7212.

50. Lee, S. D.; Jung, K. N.; Kim, H.; Shin, H. S.; Song, S. W.; Park, M. S.; Lee, J. W., Composite Electrolyte for All-Solid-State Lithium Batteries: Low-Temperature Fabrication and Conductivity Enhancement. *ChemSusChem* **2017,** *10* (10), 2175-2181.

51. Liang, Y. Z.; Lin, Z.; Qiu, Y. P.; Zhang, X. W., Fabrication and characterization of LATP/PAN composite fiber-based lithium-ion battery separators. *Electrochim. Acta* **2011,** *56* (18), 6474-6480.

52. Busche, M. R.; Drossel, T.; Leichtweiss, T.; Weber, D. A.; Falk, M.; Schneider, M.; Reich, M. L.; Sommer, H.; Adelhelm, P.; Janek, J., Dynamic formation of a solid-liquid electrolyte interphase and its consequences for hybrid-battery concepts. *Nat. Chem.* **2016,** *8* (5), 426-434.

53. Busche, M. R.; Weber, D. A.; Schneider, Y.; Dietrich, C.; Wenzel, S.; Leichtweiss, T.; Schroder, D.; Zhang, W. B.; Weigand, H.; Walter, D.; Sedlmaier, S. J.; Houtarde, D.; Nazar, L. F.; Janek, J., In Situ Monitoring of Fast Li-Ion Conductor $Li_7P_3S_{11}$ Crystallization Inside a Hot-Press Setup. *Chem. Mater.* **2016,** *28* (17), 6152-6165.

54. Noh, H. J.; Youn, S.; Yoon, C. S.; Sun, Y. K., Comparison of the structural and electrochemical properties of layered $Li[Ni_xCo_yMn_z]O_2$ (x=1/3, 0.5, 0.6, 0.7, 0.8 and 0.85) cathode material for lithium-ion batteries. *J. Power Sources* **2013,** *233*, 121-130.

55. Bak, S. M.; Hu, E. Y.; Zhou, Y. N.; Yu, X. Q.; Senanayake, S. D.; Cho, S. J.; Kim, K. B.; Chung, K. Y.; Yang, X. Q.; Nam, K. W., Structural Changes and Thermal Stability of Charged $LiNi_xMn_yCo_zO_2$ Cathode Materials Studied by Combined In Situ Time-Resolved XRD and Mass Spectroscopy. *ACS Appl. Mater. Interfaces* **2014,** *6* (24), 22594-22601.

56. Hwang, S.; Kim, S. M.; Bak, S. M.; Kim, S. Y.; Cho, B. W.; Chung, K. Y.; Lee, J. Y.; Stach, E. A.; Chang, W., Using Real-Time Electron Microscopy To Explore the Effects of Transition-Metal Composition on the Local Thermal Stability in Charged $Li_xNi_yMn_zCo_{1-y-z}O_2$ Cathode Materials. *Chem. Mater.* **2015,** *27* (11), 3927-3935.

57. Myung, S. T.; Lee, K. S.; Yoon, C. S.; Sun, Y. K.; Amine, K.; Yashiro, H., Effect of AlF_3 Coating on Thermal Behavior of Chemically Delithiated $Li_{0.35}[Ni_{1/3}Co_{1/3}Mn_{1/3}]O_2$. *J. Phys. Chem. C* **2010,** *114* (10), 4710-4718.

58. Cho, W.; Kim, S. M.; Song, J. H.; Yim, T.; Woo, S. G.; Lee, K. W.; Kim, J. S.; Kim, Y. J., Improved electrochemical and thermal properties of nickel rich $LiNi_{0.6}Co_{0.2}Mn_{0.2}O_2$ cathode materials by SiO_2 coating. *J. Power Sources* **2015,** *282*, 45-50.

59. Cho, D. H.; Jo, C. H.; Cho, W.; Kim, Y. J.; Yashiro, H.; Sun, Y. K.; Myung, S. T., Effect of Residual Lithium Compounds on Layer Ni-Rich $Li[Ni_{0.7}Mn_{0.3}]O_2$. *J. Electrochem. Soc.* **2014,** *161* (6), A920-A926.

60. Liu, Z. C.; Fu, W. J.; Payzant, E. A.; Yu, X.; Wu, Z. L.; Dudney, N. J.; Kiggans, J.; Hong, K. L.; Rondinone, A. J.; Liang, C. D., Anomalous High Ionic Conductivity of Nanoporous β-Li_3PS_4. *J. Am. Chem. Soc.* **2013,** *135* (3), 975-978.

61. Ohzuku, T.; Ueda, A.; Yamamoto, N., Zero-Strain Insertion Material of $Li[Li_{1/3}Ti_{5/3}]O_4$ for Rechargeable Lithium Cells. *J. Electrochem. Soc.* **1995,** *142* (5), 1431-1435.

62. Wu, X. H.; El Kazzi, M.; Villevieille, C., Surface and morphological investigation of the

electrode/electrolyte properties in an all-solid-state battery using a Li_2S-P_2S_5 solid electrolyte. *J. Electroceram.* **2017,** *38* (2-4), 207-214.

63. Li, W.; Reimers, J. N.; Dahn, J. R., In-Situ X-Ray-Diffraction and Electrochemical Studies of $Li_{1-x}NiO_2$. *Solid State Ionics* **1993,** *67* (1-2), 123-130.

64. Ohzuku, T.; Ueda, A.; Nagayama, M., Electrochemistry and Structural Chemistry of $LiNiO_2$ R-3m for 4 Volt Secondary Lithium Cells. *J. Electrochem. Soc.* **1993,** *140* (7), 1862-1870.

65. Arai, H.; Okada, S.; Ohtsuka, H.; Ichimura, M.; Yamaki, J., Characterization and Cathode Performance of $Li_{1-x}Ni_{1+x}O_2$ Prepared with the Excess Lithium Method. *Solid State Ionics* **1995,** *80* (3-4), 261-269.

66. Li, J.; Downie, L. E.; Ma, L.; Qiu, W. D.; Dahn, J. R., Study of the Failure Mechanisms of $LiNi_{0.8}Mn_{0.1}Co_{0.1}O_2$ Cathode Material for Lithium Ion Batteries. *J. Electrochem. Soc.* **2015,** *162* (7), A1401-A1408.

67. Sakuda, A.; Takeuchi, T.; Kobayashi, H., Electrode morphology in all-solid-state lithium secondary batteries consisting of $LiNi_{1/3}Co_{1/3}Mn_{1/3}O_2$ and Li_2S-P_2S_5 solid electrolytes. *Solid State Ionics* **2016,** *285*, 112-117.

68. Otoyama, M.; Ito, Y.; Hayashi, A.; Tatsumisago, M., Raman imaging for $LiCoO_2$ composite positive electrodes in all-solid-state lithium batteries using Li_2S-P_2S_5 solid electrolytes. *J. Power Sources* **2016,** *302*, 419-425.

69. Otoyama, M.; Ito, Y.; Hayashi, A.; Tatsumisago, M., Raman Spectroscopy for $LiNi_{1/3}Mn_{1/3}Co_{1/3}O_2$ Composite Positive Electrodes in All-Solid-State Lithium Batteries. *Electrochemistry* **2016,** *84* (10), 812-814.

70. Strobridge, F. C.; Orvananos, B.; Croft, M.; Yu, H. C.; Robert, R.; Liu, H.; Zhong, Z.; Connolley, T.; Drakopoulos, M.; Thornton, K.; Grey, C. P., Mapping the Inhomogeneous Electrochemical Reaction Through Porous $LiFePO_4$-Electrodes in a Standard Coin Cell Battery. *Chem. Mater.* **2015,** *27* (7), 2374-2386.

71. Orvananos, B.; Ferguson, T. R.; Yu, H. C.; Bazant, M. Z.; Thornton, K., Particle-Level Modeling of the Charge-Discharge Behavior of Nanoparticulate Phase-Separating Li-Ion Battery Electrodes. *J. Electrochem. Soc.* **2014,** *161* (4), A535-A546.

72. Dietrich, C.; Koerver, R.; Gaultois, M. W.; Kieslich, G.; Cibin, G.; Janek, J.; Zeier, W. G., Spectroscopic characterization of lithium thiophosphates by XPS and XAS – a model to help monitor interfacial reactions in all-solid-state batteries. *Phys. Chem. Chem. Phys.* **2018,** *20* (30), 20088-20095.

73. Richards, W. D.; Miara, L. J.; Wang, Y.; Kim, J. C.; Ceder, G., Interface Stability in Solid-State Batteries. *Chem. Mater.* **2016,** *28* (1), 266-273.

74. Jung, R.; Metzger, M.; Maglia, F.; Stinner, C.; Gasteiger, H. A., Oxygen Release and Its Effect on the Cycling Stability of $LiNi_xMn_yCo_zO_2$ (NMC) Cathode Materials for Li-Ion Batteries. *J. Electrochem. Soc.* **2017,** *164* (7), A1361-A1377.

75. Chen, Z. H.; Dahn, J. R., Methods to obtain excellent capacity retention in $LiCoO_2$ cycled to 4.5 V. *Electrochim. Acta* **2004,** *49* (7), 1079-1090.

76. Gallus, D. R.; Schmitz, R.; Wagner, R.; Hoffmann, B.; Nowak, S.; Cekic-Laskovic, I.; Schmitz, R. W.; Winter, M., The influence of different conducting salts on the metal dissolution and capacity fading of NCM cathode material. *Electrochim. Acta* **2014,** *134*, 393-398.

77. Li, J.; Liu, H. S.; Xia, J.; Cameron, A. R.; Nie, M. Y.; Botton, G. A.; Dahn, J. R., The Impact of Electrolyte Additives and Upper Cut-off Voltage on the Formation of a Rocksalt Surface Layer in $LiNi_{0.8}Mn_{0.1}Co_{0.1}O_2$ Electrodes. *J. Electrochem. Soc.* **2017,** *164* (4), A655-A665.

78. Liang, J. Y.; Zeng, X. X.; Zhang, X. D.; Wang, P. F.; Ma, J. Y.; Yin, Y. X.; Wu, X. W.; Guo, Y. G.; Wan, L. J., Mitigating Interfacial Potential Drop of Cathode-Solid Electrolyte via Ionic Conductor Layer To Enhance Interface Dynamics for Solid Batteries. *J. Am. Chem. Soc.* **2018,** *140* (22), 6767-6770.

Chapter 8.
General conclusions

In Chapter 1, the overview of fundamental principles for batteries and thermodynamics of two-phase materials were described.

In Chapter 2, $Li(Fe_{0.95}Zr_{0.05})(P_{0.9}Si_{0.1})O_4$, which is the material with reduced lattice mismatch based on the mother structure of $LiFePO_4$, demonstrates the high rate performance in addition to the long cycle life. The participation of the metastable intermediate phase is responsible for the intercalation reaction under the extremely high current rate in a wide Li compositional range. Suppression of the lattice volume change could open bypath for the fast phase transition kinetics.

In Chapter 3, the intermediate phase, which has been observed at ambient temperature as the metastable phase, was thermodynamically stabilized at elevated temperature and investigated the role in the phase transition. The discrepancy between the nucleation point and the maximum composition of the phase produces the unexpected results that the sequential phase transition via the intermediate solid solution phase proceeds on the charge, but the three phases coexist in a whole reaction on the discharge. The formation of the intermediate solid solution phase is important as its further stabilization leads to an extension of a single phase reaction, realizing high-rate electrode materials.

In Chapter 4, the intermediate phase of $Li(Fe_{0.95}Zr_{0.05})(P_{0.9}Si_{0.1})O_4$ was further investigated as a thermodynamically stable phase at elevated temperature. The stability of the intermediate phase provides the new approach for material exploration.

In Chapter 5, the surface modification of $LiFePO_4$ by nitrogen was investigated in the model thin-film electrode. The electronic and local structure changes accelerate lithium ions transportation at the interface between surface-nitrided LiFePO4 and electrolyte, improving the rate performance.

In Chapter 6, the thin-film Cu cathode was fabricated as a model metal electrode in fluoride-ion battery system. With an assumption of 3 V battery configuration with an appropriate anode, the energy density would achieve 2,000 Wh/kg. The electrochemical reaction of Cu/CuF_2 proceeds with separation into two phases, Cu and CuF_2. Metal alloys offer the tremendous possibility to design materials to be reduced the lattice strain at phase boundary. Cu_3Au alloy provides the high rate performance as well as the long cycle life compared to Cu metal. The findings have implication for battery design and utilization, which could be realized by such as materials informatics.

In Chapter 7, the concept of using the phosphate electrolyte $Li_{1.5}Al_{0.5}Ti_{1.5}(PO_4)_3$ within $LiNi_{0.8}Co_{0.1}Mn_{0.1}O_2$ cathode composite was evaluated. The stability of the phosphate electrolyte as well as the lack of an additional interface impedance during cycling suggests the usage as a coating for cathode active materials.

In Chapter 8, the results of the thesis were summarized.

Acknowledgement

I would like to express my gratitude to all those who helped me during the writing of this thesis.

My deepest gratitude goes first and foremost to Professor Yoshiharu Uchimoto, for his constant encouragement and guidance. He has walked me through all the stages of the writing of this thesis. Without his consistent and illuminating instruction, this thesis could not have reached its present form.

I am also greatly indebted to all the members of Prof. Uchimoto's laboratory, who have instructed and helped me a lot in the past six years.

Special thanks are expressed to Dr. Yuki Orikasa and Dr. Kentaro Yamamoto for their advices on the whole study.

Last, my thanks would go to my beloved family for their loving considerations and great confidence in me all through these years.

Kyoto, JAPAN
February, 2019
Takahiro Yoshinari

List of publications

Chapter 2

Takahiro Yoshinari, Kentaro Yamamoto, Motoaki Nishijima, Katsutoshi Fukuda, Akihide Kuwabara, Isao Tanaka, Kazuhiko Maeda, Hiroshi Kageyama, Yuki Orikasa, Yoshiharu Uchimoto

"High rate performance of dual-substituted $LiFePO_4$ based on controlling metastable intermediate phase"

ACS Appl. Energy Mater. **2018,** *1* (12), 6736-6740.

Chapter 3

Takahiro Yoshinari, Takuya Mori, Kazufumi Otani, Toshiyuki Munesada, Kentaro Yamamoto, Katsutoshi Fukuda, Yukinori Koyama, Rika Hagiwara, Yuki Orikasa, Yoshiharu Uchimoto

"Current-induced hysteretic phase transition behavior via intermediate solid solution phase in $LiFePO_4$"

Journal of Materials Chemistry A, submitted

Chapter 4

Takahiro Yoshinari, Kentaro Yamamoto, Motoaki Nishijima, Naoya Hamaguchi, Katsutoshi Fukuda, Kazuhiko Maeda, Hiroshi Kageyama, Yuki Orikasa, Yoshiharu Uchimoto

"Stabilization of Intermediate Phase in $LiFePO_4$ for High-power Li-ion batteries"

Solid State Ionics, submitted

Chapter 5

Kentaro Yamamoto, Takahiro Yoshinari, Akihide Kuwabara, Eri Kato, Yuki Orikasa, Koji Nakanishi, Tomoki Uchiyama, Kazuhiko Maeda, Hiroshi Kageyama, Toshiaki Ohta, Yoshiharu Uchimoto

"Fast lithium ion intercalation/deintercalation at the interface between surface-nitrided $LiFePO_4$ electrode and electrolyte"

Journal of Physical Chemistry C, submitted

Chapter 6

Takahiro Yoshinari, Yuya Kitaguchi, Aika Ochi, Kentaro Yamamoto, Tomoki Uchiyama, Yuki Orikasa, Koji Amezawa, Yoshiharu Uchimoto

"Design Principle for Metal/Metal Fluoride-ion Electrode Materials for High-energy Density Storages**"**

Nature energy, submitted

Chapter 7

Takahiro Yoshinari, Raimund Koerver, Patrick Hofmann, Yoshiharu Uchimoto, Wolfgang G. Zeier, Jürgen Janek

"Interfacial stability of phosphate-NASICON solid electrolytes in Ni-rich NCM cathode-based solid-state batteries"

Chemistry of Materials, submitted